Structural and functional characterisation of conventional kinesin and mitotic kinesin Eg5 — a validated target for cancer chemotherapy

Hung Yi Kristal Kaan (B.Sc)

Submitted to the University of Glasgow
in fulfilment of the requirements for the Degree of
Doctor of Philosophy

Beatson Institute for Cancer Research
Garscube Estate
Switchback Road
Glasgow G61 1BD, U.K.

September 2011

Abstract

Kinesins are molecular motors that use energy from ATP hydrolysis to transport cargoes along microtubule tracks. There are at least 14 families of kinesins with different structural organisations but all kinesins have a motor domain that is the catalytic core for ATP hydrolysis and the binding site for microtubules. Most kinesins have a stalk domain, which facilitates oligomerisation, and a tail domain that is implicated in cargo binding and regulation. Depending on their structural organisation, each kinesin is suited for different functions. Some are involved in transporting vesicles and organelles in cells, while others are essential for axonal transport in neurons. Still others are involved in intraflagellar transport in cilia. Lastly, a group of kinesins participate in different steps of mitosis.

One such kinesin is the human mitotic kinesin Eg5. It is a homotetrameric kinesin that is made up of a dimer of anti-parallel dimers. By cross-linking anti-parallel microtubules and moving towards their plus ends, Eg5 slides them apart and establishes the bipolar spindle. When Eg5 is inhibited by antibodies or siRNA, cells arrest in mitosis with non-separated centrosomes and monoastral spindles. Prolonged mitotic arrest eventually leads to apoptotic cell death. For that reason, Eg5 is a potential target for drug development in cancer chemotherapy with seven inhibitors in Phase I and II clinical trials. The first inhibitor of Eg5 was discovered in a phenotype-based screen and is called monastrol. Since then, several classes of inhibitors, such as ispinesib (a clinical trial candidate) and S-trityl-L-cysteine (STLC), have been discovered.

To develop more potent inhibitors, we employed a structure-based drug design approach. By determining crystal structures of the Eg5 motor domain in complex with various inhibitors, we can understand the interactions between the inhibitor and Eg5; thus, analysis of the structure-activity relationship (SAR) can help us to improve their potency. Consequently, these inhibitors could complement or act as alternatives to taxanes and vinca alkaloids, which are successful cancer chemotherapeutics currently used in the clinic, but have the tendency to cause neurotoxicities and develop resistance in patients.

Here, I report the crystal structures of Eg5 in complex with three monastrol analogues, STLC, and four STLC analogues separately. Based on the crystal structures with monastrol analogues, I identified the preferential binding mode of each inhibitor and the main reasons for increased potency: namely the better fit of the ligand and the addition of two fluorine atoms. Next, the crystal structure of Eg5-STLC indicates that the three phenyl rings in STLC are buried in a mainly hydrophobic region, while the cysteine moiety of STLC is solvent-exposed. In addition, structures of Eg5 in complex with STLC analogues, which have *meta*- or *para*-substituents on one or more of the phenyl rings, reveal the positions of the substituents and provide valuable information for the SAR study. In short, these structures reveal important interactions in the inhibitor-binding pocket that will aid development of more potent inhibitors.

To understand the molecular mechanism of inhibition, I examined the structure of the Eg5-STLC complex, which revealed an unprecedented intermediate state, whereby local changes at the inhibitor-binding pocket have not propagated to structural changes at the switch II cluster and neck linker. This provides structural evidence for the sequence of drug-induced conformational changes. In addition, I performed isothermal titration calorimetry to determine the thermodynamic parameters of the interaction between Eg5 and its inhibitors. The structural information and the thermodynamic parameters obtained help us to gain a better understanding of the molecular mechanism of inhibition by an Eg5 inhibitor.

While there is a large amount of information about the motor domain of Eg5, less is known about the stalk domain, which facilitates oligomerisation. A prediction program showed that the first ~100 residues of the stalk domain have a high probability of forming a coiled-coil structure, while the middle ~150 residues have a low probability. Using analytical ultracentrifugation, I showed that the Eg5 $stalk_{364-520}$ domain exists predominantly as a dimer with a sedimentation coefficient of 1.76 S. The purported coiled-coil quaternary structure is backed-up by circular dichroism data, which showed that Eg5 $stalk_{364-520}$ domain contains about 52 % helical content. Finally, the low resolution solution structure of Eg5 $stalk_{364-520}$ domain was determined by small angle X-ray scattering, which revealed an elongated structure that is ~165 Å in length.

Together, these data give us a glimpse into the structural characteristics of the Eg5 stalk$_{364\text{-}520}$ domain.

Besides gaining a better understanding of Eg5, I decided to investigate the molecular mechanism of autoinhibition in conventional kinesin (later known as kinesin-1). As the founding member of kinesins, it was first discovered to be involved in axonal transport. When not transporting cargo, kinesin-1 is autoinhibited to prevent squandering of ATP. Although it is widely accepted that the tail binds to the motor domain to keep it in a folded autoinhibited state, the molecular mechanism remains unclear and several mechanisms have been proposed. Here, I report the crystal structures of the *Drosophila melanogaster* kinesin-1 motor domain dimer and the dimer-tail complex. The dimer, which exhibits ~180° rotational symmetry between the monomers, provides valuable structural information for modeling the motility of kinesins on microtubules.

By comparing the free dimer with the dimer-tail complex, we observe that the motor domains have considerable freedom of movement in the absence of tail binding. However, in the dimer-tail complex, a 'double lockdown' at both the neck coil and the tail interface freezes out major movements. This could prevent conformational changes, such as neck linker undocking. Data from our collaborator (David Hackney) showed that a covalent cross-link, which mimics double lockdown of the dimer, prevents ADP release. Together, we propose a 'double lockdown' mechanism, in which cross-linking at both the coiled-coil and tail interface prevents the movement of the motor domains that is needed to undock the neck linker and release ADP. In short, the structures shed light on the autoinhibition mechanism, reveal important residues at the dimer-tail interface, invalidate other proposed mechanisms, and open up the possibility that other kinesins may be regulated by the same mechanism.

Table of Contents

List of Figures

List of Tables

List of Accompanying Material

Preface

Dedicated to my maternal Aunt, Tan Bee Lay (1952 – 2006)
and paternal Uncle, Kaan Quan Hon (1955 – 2011),
who had fought bravely against cancers for several years
and had inspired me to search for cures against cancers.

Acknowledgements

First and foremost, I would like to thank God, for by His grace, I was able to achieve the results presented in this thesis.

I would like to express my gratitude to my supervisor, Prof. Frank Kozielski, for his support and guidance throughout my entire research project. I am also grateful to my advisor, Prof. Mike Olson, and post-graduate convenor, Prof. Nicol Keith, for their wise counsel. I would also like to thank the members of the R9 group (present: James Good, Marta Klejnot, Oliver Rath, Alexander Schüttelkopf, Sandeep Talapatra, Venkat Ulaganathan and Fang Wang; past: Chris Gray and Katarzyna Tkocz) for their invaluable help and friendship.

I am also indebted to my undergraduate honours project supervisor, Prof. Holger Sondermann (Cornell University), who taught me various techniques and sparked my interest in X-ray crystallography. Special mention also go out to our collaborators Prof. David Hackney (Carnegie Mellon University), Prof. C. Oliver Kappe (University of Graz), Prof. Johanna Weiss (University of Heidelberg), Prof. Benoit Joseph (University Claude Bernard Lyon), Dr. Olwyn Byron and Dr. Sharon Kelly (both from University of Glasgow) for their input towards my project.

The completion of my research project would not have been possible without the love and support of my family and friends, both in Singapore and Glasgow. I would also like to express my appreciation to my husband for his continual encouragement that has allowed me to persevere in my studies.

The Beatson Proteomics Facility, Molecular Technology Services and Central Services at the Beatson Institute have been tremendously helpful in providing the relevant services. I would also like to acknowledgement the European Synchrotron Radiation Facility (ESRF), Diamond Light Source (DLS) and Swiss Light Source (SLS) for providing us with beamtime and assistance.

Last but not least, I am grateful to the Agency for Science, Technology and Research (A*STAR), Singapore for funding my studies and to Cancer Research UK (CRUK) for funding our research.

Author's Declaration

I declare that I am the sole author of this thesis and the work presented here is entirely my own, except where acknowledged to others. This thesis does not include work that has been submitted for consideration for another degree in this or any other university.

Definitions / Abbreviations

Å	Ångström
A_{600}	Absorbance at 600 nm
ABS	Auxiliary binding site
ADME	Absorption, distribution, metabolism and excretion
ADP	Adenosine diphosphate
AMPPNP	Adenylyl-imidodiphosphate
APP	Amyloid precursor protein
ATP	Adenosine triphosphate
AUC	Analytical ultracentrifugation
CD	Circular dichroism
Cdk1	Cyclin dependent kinase 1
cDNA	Complementary deoxyribonucleic acid
CENP-E	Centromere-associated protein E
CLM	Cys-lite mutant
cm	Centimetre
cryo-EM	Cryo-electron microscopy
Da	Dalton
ΔH	Enthalpy change
ΔS	Entropy change
DESY	Deutsches Elektronen-Synchrotron
DHPM	Dihydropyrimidine
D_{max}	Maximum dimension
DMSO	Dimethyl sulfoxide
DTT	Dithiothreitol
E1	Enantiomer 1
E2	Enantiomer 2
EC_{50}	Half maximal effective concentration
EDTA	Ethylenediaminetetraacetic acid
EGTA	Ethylene glycol tetraacetic acid
EMBL	European Molecular Biology Laboratory
ESRF	European Synchrotron Radiation Facility
HEPES	4-(2-hydroxyethyl)-1-piperazineethanesulfonic acid
hr	Hour

I(0)	Extrapolated intensity at zero scattering angle
IC_{50}	Half maximal inhibitory concentration
IPTG	Isopropyl ß-D-thiogalactopyranoside
ITC	Isothermal titration calorimetry
K_2HPO_4	Dipotassium phosphate
K_a	Association constant
kcal/mol	Kilocalorie per mole
KCl	Potassium chloride
K_d	Dissociation constant
kDa	Kilodalton
KHC	Kinesin heavy chain
K_i^{app}	Apparent inhibitor constant
KLC	Kinesin light chain
l	Litre
M	Molar
mant-ADP	2'-/3'-O-(N'-Methylanthraniloyl)adenosine-5'-O-diphosphate
MCAK	Mitotic centromere-associated kinesin
MDR	Multidrug resistance
MES	2-(N-morpholino)ethanesulfonic acid
mg	Milligram
Mg^{2+}ADP	Magnesium-adenosine diphosphate complex
MgATP	Magnesium-adenosine triphosphate complex
$MgCl_2$	Magnesium chloride
mins	Minutes
ml	Millilitre
mm	Millimetre
mM	Millimolar
mRNP	Messenger ribonucleoprotein
MTs	Microtubules
$M_{w,app}$	Apparent weight average molecular weight
N	Stoichiometry
NaCl	Sodium chloride
Ncd	Non-claret disjunctional
NEB	New England Biolabs
NiNTA	Ni(2+)-nitrilotriacetic acid

nm	Nanometre
nM	Nanomolar
nt	Not tested
p(r)	Pair-distance distribution function
PCR	Polymerase chain reaction
PEG	Polyethylene glycol
Pgp	P-glycoprotein
PIPES	Piperazine-N,N′-bis(2-ethanesulfonic acid)
PMSF	Phenylmethanesulfonylfluoride
pN	Piconewton
r.m.s.d.	Root-mean-square deviation
rac	Racemic
R_g	Radius of gyration
rpm	Rounds per minute
rtp	Room temperature and pressure
S	Svedberg
$s^\circ_{20,w}$	True sedimentation coefficient at 20°C and in water, at zero concentration
$s_{20,w}$	True sedimentation coefficient at 20°C and in water
$s_{4,b}$	Apparent sedimentation coefficient at 4°C and in buffer
SAR	Structure-activity relationship
SAXS	Small angle X-ray scattering
SDS	Sodium dodecyl sulfate
SE	Sedimentation equilibrium
secs	Seconds
siRNA	Small interfering ribonucleic acid
STLC	*S*-trityl-L-cysteine
SUMO	Small ubiquitin-like modifier
SV	Sedimentation velocity
TB	Terrific broth
TBS-T	Tris-buffered saline with tween-20
TCEP	Tris(2-carboxyethyl)phosphine
TPX2	Targeting protein for Xklp2
Tris	Tris(hydroxymethyl)aminomethane
µg	Microgram

µl	Microlitre
µm	Micrometre
µM	Micromolar
UV	Ultraviolet
v-bar	Partial specific volume
η	Viscosity
ρ	Density

1 Introduction

1.1 Overview of kinesins

Kinesins are a family of proteins that belong to a larger group of proteins called molecular motors (Figure 1-1). Like its motor protein cousins — myosins and dyneins — kinesins use the energy derived from ATP hydrolysis to produce the force required for it to perform essential functions in the cell. Despite the common source of 'fuel', these motor proteins differ in the type of cytoskeletal filament they associate with and the functions they perform in the cell. Myosins bind specifically to actin filaments, while dyneins and kinesins associate with microtubules. A well-known class of myosins (myosin II) is involved in muscle contraction, while a class of dyneins (axonemal dyneins) is responsible for driving the beating of cilia and flagella. Kinesins, on the other hand, are more commonly known for axonal transport among other functions.

Kinesin was first discovered about 26 years ago by Vale *et al*. and Brady *et al*., while studying axonal transport in squid and chick brain respectively[1,2]. Subsequently named kinesin-1, it was found to be involved in the transport of organelles from the cell body to the axon of neurons. When immobilised on a glass slide, this force-generating molecule induced gliding of the added microtubules along the glass surface (Figure 1-2a). Similarly, when the microtubules were immobilised on the glass slide, kinesin was shown to carry cargo, in the form of latex beads or organelles, along the microtubule tracks[3,4] (Figure 1-2b). Although kinesin was discovered much later than myosin or dynein, its reputation as an important molecular motor was hence established.

After the sequence of the *Drosophila melanogaster* kinesin heavy chain was deposited in 1989[5], numerous families of kinesins were identified in various species, including yeast *Saccharomyces cerevisiae*, nematode *Caenorhabditis elegans*, humans and even plants. Phylogenetic analysis[6] and a standardised naming system[7] for kinesins have led to the classification of at least 14 distinct families, with each member of a family sharing sequence homology, domain organisation, motility characteristics and similar functions (Figure 1-3). To date, about 45 kinesins have been identified in humans.

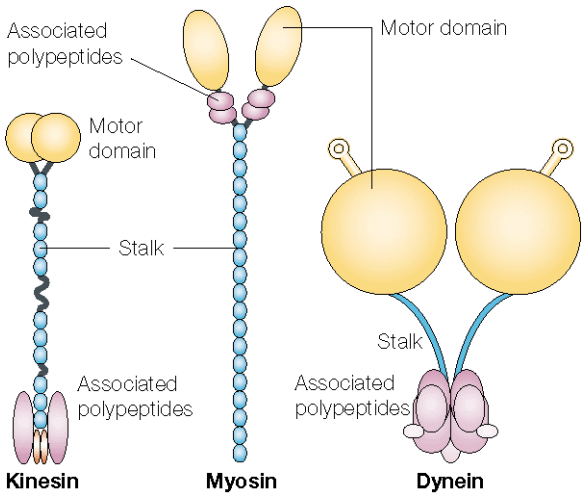

Figure 1-1. Schematic of molecular motors.

Kinesin has the smallest catalytic motor domain (yellow) among the molecular motors. The motor domain is usually associated with the stalk domain (blue). Associated polypeptides for the various molecular motors are depicted in purple. Adapted from Woehlke et al., 2000[8].

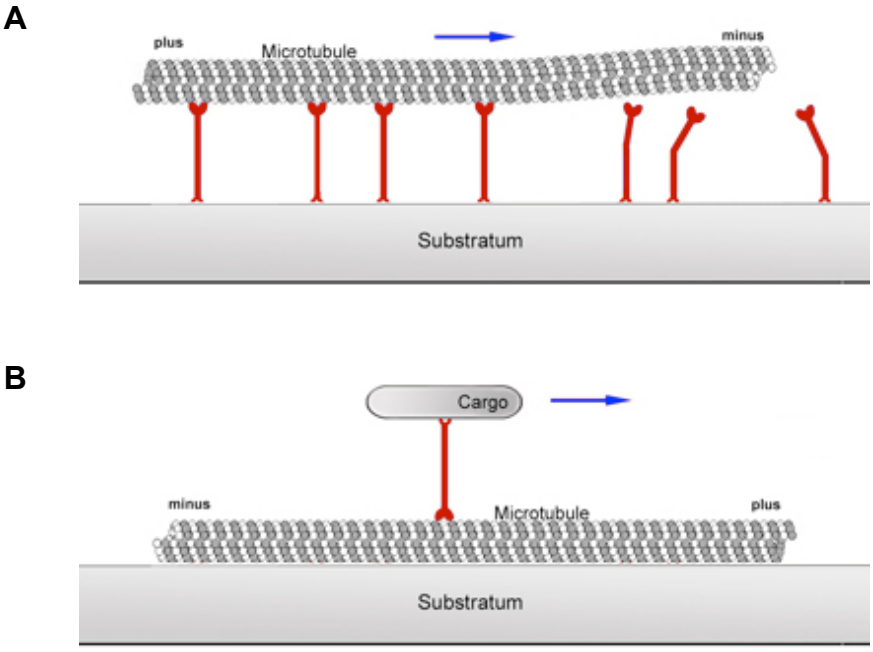

Figure 1-2. Kinesin motility assay.

(A) Kinesin molecules immobilised on a glass slide causes added microtubules to glide along the surface. **(B)** Kinesin molecule transports cargo along immobilised microtubule track. Figure adapted from http://www.fli-leibniz.de/www_elmi/Motility_assays.jpg.

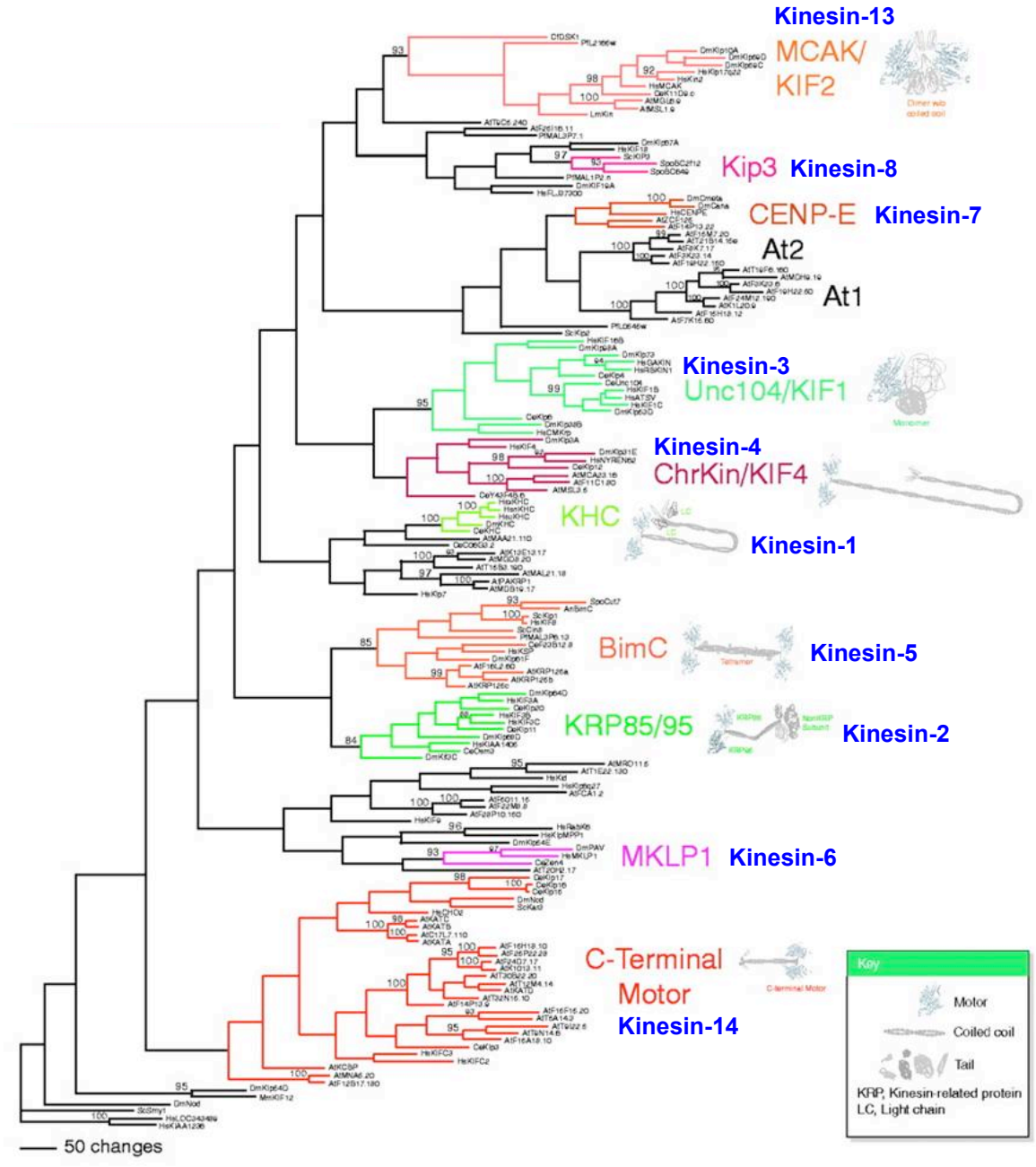

Figure 1-3. Kinesin family tree.

Phylogenetic analysis classifies kinesins into at least 14 distinct families, with each member of a family sharing sequence homology, domain organisation, motility characteristics and similar functions (Red: chromosome and spindle organisation; green: vesicular and organelle transport). The standardised nomenclature for each family of kinesins is shown in blue. Adapted from Dagenbach *et al*., 2004[9].

1.1.1 Structural organisation of kinesins

Despite their different functions, all kinesins consist of a globular motor domain, which is usually attached to a coiled-coil stalk domain of varying lengths. At the other end of the stalk domain lies a tail domain (Figure 1-3). Depending on the position of the motor domain in the molecule, kinesins are divided into three categories: N-terminal, middle or C-terminal. Those with motor domains at the N-terminal (e.g. kinesin-1) move towards the plus end of microtubules, while those with C-terminal motor domains (kinesin-14) are minus-end directed. Kinesins with motor domains in the middle of the molecule (kinesin-13) do not move in similar ways, but diffuse to the plus or minus end of microtubules to perform their function[10].

The arrowhead-shaped motor domain (~350 residues) is highly conserved as shown by crystal structures of various kinesins. It is the catalytic site for ATP hydrolysis and binding site for microtubules. It has an eight-stranded ß-sheet, surrounded by three α-helices on each side (Figure 1-4). L11-α4-L12-α5 form the microtubule-binding site and loop L8 is implicated in microtubule binding[11-14]. On the opposite side, the nucleotide occupies the active site through binding of the α- and ß-phosphates to the P-loop (GxxxxGKS/T)[15], which is conserved in G proteins, myosins and kinesins. Switch I (SSRSH) and switch II (DLAGSE) are two other highly conserved motifs that undergo conformational changes during the ATP hydrolysis cycle[16,17]. The former acts as a γ-phosphate sensor and translates local changes to a larger conformational change in the latter.

Linking the motor domain to the stalk domain is a short polypeptide called the neck linker (Figure 1-4). When the switch II cluster (formed by α4-L12-α5) shifts upwards toward the N-terminal of helix α4, the neck linker is allowed to dock parallel to the motor domain. Conversely, when it shifts downwards toward the C-terminal of helix α4, the neck linker is undocked and perpendicular to helix α6. In the ADP-bound kinesin-1 monomer structure, the neck linker is observed to be disordered and undocked[17], but becomes ordered and docked in the microtubule-bound kinesin-AMPPNP (slowly-hydrolysable ATP analogue) monomer structure[18] (Figure 1-5). A conformational change in the neck linker is believed to be pivotal in producing movement for the molecular motor.

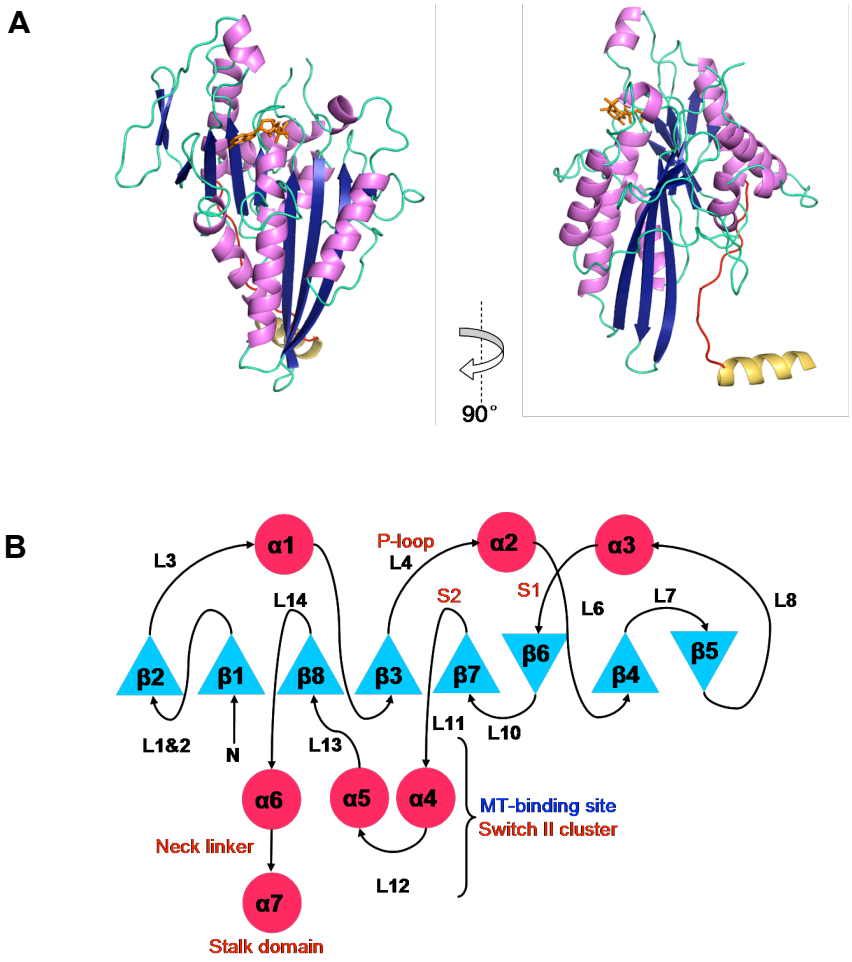

Figure 1-4. Structural organisation of the kinesin motor domain.

(A) Arrowhead-shaped motor domain consisting of an eight-stranded β-sheet (blue), surrounded by three α-helices (pink) on each side. Mg^{2+}ADP (orange) binds in the active site as shown. The neck linker (red) at the C-terminus of the motor domain links the motor to the stalk domain (yellow). (PDB ID: 2Y5W) **(B)** Simple topology of the major secondary structure elements of the motor domain. Conversed motifs, such as P-loop, switch I (S1) and switch II (S2), are shown.

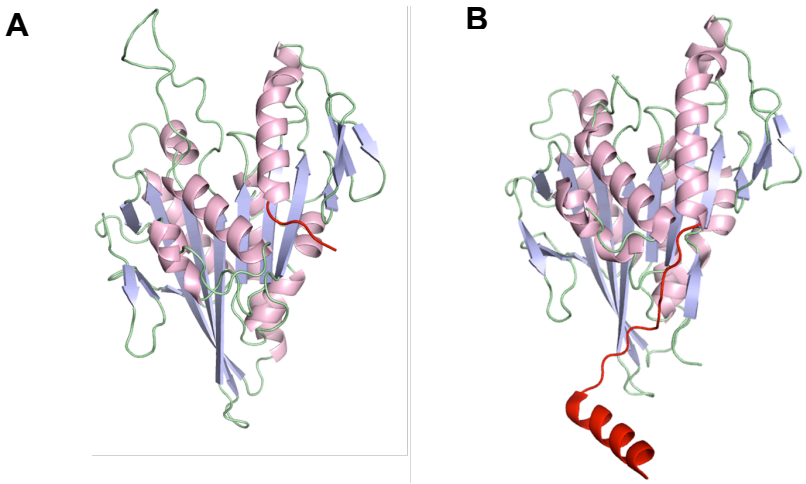

Figure 1-5. Conformational changes in the neck linker.

(A) Structure of kinesin-1 monomer showing disordered and undocked neck linker (red). (PDB ID: 1BG2[17]) **(B)** Structure of kinesin-1 monomer showing an ordered neck linker that is docked to the motor domain. (PDB ID: 1MKJ[19]) A partial helical stalk domain is shown in red.

While the neck linker is crucial for force generation, the stalk domain is essential for coordinating movement. For the majority of kinesins (e.g. kinesin-1), the stalk domain mediates dimerisation and is implicated in coordinating the movement of the kinesin motor domains along the microtubule. For kinesin-5, further oligomerisation occurs as two anti-parallel dimers interact via the stalk to form a homotetramer (Figure 1-3), which is necessary for its function in sliding anti-parallel microtubules apart[20]. Still other kinesins (e.g. kinesin-2[21]) rely on the stalk domain to associate with a different family of kinesin or with non-motor proteins. As there are no crystal structures available for the entire stalk domain of kinesin, the coiled-coil structure is generally inferred from the heptad repeats in the sequence. Using a prediction program called COILS[22], kinesin-1 is predicted to consist of an interrupted coiled-coil stalk domain. The hinges or flexible regions in the stalk domain allow it to fold back onto itself to form a compact autoinhibited molecule[23].

The tail domain of kinesin is believed to play an important role in regulating the molecular motor. When kinesin is folded into a compact form, the tail domain interacts with the motor domain and inhibits activity[24]. This prevents the squandering of ATP when kinesin is not transporting cargo or performing its functions. Another significant role of the tail domain is the binding and selection of cargo, which gives rise to the specificity of each family of kinesin for its cargo. However, in the case of kinesin-14, the tail domain does not bind vesicles or organelles, instead it binds microtubules[25,26]. Thus, both the motor and tail domains cross-link microtubules and slide them apart during spindle assembly[27]. Finally, the tail domain has also been shown to interact with kinesin-associated proteins, such as UNC-76, which could further regulate the cargo binding and transport abilities of kinesin[28].

1.1.2 Functions of kinesins

The basic function of kinesins is to transport cargo along microtubules. To this end, some kinesins are highly processive, for example kinesin-1, which takes about a hundred steps before dissociating from the microtubule track[29-31]. Each 8 nm step[32,33] requires the hydrolysis of a single ATP molecule[34], which produces a

force of 6-8 pN[35]. Ncd (kinesin-14), on the other hand, is a non-processive kinesin that dissociates from the microtubule track after each step. To overcome this problem, it does not work alone but as an array of multiple motors that bind to the microtubules alternately[36]. Although the mechanism by which kinesins move along microtubules is poorly understood, it is widely accepted that the molecular motor walks by a 'hand-over-hand' mechanism (Figure 1-6), whereby the motor domains take turns to be the leading and lagging motor[37-39].

Spanning the 14 families of kinesins is a myriad of different cellular functions that are implicated in development[40], higher brain function[41] and tumour suppression[42]. In neurons, kinesins transport vesicles, protein complexes and membranous organelles, such as mitochondria[43], either anterograde or retrograde for the development and normal functioning of neurons. Kinesins also transport vesicles and messenger ribonucleoprotein (mRNP) complexes[44] in dendrites for synaptic transmission. In cells, the roles of kinesins are aplenty. They transport vesicles, such as endosomes and lysosomes, and organelles, such as the endoplasmic reticulum and Golgi apparatus to their respective destinations in the cell[45]. Finally, kinesins also transport components of the cilia in intraflagellar transport[46]. Thus, given their many cellular functions (Figure 1-7), it is not surprising that a loss or mutation of a certain kinesin gene could result in embryonic lethality, developmental abnormalities, tumorigenesis, neuropathies, neurodegeneration[47] and dysfunction.

Apart from intracellular transport, kinesins have been discovered to be involved in cellular division[48]. Immunodepletion of kinesins in *Xenopus* eggs has shed light on the role of kinesins in the various steps of mitosis. At least 12 out of 45 human kinesins belong to this special class called mitotic kinesins that facilitate spindle assembly, chromosome segregation and cytokinesis (Figure 1-8). To start with, Eg5 (kinesin-5) is largely responsible for the separation of centrosomes and formation of the bipolar spindle[49]. CENP-E (kinesin-7)[50] and MCAK (kinesin-13)[51], among others, help to align chromosomes in metaphase. Finally, members of the kinesin-6 family are involved in cytokinesis. Although some of the mitotic kinesins are redundant and have counterparts that perform similar functions, the importance of kinesins in the regulation of cell division is undisputed.

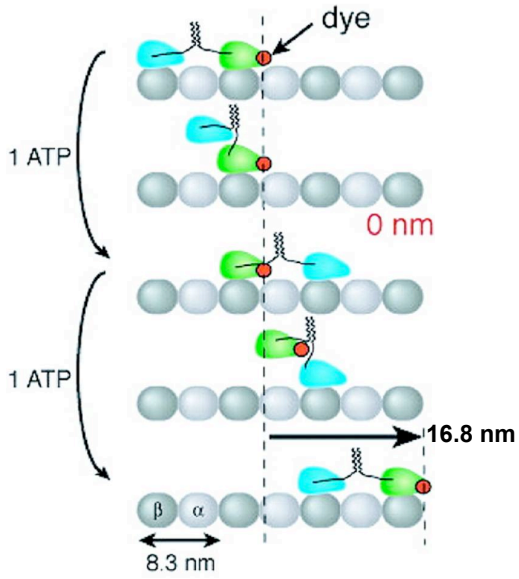

Figure 1-6. Diagram depicting the 'hand-over-hand' model of kinesin motility.

In this model, the motor domains alternate between being the leading and lagging motor. This model also predicts that for every ATP hydrolysis cycle, a dye placed on one motor will move 0 and 16.8 nm alternately. Figure adapted from Yildiz *et al*., 2004[39].

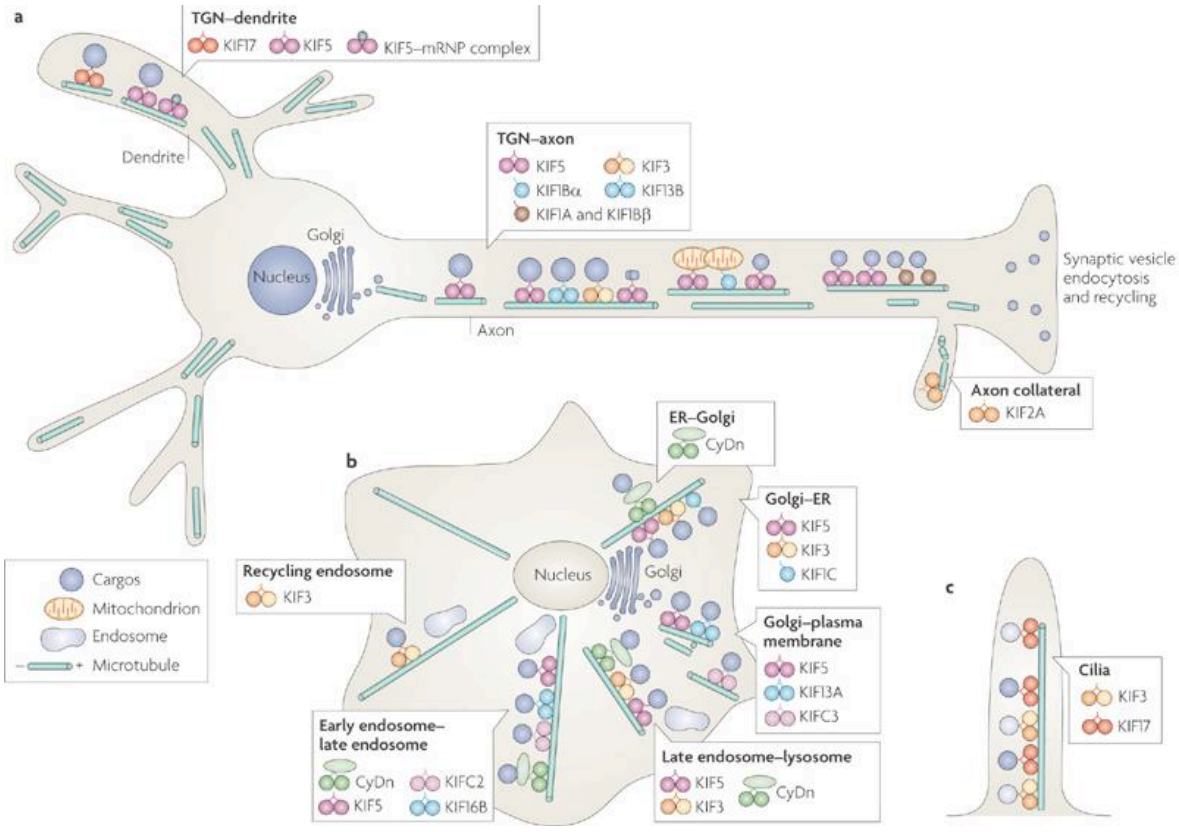

Figure 1-7. The roles of kinesin in intracellular transport.

(A) Axonal and dendritic transport of cargoes in neurons by different families of kinesins. **(B)** Kinesins transport vesicles, protein complexes and organelles to their respective locations in the cell. **(C)** An example of intraflagellar transport of vesicles by kinesins in cilia. Figure adapted from Hirokawa *et al*., 2009[52].

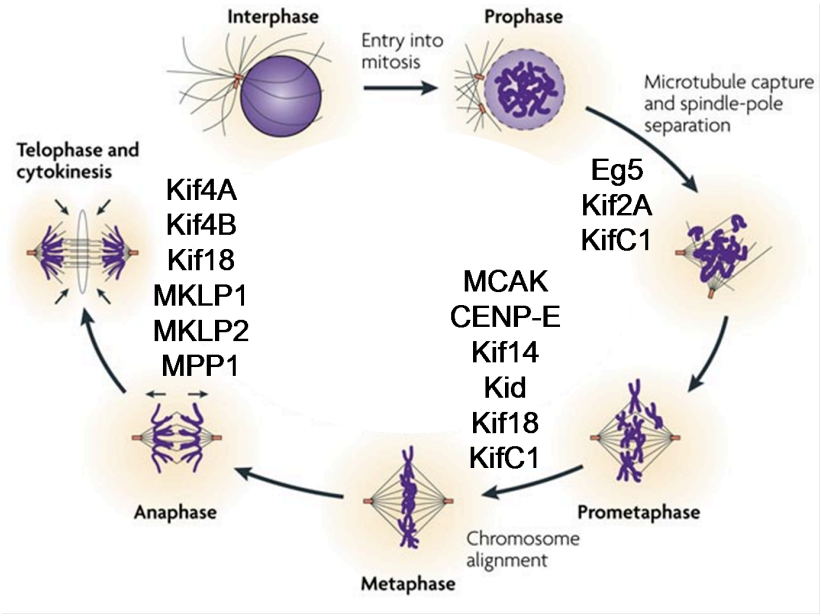

Figure 1-8. Mitotic kinesins involved in different steps of cell division.

Mitotic kinesins facilitate spindle assembly, chromosome alignment and cytokinesis. Figure adapted from Jackson *et al*., 2007[53].

1.2 *Homo sapiens* mitotic kinesin Eg5

A decade before kinesin-1 was first discovered in giant squid axons, a gene was found to be crucial in nuclear division of *Aspergillus nidulans*[54]. The temperature-sensitive mutant of this gene caused mitotic arrest soon after the cell had entered mitosis. It was given the name bim. A few years after the discovery of kinesin, a homologue of bim was discovered during a differential screening of *Xenopus* egg cDNA for genes that are necessary for nuclear division and cell proliferation[55]. This gene and bim were later classified as members of the kinesin-5 family. The human homologue (henceforth called Eg5) was then isolated and characterised by Blangy *et al*.[56]. The results showed that Eg5 indeed has a role to play in the formation of the bipolar spindle and is regulated by a protein kinase, $p34^{cdc2}$.

1.2.1 Structural organisation of Eg5

Eg5, like many other kinesins, consists of a globular motor domain of ~350 residues at the N-terminus, an interrupted α-helical coiled-coil stalk domain of

~460 residues in the middle of the protein, and a non-helical C-terminal tail domain of ~220 residues (Figure 1-9). However, unlike many kinesins that form dimers, electron micrographs of rotary-shadowed Eg5 provide evidence that it exists as a homotetramer[57] (Figure 1-10a). By forming a dimer of anti-parallel dimers, Eg5 assembles into a dumbbell-shaped bipolar kinesin with two motor domains at each end, which allows it to bind microtubules at both ends (Figure 1-10b). This quaternary structure is consistent with and can help to explain its function of cross-linking and sliding anti-parallel microtubules apart.

The structure of ADP-bound Eg5 motor domain monomer, solved by Turner *et al*.[58], has provided insights into the catalytic domain. Although it does not share a high sequence homology with other kinesins, the basic eight-stranded ß-sheet and six α-helices structure is still observed. The nucleotide-binding pocket, P-loop and switch I are also conserved. The neck linker that follows after the switch II cluster is undocked, akin to kinesin-1. Recently, a crystal structure of AMPPNP-bound Eg5 that mimics the ATP-bound state was solved[59] and it revealed a docked neck linker, which is in agreement with that of kinesin-1. However, due to the static nature of crystal structures and the fact that many kinesins do not work alone as a monomer, it would be difficult to correlate these structures with the different stages of the ATPase cycle[60,61] with great certainty.

A significant difference between the motor domain of Eg5 and other kinesins is the length of L5, which is a loop that interrupts helix α2. Consisting of ~18 residues (Glu116 to Ile133), Eg5 has the longest loop L5 of all kinesins. While its function remains unclear, biochemical and biophysical studies have shown that this loop, along with other conserved motifs like switch I, is likely to be involved in the regulation of nucleotide and microtubule binding[62,63]. During the ATPase cycle, loop L5 moves between an ‘open’ conformation, when ADP is bound[58], and a ‘closed’ conformation in the ATP state[59,64]. This in turn influences the neck linker conformation and affects force generation and movement of Eg5[62,63].

Although many crystal structures of the motor domain are available, little is known about the stalk and tail domains. As previously mentioned, the stalk domain helps facilitate the formation of an oligomer, and in this case a tetramer. It is also necessary for coordinating the ‘hand-over-hand’ movement

of the motor domains. Using the COILS program[22], the stalk is predicted to be an interrupted coiled-coil domain, with the first ~100 residues having a very high score and probability of forming a coiled-coil, while the middle ~150 residues have a very low score and probability of forming a coiled-coil (Figure 1-11). Unfortunately, without a high resolution crystal structure, the true structure and conformation of the stalk domain remains elusive.

Although there are no crystal structures of the C-terminal tail domain of Eg5, studies have revealed a number of important roles for this domain. Firstly, the association of human Eg5 with centrosomes during early prophase is regulated by the phosphorylation of Thr927 by protein kinase $p34^{cdc2}$, more commonly known as cyclin-dependent kinase 1 (Cdk1)[56]. This temporal regulation localises the protein on centrosomes and a single point mutation at this tail domain residue is sufficient to abolish interaction of the protein with the spindle apparatus. In addition, it was discovered through a yeast two-hybrid screen that the tail interacts with $p150^{Glued}$, a subunit of the dynactin complex, which could mediate the association of Eg5 with microtubules or the spindle apparatus[65]. Recently, the tail, in addition to the motor domain, was shown to bind microtubules[20,66]. The results suggest that the low processivity of Eg5[67] could be compensated by the tail domain, which continues to bind and cross-link microtubules.

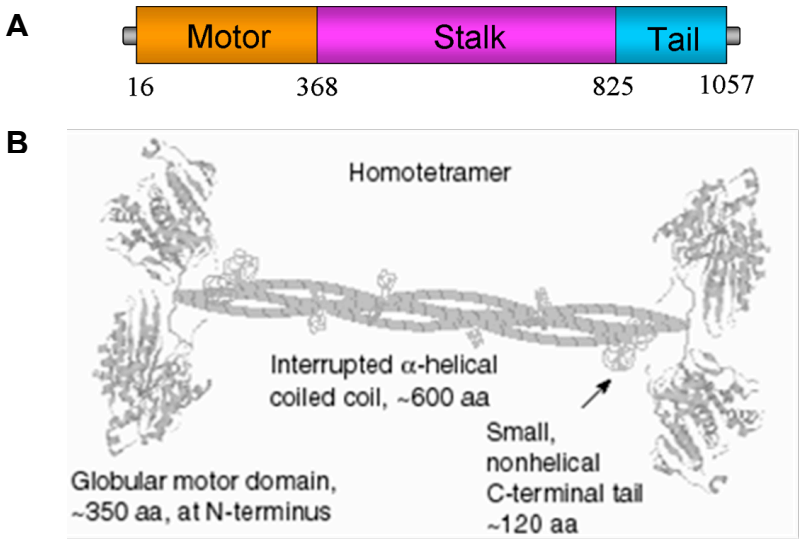

Figure 1-9. Structural domains of Eg5.

(A) Schematic diagram of full length Eg5 showing the motor, stalk and tail domains. (Not drawn to scale) **(B)** Cartoon of how Eg5 monomers may interact to form a homotetramer via interactions of the stalk domains. Figure adapted from http://www.proweb.org/kinesin/BE5a_BimC.html.

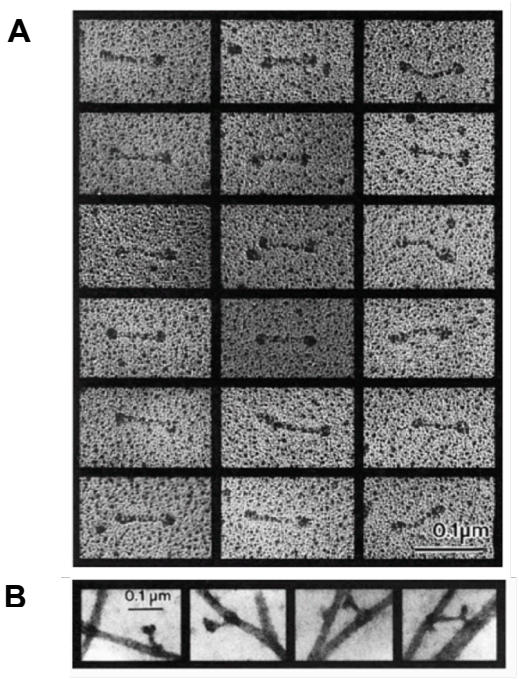

Figure 1-10. Electron micrographs of rotary-shadowed Eg5.

(A) Multiple images of dumbbell-shaped Eg5, which indicate that Eg5 exists as a homotetrameric bipolar kinesin. **(B)** Images of Eg5 binding to a single microtubule (left) and cross-linking two microtubules (right). Figure adapted from Kashina *et al*., 1996[57].

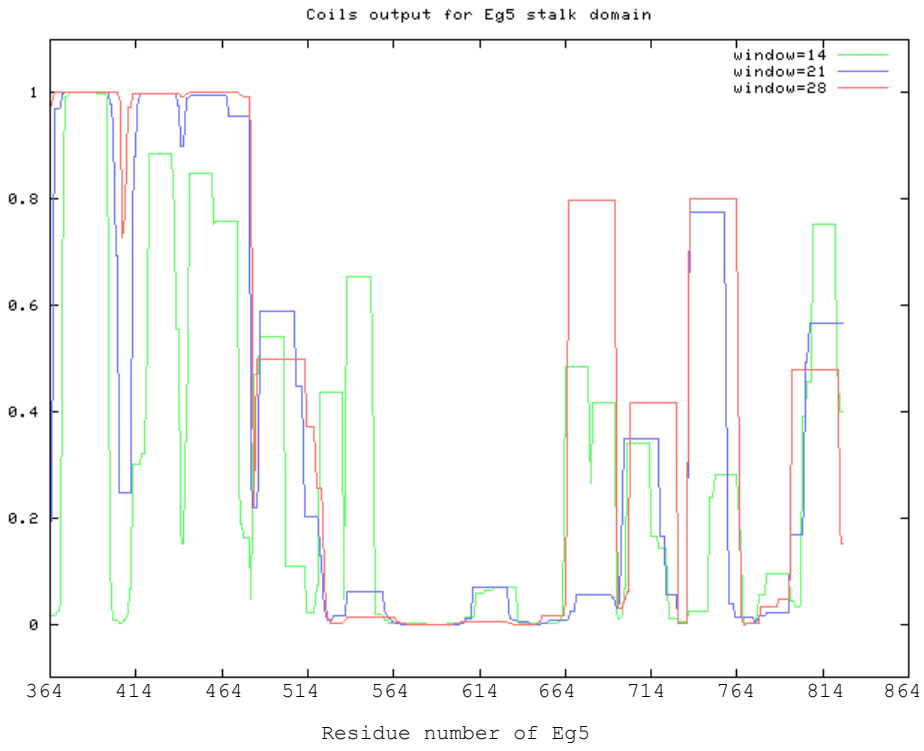

Figure 1-11. Prediction of quaternary structure of the Eg5 stalk domain.

Output from the COILS prediction program[22] shows that the first ~100 residues have a high score and probability of forming a coiled-coil structure, while the middle ~150 residues have a low probability.

1.2.2 Functions of Eg5

The main and often talked about function of Eg5 is the formation of the bipolar spindle. Many studies have used various techniques and different cell lines to probe the function of this bipolar kinesin. In the earliest study on human Eg5, Blangy *et al*.[56] showed that the inhibition of Eg5 by antibodies caused HeLa cells to arrest in mitosis with a very characteristic phenotype: cells form a monoastral spindle with an array of microtubules emanating from a pair of non-separated centrosomes (Figure 1-12). Another study using siRNA to knockdown Eg5 in PtK cells also resulted in the monopolar spindle phenotype and mitotic arrest[68]. Thus, the current model suggests that Eg5 separates the duplicated centrosomes by cross-linking antiparallel microtubules and sliding them apart, as it moves towards the plus end of microtubules (Figure 1-13).

Further investigations are in place to find out whether Eg5 works alone, synergistically or antagonistically with other molecular motors to maintain the bipolarity of the spindle. Two studies have suggested that kinesin-14 and dynein, both minus-end directed motors, could oppose the activity of Eg5[69,70]. On the other hand, kinesin-12 has been found to cooperate with or even take over the function of Eg5 in bipolar spindle formation under particular conditions[71]. While the primary function of kinesin-12 is to maintain the spindle bipolarity, it can also drive centrosome separation when Eg5 is inhibited. With the help of a microtubule-associated protein, TPX2, it appears that kinesin-12 may be able to completely replace the function of Eg5.

The other function of Eg5 is its role in developing neurons. Although Eg5 is a mitotic kinesin that is expressed in dividing neuroblasts, Ferhat *et al*.[72] showed that Eg5 continues to be expressed in postmitotic neurons. Using immunofluorescence staining with an antibody against Eg5, the molecular motor was found to be localised in the cell body, along the length of and at the distal tips of developing processes, namely the axon or dendrites (Figure 1-14). The study also suggests that unlike kinesin-1, Eg5 does not transport organelles from the cell body to the tips of neurons. Instead, Eg5 may be involved in regulating microtubule organisation and behaviour within the distal tips of developing processes, although the exact mechanism remains unclear.

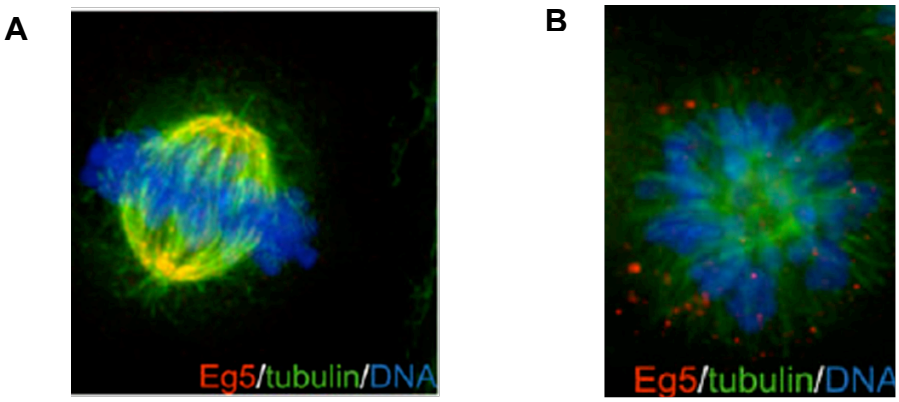

Figure 1-12. Role of Eg5 in establishing the bipolar spindle.

(A) Normal cell in a control setup showing chromosomes aligned at the metaphase plate of a bipolar spindle. **(B)** Cell arrests in mitosis with a monoastral spindle upon knockdown of Eg5 using siRNA. Figure adapted from Stout *et al*., 2006[68].

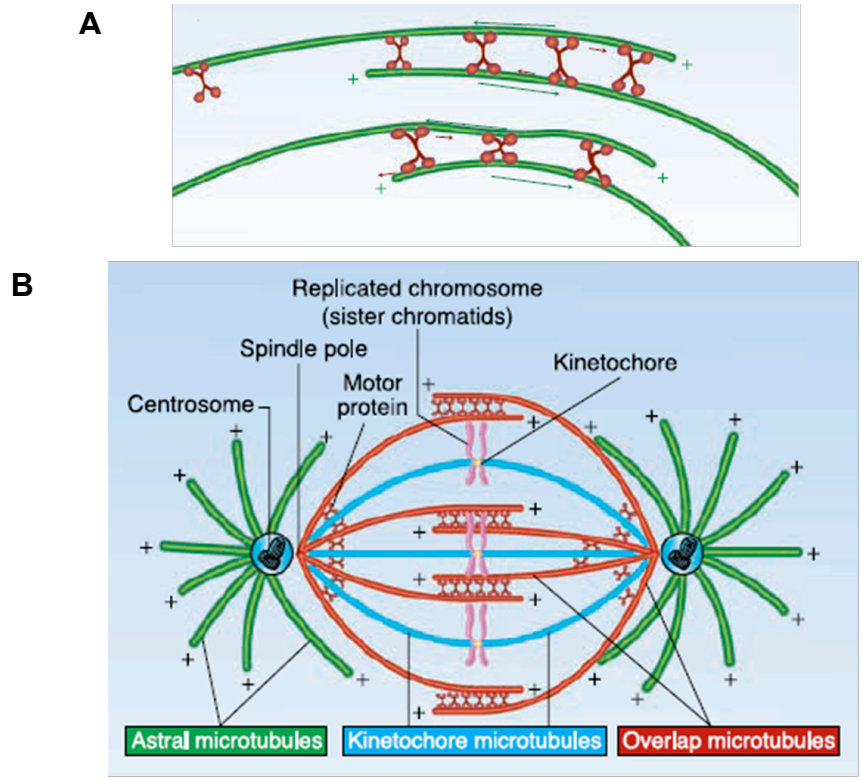

Figure 1-13. Bipolar Eg5 homotetramer cross-links and slides microtubules apart.

(A) By forming a homotetramer, Eg5 has two motor domains binding to one microtubule and the other two motor domains binding to an adjacent but anti-parallel microtubule. **(B)** As Eg5 is a plus-end directed motor, it moves towards the plus end of microtubules and in doing so, it pushes the anti-parallel microtubules apart, separates the duplicated centrosomes, and establishes the bipolar spindle. Figure adapted from Sarli *et al*., 2008[73].

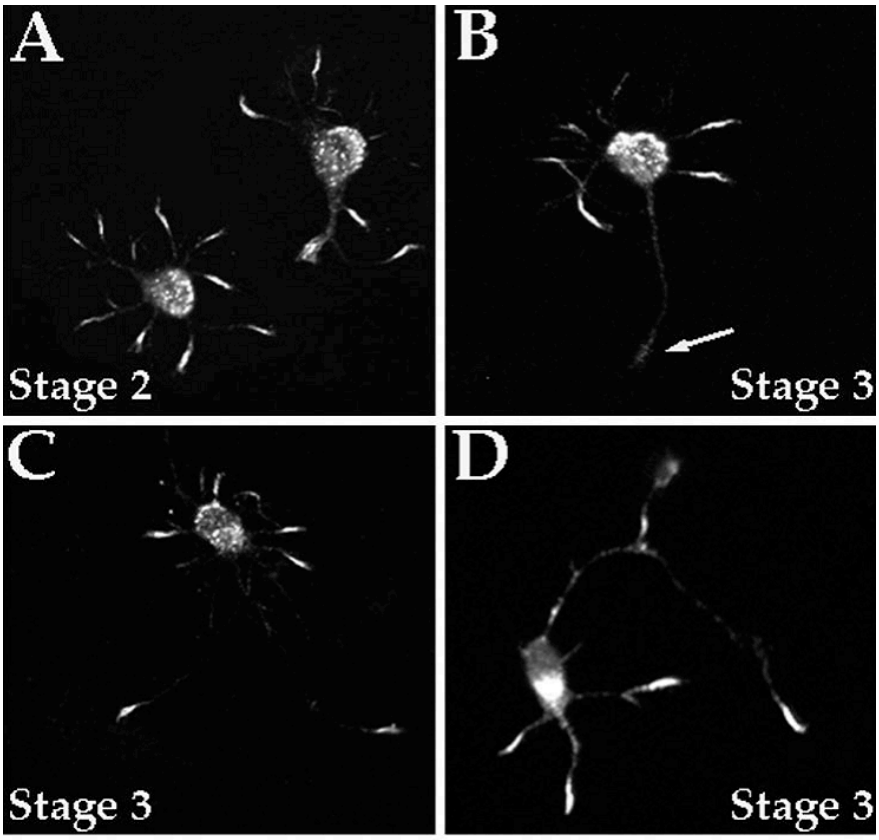

Figure 1-14. Immunofluorescence staining of Eg5 in cultured rat hippocampal neurons.

(A) At stage 2 of early development, Eg5 is localised within the cell body and at the tips of minor processes. **(B, C, D)** At stage 3, the localisation of Eg5 does not change, although in some cases, it is not observed at the distal tip of the axon (B, arrow).

More recently, Bartoli *et al.*[74] reported a new and unexpected role of Eg5 in polypeptide synthesis. In the study, Eg5 was shown to be essential for the production of normal levels of protein in the cell. When Eg5 was inhibited, an approximately 40 % decrease in proteins levels was observed after ruling out factors such as mitotic arrest and cell death. In addition, the ribosome transit time (the time during which the growing polypeptide chain remains attached to the ribosome) was also decreased. Through *in vitro* binding assays, Eg5 was shown to associate with ribosomes and act as a link between ribosomes and microtubules. This link could promote ribosome transit. Hence, Eg5 is postulated to play an important role in translation and elongation of the polypeptide chain by facilitating association of the ribosomes to the cytoskeleton and hence increasing the efficiency of the ribosomes.

1.2.3 Validated drug target for cancer chemotherapy

Over the past twenty years, taxanes and vinca alkaloids, which target tubulin and interfere with microtubule dynamics, have been used successfully in the clinics as anti-cancer drugs[75]. Although these drugs possess anti-tumour properties by impeding cell proliferation, patients treated with these drugs also suffer from microtubule-dependent side effects, such as peripheral neuropathy [76]. Given the risk of neurotoxicity caused by these drugs and the development of drug resistance by tumour cells[77-79], an alternative to microtubule-based drugs is greatly desired. Currently, several novel targets for drug development in cancer therapy, such as kinases and mitotic kinesins, have been identified. Given that the inhibition of Eg5 by antibodies and siRNA causes cells to arrest in mitosis and prolonged mitotic arrest then leads to apoptotic cell death, Eg5 has become an interesting candidate for drug development in cancer chemotherapy.

The first inhibitor of Eg5 was discovered by Mayer *et al*.[80] while conducting a phenotype-based screen for small molecules that inhibit the formation of the bipolar spindle (Figure 1-15). Out of more than 16000 compounds, they narrowed down their search to 139 compounds that caused mitotic arrest in cells. Next, using an *in vitro* tubulin polymerisation assay, they found 86 compounds that do not affect microtubule dynamics. Finally, they managed to obtain 5 hits that affected only proliferating cells undergoing mitosis. One such compound, which was found to be a specific inhibitor of Eg5, was named monastrol, because of the characteristic monoastral spindle phenotype it causes in dividing cells. Despite its relatively weak potency in cancer cells (IC_{50} = 34 μM)[81], it is the prototype small molecule inhibitor that is widely used in biochemical assays to study the functions and mechanisms of Eg5.

While efforts are underway to improve the potency of monastrol analogues[82], many other classes of Eg5-specific inhibitors are currently being investigated. Cell-based and *in vitro* assays have led to the discovery of a series of inhibitors that target Eg5. *S*-trityl-L-cysteine (STLC), from the National Cancer Institute library, was previously identified as a new Eg5 inhibitor that is 36 times more potent than monastrol[83]. STLC not only inhibits basal and microtubule-activated Eg5 ATPase activity by preventing ADP release, it also inhibits microtubule

gliding in motility assays[84]. Tumour cells treated with STLC were shown to undergo mitotic arrest through the activation of the spindle assembly checkpoint, evident by the phosphorylation of BubR1[85]. Prolonged mitotic arrest consequently led to the activation of caspase-9, cleavage of caspase-8 and accumulation of caspase-3, which is indicative of apoptosis by the intrinsic apoptotic pathway[86].

Tetrahydroisoquinolines[87] and pyrrolotriazine-4-one based inhibitors[88] are other examples of compounds that bind to the same pocket as, but exhibit greater potency than monastrol. More recently, benzimidazole inhibitors have been shown to bind to a different site and are uncompetitive with ATP[89]. This new class of inhibitors provides a strategy against resistance that may develop from mutations in the monastrol-binding pocket[90]. The specificity of new inhibitors is also a major concern in the effort to reduce side effects and improve efficacy of potential new cancer therapy. Thus, screening the potential inhibitor against a variety of kinesins would weed out those that have cross-reactivity with other families of kinesins[81]. Finally, in order to develop more potent and specific inhibitors against Eg5, a structure-based drug design approach may be pursued.

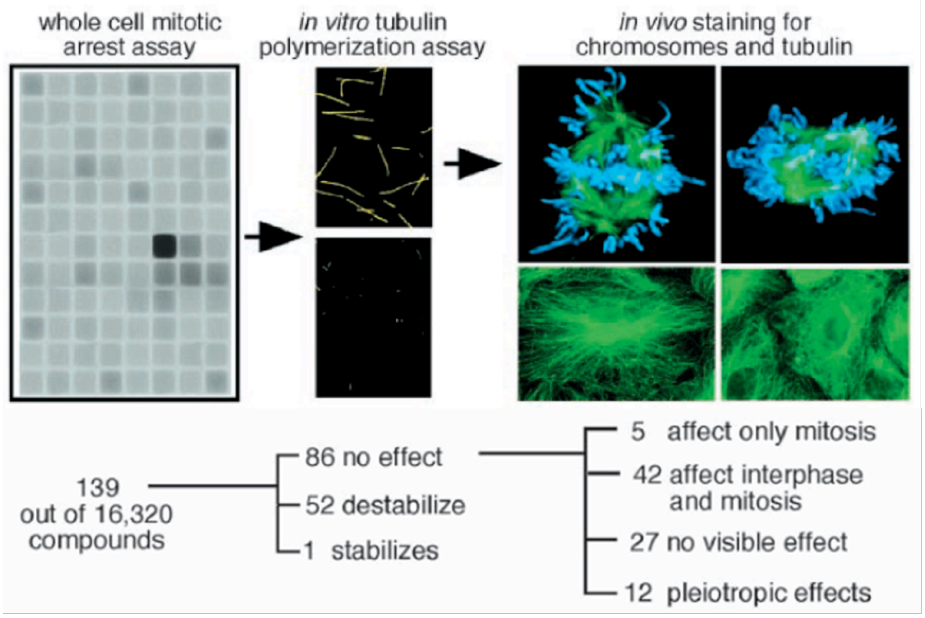

Figure 1-15. Phenotype-based screen for inhibitors of the mitotic spindle.

This diagram depicts the process that led to the discovery of monastrol, a specific inhibitor of Eg5, which causes cells to arrest in mitosis but does not have an effect on microtubule dynamics. Figure adapted from Mayer *et al*., 1999[80].

The crystal structure of Eg5 in complex with monastrol was solved by Yan *et al.*[91]. At a resolution of 1.9 Å, the ternary structure of Eg5 in complex with *S*-monastrol and Mg^{2+}ADP provides a great deal of insight into the inhibitor-binding pocket (Figure 1-16a). By comparing this structure with that of native Eg5-ADP[58], one is also able to observe several conformational changes that occur upon inhibitor binding. Firstly, to accommodate the inhibitor, Arg119 (on helix α2) and Tyr211 (on helix α3) move outward, while Trp127 of loop L5 swings downwards, by about 7 Å, from a solvent-exposed region to form an aromatic edge-to-edge π-interaction with the phenol ring of Tyr211 (Figure 1-16b). These conformational changes close the entrance of the induced-fit pocket and form a snug inhibitor-binding pocket.

Secondly, switch I, which is the γ-phosphate sensor, swings outward towards the solvent by about 6 Å (Figure 1-17) in the inhibitor-bound structure. It also transforms from a loop in the native Eg5-ADP structure to a short helix in the inhibitor-bound complex. Conformational changes in and around the inhibitor-binding pocket also translate to changes at helix α4, α5 and the neck linker. Helix α4 and α5, which form the switch II cluster, shift upwards towards the N-terminal of helix α4; thus, opening space for the neck linker to assume a docked conformation parallel to the motor domain (Figure 1-17). These conformational changes observed in the crystal structure were further confirmed by Maliga *et al.*, in a study using spectroscopic probes to dissect the structural changes caused by monastrol binding[92].

A closer look at the inhibitor-binding pocket reveals that it is bordered by helix α3, loop L5 and helix α2. A total of about 20 residues surround the inhibitor. This pocket is about 12 Å away from the nucleotide pocket, thus monastrol is considered an allosteric or ATP-noncompetitive inhibitor. By studying the interactions between the inhibitor and the motor domain, one can think of ways to improve the potency of the small molecule. The 3-hydroxy group on the phenyl ring forms hydrogen bonds with several residues (Glu118, Ala133 and Arg119) of the motor domain. The phenyl ring also forms a C—H---π interaction with Pro137 and π-π interactions with Trp127 and Tyr211. Lastly, the oxygen in the carbonyl group of the ketone forms a hydrogen bond with Arg119 (Figure 1-18).

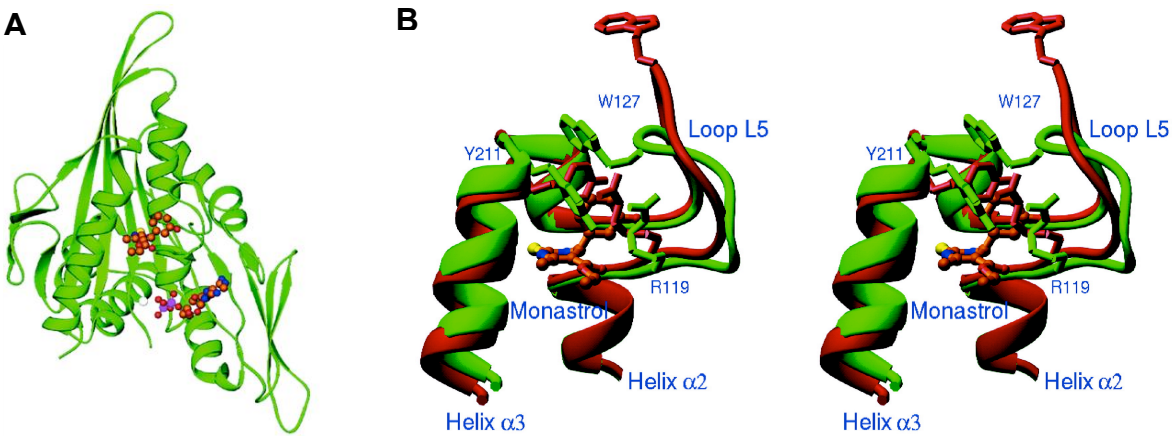

Figure 1-16. Structure of Eg5-ADP-monastrol complex.

(A) Overall structure of the ternary complex (PDB ID: 1X88). The inhibitor and nucleotide are represented by ball-and-stick models (C = orange, N = blue, S = yellow, O = red). **(B)** Stereoplot showing the conformational changes (before = red, after = green) that take place upon inhibitor binding. Loop L5 swings downwards to close the pocket. Figure adapted from Yan *et al.*, 2004[91].

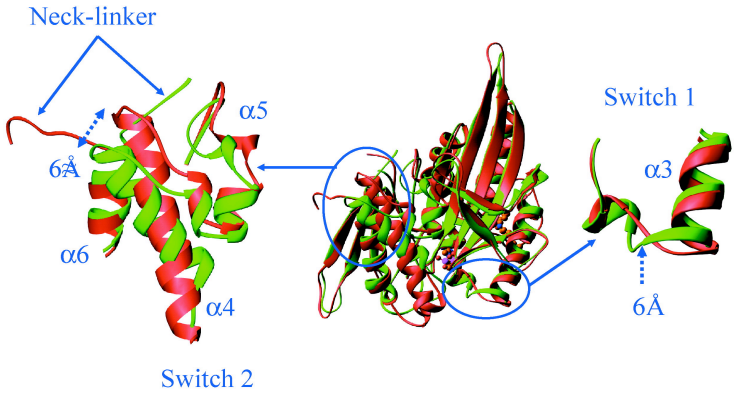

Figure 1-17. Conformational changes in switch I, switch II cluster and neck linker upon inhibitor binding.

Switch I swings towards the solvent, while the neck linker docks onto the motor domain. (before = red, after = green). Figure adapted from Yan *et al.*, 2004[91].

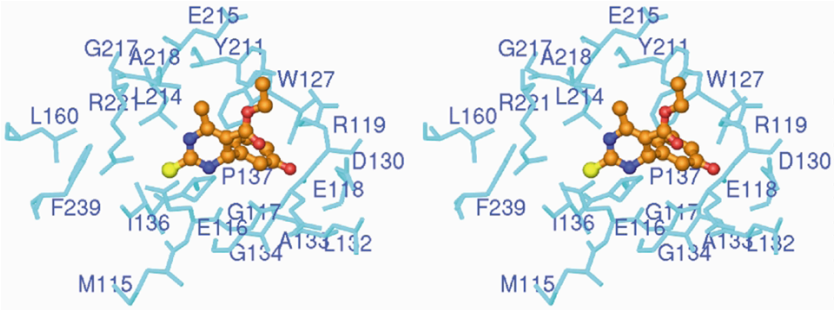

Figure 1-18. Stereoplot of Eg5-monastrol inhibitor-binding pocket.

Monastrol (ball-and-stick model) forms hydrogen bonds, π-π interactions and C—H---π interaction with the motor domain residues (light blue). Figure adapted from Yan *et al.*, 2004[91].

As more potent inhibitors are being developed through structure-based drug design, rigorous testing in tumour cell lines and mouse xenographs are required to determine the efficacy of the compounds *in vivo*. Various classes of inhibitors have been tested on paediatric cancers, pancreatic cancer and glioblastoma cell lines and xenografts. The results proved to be very encouraging, as complete responses, tumour regression and total eradication of tumours have been observed in the respective mouse xenograft models[93-95]. In addition, taxane-resistant prostate and ovarian cancer cell lines were shown to be sensitive and responsive to Eg5 inhibitors[96,97]. The treated cells arrested in mitosis and consequently died by apoptosis. As Eg5 inhibitors work via a different mode of action compared to microtubule-targeting drugs, multidrug resistance that arise from the mutation of tubulin subunits will not pose a problem for the former.

Besides being able to overcome drug resistance that may develop due to long term usage of taxanes and vinca alkaloids, Eg5 inhibitors are also relatively more specific against cancer cells. While microtubule-targeting drugs would affect all cells containing microtubules, Eg5 inhibitors would only kill cells that are rapidly proliferating, in particular various cancers, such as pancreatic cancer and leukaemias, that have been shown to possess an elevated expression profile of Eg5[98,99]. Although the overexpression of Eg5 may be a consequence of cancer cells naturally having a higher mitotic index, Castillo *et al.*[100] showed that overexpressing Eg5 in mice resulted in chromosome instability, which is a newly identified hallmark of cancer[101], and predisposed the mice to the development of tumours. Ultimately, whether the high expression levels of Eg5 is a result of rapidly proliferating cancer cells or the overexpression of Eg5 results in the development of cancers, one cannot deny that Eg5 inhibitors are relatively more specific than microtubule-binding drugs.

In conclusion, seven specific inhibitors are currently in Phase I and II clinical trials. The best studied compound, ispinesib, was developed by Cytokinetics and GlaxoSmithKline, and was the first to enter into human trials[102]. Other compounds include MK-0731 by Merck and ARRY-520 by Array BioPharma. All these compounds have been shown to be highly potent against tumour cell proliferation and have IC_{50} in the low nanomolar range (<10 nM). The Phase I study of ispinesib showed that it is well-tolerated, safe and did not cause

neurotoxicity in patients with solid tumours[103-105]. The results underscore the use of drugs that do not affect microtubule dynamics, as they do not cause serious and often irreversible peripheral neuropathy in patients. Nevertheless, side effects such as fatigue, nausea and neutropenia are unavoidable.

Phase II study of ispinesib in a large range of adult solid tumours revealed greatest activity of the drug in breast, ovarian and non-small cell lung carcinoma. The most promising results were shown in advanced and metastatic breast cancer patients treated with ispinesib, as half of the number of patients enrolled experienced stable disease for up to half a year[106]. Unfortunately, the use of ispinesib in the treatment of other solid tumours did not yield any significant response. Thus, the future direction would be to test ispinesib and more potent analogues, such as SB 743921, in combination with other chemotherapeutics, in hope of achieving a synergistic effect.

1.3 *Drosophila melanogaster* kinesin-1

The founding member of kinesins, discovered about 26 years ago, used to be called conventional kinesin, as it was believed to be the archetypal kinesin. After the discovery of other families of kinesins that possess different characteristics and structural organisation, and with the implementation of a standardised nomenclature, it became known as kinesin-1. While it was first discovered in squid and chick, homologues of this ubiquitous kinesin have now been found in many other organisms, such as human, fruit fly and fungus. Here, we focus on the *D. melanogaster* homologue of kinesin-1, whose sequence was the first to be deposited[5], and describe its structure, function, motility and regulation.

1.3.1 Structural organisation of kinesin-1

The first insight into the structure of kinesin-1 came from electron micrographs of rotary-shadowed bovine kinesin-1. Images revealed a ~80 nm rod-shaped molecule that contains a pair of globular domains at one end and a fan-shaped

structure at the other end[107]. Addition of monoclonal antibodies against the kinesin heavy chain labeled the globular domains, while antibodies against the kinesin light chain decorated the fan-shaped structure (Figure 1-19). From these results, it was inferred that kinesin-1 is a heterotetramer consisting of two heavy chains and two light chains (Figure 1-20a).

The heavy chain of *D. melanogaster* kinesin-1 (henceforth called kinesin-1) is made up of an N-terminal globular motor domain (~360 residues) that is linked to the stalk domain via a neck linker[5] (Figure 1-20b). Similar to other kinesins, the motor domain is the catalytic site for ATP hydrolysis and the binding site for microtubules. The neck linker is believed to not only provide the 'power stroke', but also to determine directionality[108-110]. The coiled-coil stalk domain (~500 residues), which facilitates dimerisation, is interrupted in at least two positions by kinks or hinges that confer flexibility to the molecule. This allows the molecule to fold back onto itself, such that the N-terminal motor domain comes into contact and interacts with the C-terminal tail domain (~40 residues). This folded conformation is believed to be the inhibited form of the molecular motor[111]. About 150 residues preceeding the tail domain is a predicted coiled-coil region that is involved in cargo binding and association with the kinesin light chain[112]. At 508 residues long, the kinesin light chain determines the specificity of cargo being transported by kinesin-1.

The motor domain has been intensively studied and three crystal structures of the motor domain monomer are available: human, rat and fungal kinesin-1[17,113,114]. They provide insight into the overall structure, nucleotide-binding site and conserved motifs within the catalytic core. The motor domain has the same fold as that of other kinesins: eight major ß-strands in the core, surrounded by three major α-helices on each side. The nucleotide-binding site and motifs, such as the P-loop, switch I and II are also conserved. However, as the kinesin-1 heavy chain exists as a dimer, it is also important to study the structure of a dimer to understand how the molecular motor works. The first kinesin-1 dimer structure was solved by Kozielski *et al.* and it revealed a 120° rotational symmetry between the *Rattus Norvegicus* kinesin-1 monomers[115] (Figure 1-21). Although the structure revealed a small portion of the stalk domain being intertwined as a coiled-coil, there were no interactions between the catalytic core and the stalk.

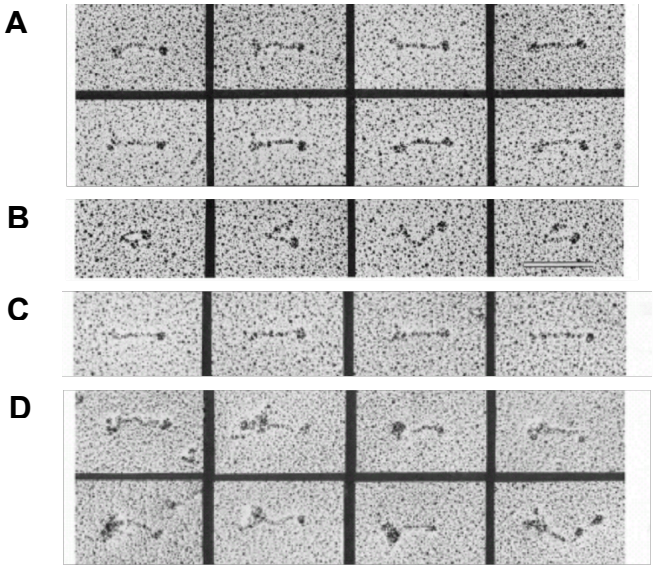

Figure 1-19. Electron micrographs of rotary-shadowed bovine kinesin-1.

(A) Heterotetrameric kinesin-1 consisting of a pair of globular domains on one end and a fan-shaped structure on the other end. **(B)** Kinesin-1 molecule folded at a hinge in the stalk domain. **(C)** Antibodies against the heavy chain label the globular domains. **(D)** Antibodies against the light chain label the fan-shaped structure. Figure adapted from Hirokawa *et al*., 1989[107].

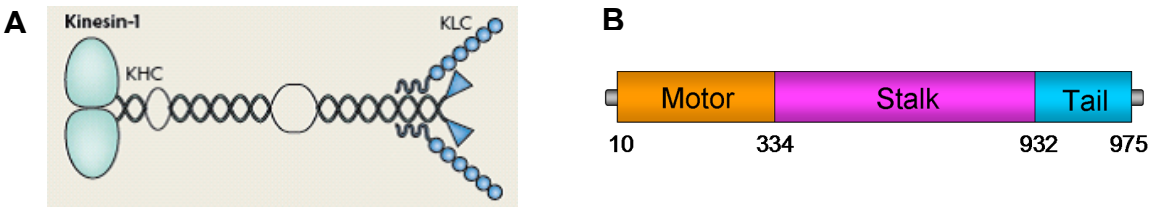

Figure 1-20. Structural domains of kinesin-1.

(A) Cartoon of kinesin-1 heterotetramer formed by two kinesin heavy chains (KHC, consisting of the motor, stalk and tail domains) and two kinesin light chains (KLC). Figure adapted from Verhey *et al*., 2009[116]. **(B)** Schematic diagram of the full length kinesin-1 heavy chain (not drawn to scale).

Figure 1-21. Crystal structure of *R. norvegicus* kinesin-1 dimer.

Monomers exhibit a rotational symmetry of ~120° about an axis close to the coiled-coil domain (PDB ID: 3KIN[115]).

1.3.2 Functions of kinesin-1

When kinesin-1 was first discovered in squid axon, it was found to be involved in anterograde axonal transport of vesicles and organelles from the cell body to the tips of neurons. While there is no doubt about its role in axonal transport, the specific functions of kinesin-1 are not well understood. Thus, in order to probe the exact functions of kinesin-1, genetic studies were carried out in both larva and adult *D. melanogaster*[117]. The results from the studies indicate that the kinesin-1 heavy chain is essential for the viability of the larva, as mutations in both alleles proved to be lethal, but a cloned copy of wild-type heavy chain rescued lethality. The mutant hemizygotes were not spared either as they suffered growth abnormalities, such as slower growth and reduction in size, especially in the posterior regions. This is evident in the skinny and tapered tails of hemizygous mutants, compared with the broad and blunt-end tails of wild-type larva.

Besides growth abnormalities, hemizygote larvae also experienced behavioural changes and neuromuscular malfunction. By measuring their rate of crawling and feeding, it was found that they were more sluggish than their wild-type counterparts. This could be linked to loss of neuromuscular function in the posterior region, as the mutant larvae were observed to use only their anterior half in their crawling motion, while dragging their paralysed tail along. In addition, their posterior region also lacked tactile sensitivity, as they did not respond when touched with a needle. Having ruled out necrosis of the tissues in the posterior region, it became apparent that an impaired kinesin-1 function results in growth abnormalities, motor and sensory impairment of the posterior end.

A temperature-sensitive mutant of the kinesin-1 heavy chain tested in adult flies revealed similar results: sluggish movements characterised the homozygous mutant flies. Furthermore, behavioural depression, in the form of reduced courtship, mating and minimal response to stimuli, was observed when the flies were cultured in restrictive temperature. On the other hand, the temperature-sensitive mutant tested in embryos saw no effect on proliferation and embryogenesis. In short, all these data come together to show that kinesin-1

heavy chain is essential for proper development and neuronal function, in particular motility, tactile sensation and behaviour. Loss of function of this molecular motor causes lethality but does not impede cellular division in embryogenesis.

However, the question remains as to how the role of kinesin-1 in axonal transport affects normal physiological function in neurons. To answer this, Gho *et al.*[118] dissected the molecular mechanism and showed that the kinesin-1 heavy chain is required for action potential propagation in axons and the release of neurotransmitters at the nerve ends. However, it was shown that the kinesin-1 mutant does not impair neurotransmitter release by reducing transportation of synaptic vesicle components. Instead, the authors postulate that kinesin-1 may be essential for the anterograde transport of vesicles that carry ion channels, presynaptic membrane or protein components to their respective locations, where they will be inserted or incorporated.

In light of the role of kinesin-1 in axonal transport, the molecular motor has been linked to several diseases in human. Firstly, it is implicated in Alzheimer's disease after it was found that amyloid precursor protein (APP) binds to kinesin-1 light chain[119]. Recently, Kif5B (one of the three isoforms of kinesin-1 in humans) was identified to form a complex with two neurofibromatosis tumour suppressors[120]; thus linking the molecular motor to cancer. Finally, kinesin-1 is linked to certain viral infections, as it was found to be necessary for the transport of vaccinia virus and herpes viruses[121,122]. With a better understanding of how kinesin-1 works in each of these diseases, strategies that target the molecular motor could be employed to combat these diseases.

1.3.3 Motility of kinesin-1

In order for kinesin-1 to perform its functions, it must possess two important characteristics: directional motility and processivity. As mentioned earlier, the plus-end directed kinesin-1 is highly processive, as it takes about a hundred steps before dissociating from the microtubule[29-31]. Each step spans 8 nm and is coupled to the hydrolysis of a single ATP molecule[32,34]. Initially, an 'inchworm'

model, whereby one motor domain will always be leading, was proposed for kinesin-1 motility[123] (Figure 1-22). The study involved immobilising the tails of a kinesin dimer to a surface, adding microtubules to the motor domains and observing their movement. If the kinesin dimer moves by a symmetric 'hand-over-hand' model, one would expect the microtubule to rotate by 180°. However, the microtubules did not show any rotation relative to the immobilised kinesin dimers; thus, a symmetric 'hand-over-hand' model was ruled out.

Subsequently, three separate experiments were carried out and the results were shown to be inconsistent with the 'inchworm' model. Firstly, Kaseda *et al.*[38] produced and observed the movement of a heterodimeric kinesin, consisting of a wild-type motor and a mutant motor domain that hydrolyses ATP at a slower rate. It was found that the kinesin moved at an alternating fast and slow speed, consistent with the 'hand-over-hand' model, whereby the two motors step alternately (Figure 1-22). The same result was also observed by Asbury *et al.*[124], who used homodimeric kinesin containing different truncated lengths of the stalk domain. The limping movement (alternate fast and slow motion) of the homodimer was strong evidence for the 'hand-over-hand' model.

Finally, using the direct method of labelling and visualising a single motor domain as it moves, Yildiz *et al.*[39] showed that the probe moved a distance of about 16.6 nm for every other ATP hydrolysis cycle. This experiment dealt the final blow to the 'inchworm' model. Nevertheless, the finer details of the 'hand-over-hand' model are still unclear. Therefore, several groups have produced electron cryomicroscopy (cryo-EM) maps of microtubules decorated with kinesin-1 monomers or dimers, with different nucleotides bound, to create images of kinesins in each step of the processive motion[13,125-128]. By docking the kinesin-1 monomer or dimer crystal structure onto microtubules, one can observe the binding pattern and position of each motor domain and attempt to model motility on microtubules.

In general, all the maps agree on the position of the bound motor domain monomer: at the crest between the α- and ß- tubulin heterodimer. In the case of a dimer, the second unattached motor domain was observed to point towards the direction of movement, which is the plus end for kinesin-1 (Figure 1-23).

However, the position of the second motor domain is a point of contention, with two propositions: it is free[125] or tethered to the first motor domain[126]. Consequently, Hoenger *et al.*[129] advised caution when interpreting these helically averaged three-dimensional maps, as they may represent an average of several conformational states. Also, the concentration of kinesin dimers used to decorate the microtubules could affect the position of the unattached motor.

Nonetheless, with the available biophysical data, crystal structure of kinesin-1 dimer and cryo-EM maps, Hoenger *et al.*[129] attempted to model the 'hand-over-hand' mechanism. In doing so, they realised that unlike human feet that have handedness, kinesin-1 dimer consists of two identical motor domains that would overwind and produce torsional stress on the stalk if it moves in a symmetric mode. Therefore, an asymmetric mode is proposed whereby each motor domain undergoes a different conformational change as it takes a step forward (Figure 1-24). This would mean that the final conformation after taking a step is different from that at the beginning, allowing the neck linker to wrap and unwrap itself. In short, to dissect the details of motility, more biophysical data, crystal structures and cryo-EM maps of different states of motility are needed.

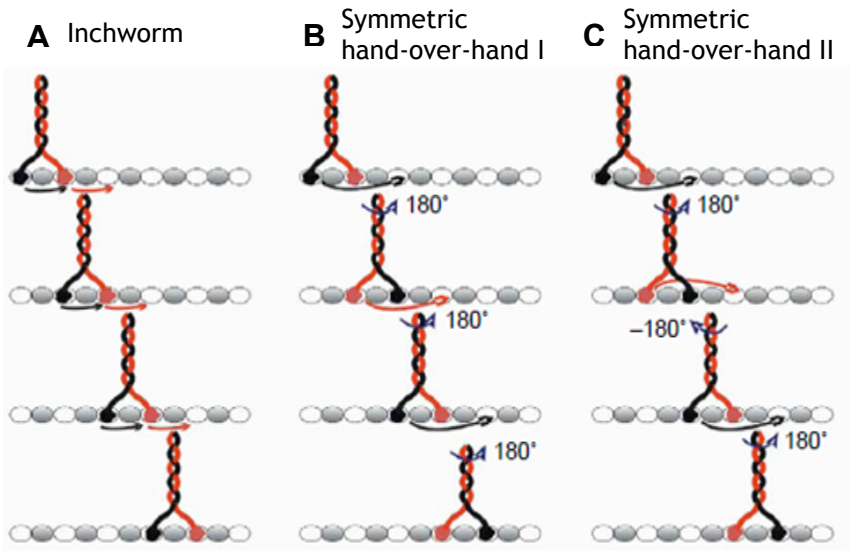

Figure 1-22. Models of motility of kinesin-1.

(A) Inchworm model where one motor domain is always the leading motor. **(B)** Symmetric hand-over-hand model with the lagging motor always passing the front motor to the left or to the right. This model is symmetric because the conformation of each motor is the same at the beginning and end of each step. **(C)** Symmetric hand-over-hand model with the lagging motor passing the front motor alternately from the left and right side. Figure adapted from Yildiz *et al.*, 2005[130].

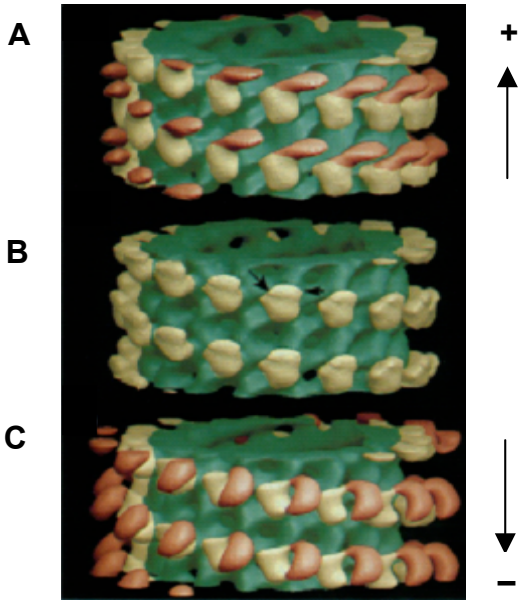

Figure 1-23. Cryo-EM maps of microtubule decorated with kinesins.

Tubulin protofilaments are in green, attached motor in cream and unattached motor domain in orange. **(A)** Kinesin-1 dimer, **(B)** kinesin-1 monomer and **(C)** kinesin-14 Ncd dimer. The unattached motor domain points towards the direction of motility. Figure adapted from Hirose *et al*., 1996[120].

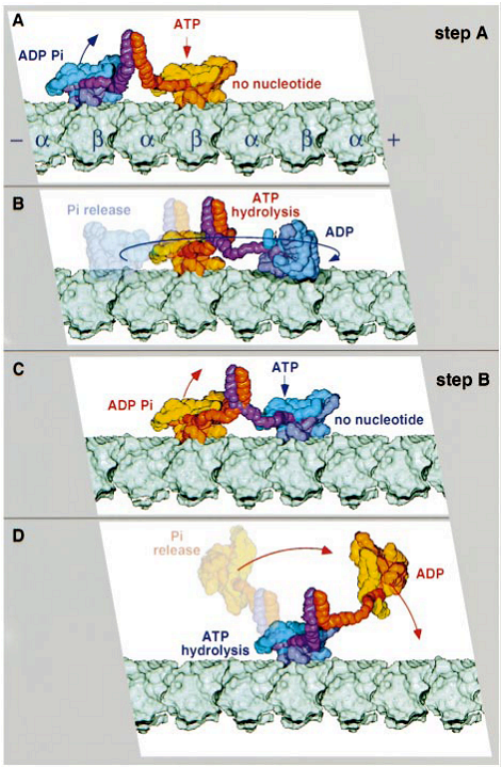

Figure 1-24. Cartoon depiction of asymmetric hand-over-hand motility of kinesin-1.

Each motor domain undergoes a different conformational change as it takes a step forward. This would mean that the conformation of each motor at the end of a step is different from the conformation at the beginning of the step. In this model, the neck linker is able to wrap and unwrap itself to relieve over winding and torsional stress build up. Figure adapted from Hoenger *et al*., 2000[121].

1.3.4 Autoinhibition of kinesin-1

When kinesin-1 is not transporting cargo along the microtubule track, it has to be regulated to prevent squandering of ATP and overcrowding of the microtubule highway. To this end, the molecular motor adopts a compact and folded conformation, through an autoinhibitory mechanism, that keeps it inactive in the absence of cargo[23,131,132] (Figure 1-25). This folded and compact structure has been shown to be the default conformation of the molecule at physiological ionic concentration[111]. By folding into a compact structure, the tail comes into close proximity with the motor domain and interacts with it with tight affinity ($K_d \approx$ 20-40 nM)[133,134]. Although the tail domain can bind to microtubules, the interaction of the tail and motor domains has been shown to reduce the affinity of kinesin-1 to microtubules. This in turn inhibits microtubule-stimulated ADP release[24]. However, it was later discovered that the tail can inhibit ADP release from the motor domains even in the absence of microtubules[135].

While it is generally accepted that the folded structure inactivates the molecular motor, the exact mechanism as to how the tail autoinhibits the motor domain is not well understood. An idea put forward is that kinesin-1 may go by the same autoinhibition mechanism that keeps myosin II in a compact inactive conformation, whereby the tail loops around and binds to the motor domain. Using mutational studies and truncated constructs, several studies have narrowed down the site of interaction between the tail and motor domains to the IAK region of the tail[23,126]. This region is highly conserved among metazoan and fungal kinesin-1[24,136]; thus, further supporting its role in the regulation of kinesin-1 (Figure 1-26).

The sequence immediately before the IAK region, called the auxiliary binding site (ABS) region, is positively-charged and conserved among metazoan but not fungal kinesin-1 (Figure 1-26). While it helps to increase the affinity of the tail to motor domains, the ABS region alone is not sufficient to cause autoinhibition in metazoan kinesin-1, let alone fungal kinesin-1 that lacks this region. Therefore, the ABS region is not implicated in the binding to motor domains, but

may play a secondary role as a binding site for the kinesin light chain, which coincidentally is lacking in fungal kinesin-1[134].

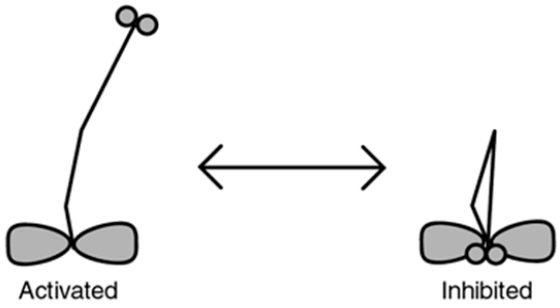

Figure 1-25. Cartoon of how kinesin-1 may be inhibited.

Kinesin-1 is activated when it in an extended conformation. It becomes inhibited when the tail binds to the motor domains in a compact folded structure. Figure adapted from Coy *et al*., 1999[132].

```
Dm    121 DIFNHIYAMEVNLEFHIKVSYYEIYMDKIRDLLDVSKVNLSVHEDKNRVPYVKGATERFV  180
Hs-A  115 DIFNHIYSMDENLEFHIKVSYFEIYLDKIRDLLDVTKTNLSVHEDKNRVPFVKGCTERFV  174
Hs-B  114 DIFNYIYSMDENLEFHIKVSYFEIYLDKIRDLLDVSKTNLSVHEDKNRVPYVKGCTERFV  173
Hs-C  115 DIFDHIYSMDENLEFHIKVSYFEIYLDKIRDLLDVSKTNLAVHEDKNRVPYVKGCTERFV  174
Sp    113 DIFNHIYQMDESLEFHIKVSYFEIYMDRIRDLLDVSKTNLSVHEDKNRVPFVKGATERFA  172
Lp    114 DIFNYIYGMDENLEFHIKISYYEIYLDKIRDLLDVTKTNLAVHEDKNRVPFVKGATERFV  173
          ***  ** *.  ******.**.***.*.*******.* **.*********.***.****
Nc    118 QIFTSILSSAANIEYTVRVSYMEIYMERIRDLLAPQNDNLPVHEEKNRGVYVKGLLEIYV  177

Dm    181 SSPEDVFEVIEEGKSNRHIAVTNMNEHSSRSHSVFLINVKQENLENQKKLSGKLYLVDLA  240
Hs-A  175 SSPEEILDVIDEGKSNRHVAVTNMNEHSSRSHSIFLINIKQENMETEQKLSGKLYLVDLA  234
Hs-B  174 CSPDEVMDTIDEGKSNRHVAVTNMNEHSSRSHSIFLINVKQENTQTEQKLSGKLYLVDLA  233
Hs-C  175 SSPEEVMDVIDEGKANRHVAVTNMNEHSSRSHSIFLINIKQENVETEKKLSGKLYLVDLA  234
Sp    173 SSPEEVMDVIEEGKSNRHIAVTNMNEHSSRSHSIFLIQVKQENMETKKKLSGKLYLVDLA  232
Lp    174 SSPEEVMEVIDEGKNNRHVAVTNMNEHSSRSHSVFLINVKQENVETQKKLSGKLYLVDLA  233
          .**..... . *.*** ***.**************.***..**** .. .************
Nc    178 SSVQEVYEVMRRGGNARAVAATNMNQESSRSHSIFVITITQKNVETGSAKSGQLFLVDLA  237

                                                  + +    ++
Dm    890 RCTMERVKALETALKEAKEGAMRDRKRYQYEVDRIKEAVRQKHLGRRGPQAQIAKPIRSG  949
Hs-A  866 RATAERVKALEGALKEAKEGAMKDKRRYQQEVDRIKEAVRYKSSGKRGHSAQIAKPVRPG  925
Hs-B  868 RATAERVKALESALKEAKENASRDRKRYQQEVDRIKEAVRSKNMARRGHSAQIAKPIRPG  927
Hs-C  870 RATAERVKALESALKEAKENAMRDRKRYQQEVDRIKEAVRAKNMARRAHSAQIAKPIRPG  929
Sp    865 RATSERVKALEMSLKETKEGAMRDRKRYQQEVDRIREAVRQRNFAKRGSSAQIAKAIRAG  924
Lp    869 RATMERVKSLESALKDAKEGAMRDRKRYQHEVDRIKEAVRQKNLARRGHAAQIAKPIRPG  928
          *.* ****.** .**..**.* .*..*** *****.****  .   .*   ***** .* *
Nc    870                                  RGLGTDAGLGGFSIGSRIAKPLRGG  894
```

Figure 1-26. Sequence alignment of selected metazoan and fungal kinesin-1s.

Conserved residues and motifs as shown by multiple seqence alightment using ClusterW. Conserved residues in the motor domains are highlighted by red boxes. The IAK region is highlighted by a green box, while the positively-charged ABS region is shown by a blue box. Dm: *Drosophila melanogaster* (GI:125414); Hs-A,B,C: *Homo sapiens* isoforms (GI:143811412, GI:417216, GI:3043586); Sp: *Strongylocentrotus purpuratus*, sea urchin (GI:10270); Lp: *Loligo pealii*, squid (GI:125415); and Nc: *Neurospora crassa* (GI:6016437).

Recent studies have shown that the monomeric tail domain is sufficient for tight binding to and half-site inhibition of the dimeric motor domain[133]. This unexpected finding raises questions as to what the role of the second tail domain might be. Using a yeast two-hybrid screen, Gindhart *et al.*[28] showed that the tail domain binds to UNC-76. A loss of UNC-76 function resulted in impaired axonal transport; thus, it could probably help to regulate the cargo binding and transport ability of kinesin-1. Besides binding to kinesin-associated proteins, the tail domain is also involved in cargo binding and it has been shown that the addition of cargo, in the form of beads, activates a previously inhibited kinesin-1[132].

Several models have been proposed to explain the role of the tail domain in inhibiting the motor: 1) the tail domain could block the microtubule binding site of the motor domain and cause steric inhibition, 2) the tail domain could bind to and induce a conformational change in the motor domain, resulting in allosteric inhibition, and 3) the tail domain could bind to the neck linker and adjacent coiled-coil region of the motor domain, which is implicated in the 'power stroke', thus inhibit movement[23]. However, Coy *et al.*[132] has shown that the tail domain is not a competitive inhibitor by measuring enzymes kinetics. Since the tail domain does not compete with microtubules for the binding to the motor domain, the steric inhibition model is unlikely. The model in which the tail domain binds to the neck coiled-coil region is also not highly plausible. This is because Friedman *et al.*[131] showed that a mutation in the neck coiled-coil region greatly, but not completely, relieved the tail-mediated inhibition of movement.

Finally, only the allosteric model of inhibition has been supported by structural information in the form of an 8 Å cryo-EM map of a photochemically cross-linked motor-tail complex on microtubules. It revealed simultaneous interaction of the tail domain with the motor domain switch I region and the microtubule[137]. The authors propose an allosteric model, whereby the binding of the tail to the motor domain induces a conformational change and the release of ADP is prevented; hence, the motor domain is halted in an ADP state on the microtubule track. Nevertheless, further confirmation of this allosteric model would be necessary before it is set in stone.

1.4 Objectives of the thesis

Since its discovery 26 years ago, a great amount of work has been done to characterise the structures and functions of various families of kinesins. The knowledge gained has allowed us to better understand the molecular mechanism of each of its functions. However, where there are gaps in our knowledge of kinesins and where there are contradictions in proposed hypotheses, further investigations need to be carried out. To this end, the objectives of this thesis are:

1) To determine the crystal structures of mitotic kinesin Eg5 in complex with various inhibitors for structure-activity relationship (SAR) studies. The structural information obtained will facilitate structure-based drug design of more potent and specific inhibitors of Eg5, by revealing important interactions in the inhibitor-binding pocket. Consequently, these inhibitors may be developed as potential drugs for cancer chemotherapy.

2) To dissect the pathway of conformational changes that occurs when an inhibitor binds to Eg5. Such structural information will allow us to better understand the molecular mechanism of inhibition of Eg5 by potential cancer chemotherapeutics.

3) To determine the thermodynamic parameters, such as binding affinity, enthalphy changes, entropy changes and stoichiometry of interaction between Eg5 and its inhibitors, using Isothermal Titration Calorimetry (ITC).

4) To determine the oligomerisation state and sedimentation coefficient of a portion of the Eg5 stalk domain using Analytical Ultracentrifugation (AUC).

5) To investigate the secondary structure of a portion of the Eg5 stalk domain using Circular Dichroism (CD). This will give us a clue to the actual structure of the stalk domain.

6) To determine the structure of a portion of the Eg5 stalk domain in solution using Small Angle X-ray Scattering (SAXS). The structural information will give us a glimpse of the overall shape of the polypeptide.

7) To determine the crystal structure of the kinesin-1 motor domain dimer, in order to make available additional structural information for the docking of the kinesin dimer to microtubules in cryo-EM maps and the modeling of kinesin motility.

8) To determine the crystal structure of the kinesin-1 motor domain dimer in complex with the tail domain. Comparison of this structure with the motor domain dimer structure will elucidate the molecular mechanism of kinesin-1 autoinhibition. This structural information will also serve to validate or invalidate current proposed models of autoinhibition.

9) To verify the essential residues involved in the binding of the tail to the motor domains during autoinhibition, through a peptide array.

2 Material and methods

All reagents used are purchased from Sigma Aldrich, unless otherwise stated. Reagents that are used for molecular biology techniques and protein purification are of molecular biology grade. Reagents used in crystallisation are of the highest purity available.

2.1 Mitotic kinesin Eg5 motor domain

2.1.1 Molecular cloning of recombinant plasmid

The motor domain of human Eg5 (residues 1-368) was initially cloned into the pET28a vector[138]. It was then cut with restriction enzymes NcoI and XhoI (New England Biolabs, NEB) and cloned into a modified pProExHT expression vector (Invitrogen), yielding a PreScission protease-cleavable N-terminal hexahistidine-tagged protein.

2.1.2 Expression and purification of protein

The plasmid was transformed into BL21 Star (DE3) pLysS competent *Escherichia coli* (Invitrogen). Six liters of bacterial culture were grown at 37°C in Terrific Broth (TB) supplemented with 100 mg/l ampicillin to an A_{600} of approximately 0.7 and induced overnight with 0.5 mM isopropyl ß-D-thiogalactopyranoside (IPTG, Melford) at 18°C. Harvested cells were resuspended in buffer A (50 mM PIPES pH 6.8, 2 mM $MgCl_2$, 250 mM NaCl and 20 mM imidazole) supplemented with 1 mM PMSF, 1 mM MgATP, and 2.5 mg lysozyme, and subjected to one cycle of freeze-thaw and sonication, before 1 mM DNaseI and 10 mM $MgCl_2$ were added. Sonication was carried out using the Vibra-Cell VCX 750 sonicator (Sonics & Materials, Inc.) with a 13 mm probe, at 70 % amplitude and 8 x 8 secs pulses with an 8-secs pause in between each pulse.

Clear lysate was loaded onto a 5 ml HisTrapFF column (GE Healthcare) equilibrated in buffer A. The resin was washed with buffer A containing 50 mM

imidazole and the proteins were eluted on a gradient of buffer A from 50 mM to 500 mM imidazole. Fractions containing protein of interest were pooled and the buffer was exchanged for protease buffer (50 mM PIPES pH 6.8 and 250 mM NaCl). 0.5 mg of PreScission protease, 1 mM MgATP, and 2 mM $MgCl_2$ were added to the protein sample (~40 mg of Eg5) and the reaction was incubated overnight at 4°C. Uncleaved protein and protease were removed by NiNTA affinity chromatography. The cleaved protein was subjected to size exclusion chromatography on a Superdex75 column (GE Healthcare) equilibrated in gel filtration buffer (50 mM PIPES pH 6.8, 50 mM KCl, 1 mM DTT, 1 mM EGTA and 1 mM $MgCl_2$). Fractions containing the protein of interest were pooled and concentrated on an Amicon Ultra filtration device (Millipore), with size exclusion limit of 30 kDa, to a final concentration of approximately 20 mg/ml, frozen in liquid nitrogen, and stored at -80°C.

2.1.3 Crystallisation of Eg5-inhibitor complexes

2.1.3.1 Eg5 in complex with enastron, dimethylenastron or fluorastrol

Purified Eg5 (10 mg/ml) was incubated with 2 mM of inhibitor in DMSO for 1 hr on ice and centrifuged at 13000 rpm for 5 mins at 4°C to pellet undissolved inhibitor before setting up of crystal trays. Crystals of Eg5 with enastron appeared 2 days after micro-seeding crystals of Eg5 with monastrol into hanging-drops of 1 µl of Eg5-enastron complex mixed with 1 µl of reservoir solution containing 25 % PEG-3350, 0.2 M K_2HPO_4 and 0.1 M HEPES pH 8.0 in VDX plates (Hampton Research) at 4°C. A hexagonal-shaped crystal with dimensions of approximately 0.1 x 0.1 x 0.1 mm was immersed in cryoprotectant solution (30 % PEG-3350, 0.24 M K_2HPO_4, 0.12 M HEPES pH 8.0, 60 mM KCl and 20 % erythritol) and flash frozen in liquid nitrogen.

Crystals of Eg5 with dimethylenastron crystallised 4 days after micro-seeding crystals of Eg5 with monastrol into hanging-drops of 1 µl of Eg5-dimethylenastron complex mixed with 1 µl of reservoir solution containing 28 % PEG-3350, 0.2 M K_2HPO_4 and 0.1 M HEPES pH 6.5 in VDX plates at 4°C. Hexagonal-shaped crystals with dimensions of approximately 0.1 x 0.1 x 0.1 mm were immersed in

cryoprotectant solution (33.6 % PEG-3350, 0.24 M K_2HPO_4, 0.12 M HEPES pH 6.5, 60 mM KCl and 20 % erythritol) and flash frozen in liquid nitrogen.

Crystals of Eg5 with racemic fluorastrol appeared after 1 day in hanging drops by mixing 1 µl of protein-inhibitor complex with 1 µl of reservoir solution containing 30 % PEG-3350, 0.2 M K_2HPO_4 and 0.1 M HEPES pH 8.0 in VDX plates at 4°C. A block-shaped crystal with dimensions of approximately 0.1 x 0.1 x 0.1 mm was immersed in cryoprotectant solution (30 % PEG-3350, 0.24 M K_2HPO_4, 0.12 M HEPES pH 8.0, 0.3 M NaCl and 20 % erythritol) and flash frozen in liquid nitrogen.

2.1.3.2 Eg5 in complex with S-trityl-L-cysteine (STLC) or 6

Purified Eg5 (10 mg/ml) was incubated with excess STLC powder (Novabiochem) overnight at 4°C. Purified Eg5 (20 mg/ml) was incubated with 2 mM **6** (in DMSO) for 2 hrs on ice. Before setting up of crystal trays, the sample was centrifuged at 13000 rpm for 5 mins at 4°C to pellet undissolved inhibitor. Crystals of Eg5 with STLC appeared after 1 month in hanging drops by mixing 2.5 µl of protein-inhibitor complex with 2.5 µl of reservoir solution containing 22 % PEG-3350, 0.15 M sodium tartrate dibasic dihydrate and 0.1 M MES pH 6.5 in VDX plates at 4°C. A block-shaped crystal with dimensions of approximately 0.1 x 0.1 x 0.3 mm was immersed in cryoprotectant solution (24 % PEG-3350, 0.18 M sodium tartrate dibasic dihydrate, 0.12 M MES pH 6.5, 0.06 M KCl and 20 % erythritol) and flash frozen in liquid nitrogen.

Crystals of Eg5 with **6** appeared after 1 month in hanging drops by mixing 2.5 µl of protein-inhibitor complex with 2.5 µl of reservoir solution containing 25 % PEG-3350, 0.15 M sodium tartrate dibasic dihydrate and 0.1 M MES pH 6.0 in VDX plates at 4°C. A block-shaped crystal with dimensions of approximately 0.1 x 0.1 x 0.2 mm was immersed in cryoprotectant solution (24 % PEG-3350, 0.24 M sodium sulphate decahydrate, 0.12 M MES pH 6.5, 0.06 M KCl, and 20 % erythritol) and flash frozen in liquid nitrogen.

2.1.3.3 Eg5 in complex with compound 7, 8 or 9

Purified Eg5 (20 mg/ml) was incubated with 2 mM *rac*-**7**, **8** or **9** (in DMSO) for 2 hrs on ice. Crystals of Eg5 with *rac*-**7** appeared after 1 week in hanging drops by mixing 1 µl of protein-inhibitor complex with 0.2 µl of 1 M potassium sodium tartrate tetrahydrate and 1 µl of reservoir solution containing 23 % PEG-3350, 0.25 M ammonium sulphate and 0.1 M MES pH 5.5 in VDX plates at 4°C. Dehydrating solution (33 % PEG-3350, 0.25 M ammonium sulphate, 0.1 M potassium sodium tartrate tetrahydrate, 0.1 M MES pH 5.5 and 10 % glycerol) was added slowly to the crystal droplet until the total volume of the drop was eight times the original. The drop was then equilibrated against air in 4°C for 30 mins. A cubic crystal with dimensions of approximately 0.1 mm on each side was then flash frozen in liquid nitrogen.

Crystals of Eg5 with **8** appeared after 4 days in hanging drops by mixing 1 µl of protein-inhibitor complex with 1 µl of reservoir solution containing 22 % PEG-3350, 0.25 M ammonium sulphate, 0.1 M potassium sodium tartrate tetrahydrate and 0.1 M MES pH 5.8 in VDX plates at 4°C. A thick needle-shaped crystal with dimensions approximately 0.1 x 0.01 x 0.01 mm was immersed in cryoprotectant solution (27.6 % PEG-3350, 0.36 M of ammonium sulphate, 0.12 M MES pH 5.5, 0.06 M KCl and 20 % erythritol) and flash frozen in liquid nitrogen.

Crystals of Eg5 with **9** appeared after 1 week in hanging drops by mixing 1 µl of protein-inhibitor complex with 1 µl of reservoir solution containing 22 % PEG-3350, 0.3 M ammonium sulphate, 0.1 M MES pH 5.5 and 0.01 M trimethylamine hydrochloride in VDX plates at 4°C. Dehydrating solution (32 % PEG-3350, 0.36 M of ammonium sulphate, 0.12 M MES pH 5.5, 0.012 M trimethylamine hydrochloride and 10 % glycerol) was added as described above. A cubic crystal with dimensions of approximately 0.1 mm on each side was then flash frozen in liquid nitrogen.

2.1.4 Data collection and processing

2.1.4.1 Eg5 in complex with enastron, dimethylenastron or fluorastrol

The diffraction data for the Eg5-enastron and Eg5-dimethylenastron crystals were measured at the European Synchrotron Radiation Facility (ESRF) on ID23-1. The diffraction data for the Eg5-fluorastrol crystal was measured at beamline ID14-1. Assistance for data collection was provided by local contact Dr. Sandor Bruckhauser. The data for Eg5-fluorastrol was processed using HKL2000/Scalepack[139]; the data for Eg5-enastron and Eg5-dimethylenastron were processed using iMOSFLM[140] and scaled using Scala[141] from the CCP4 suite of programs[142]. The calculation of R_{free} used 5 % of data.

2.1.4.2 Eg5 in complex with STLC or compound 6

Diffraction data for Eg5-STLC and Eg5-**6** were recorded at the ESRF on station ID23-1 and ID29 respectively, with the assistance of local contact Dr. David Flot. The crystals belonged to space group $P3_2$. Data were processed using iMosflm[140] and Scala[141] from the CCP4 suite of programs[142] . The calculation of R_{free} used 5 % of data. As the space group $P3_2$ is prone to crystal twinning, we carefully examined the cumulative distribution function in ctruncate and found no indication of twinning[143]. In addition, we submitted the data to the Merohedral Crystal Twinning Server[144], which also confirmed the absence of any significant twinning.

2.1.4.3 Eg5 in complex with compound 7, 8 or 9

Diffraction data for the Eg5-inhibitor complexes Eg5-**7** and Eg5-**9** were recorded at the ESRF ID23-2 with the assistance of Dr. Gordon Leonard, while Eg5-**8** was recorded at ID23-1 with the assistance of Dr. Alexander Popov. Data were processed using iMosflm[140] and scaled using Scala[141] from the CCP4 suite of programs[142]. The calculation of R_{free} used 5 % of data.

2.1.5 Structure determination and refinement

2.1.5.1 Eg5 in complex with enastron, dimethylenastron or fluorastrol

The structures of all the complexes were solved by molecular replacement with MolRep[145] from the CCP4 suite of programs[142] using the Eg5 molecule in the Eg5-monastrol structure as a search model (PDB Code: 1X88)[146]. The two molecules in the asymmetric unit were positioned and refined with Refmac5 using rigid body refinement followed by restrained refinement[147]. Electron density and difference density maps were all σ_A-weighted, inspected and the models were rebuilt and improved using Coot[148]. The ligand coordinates and the cif dictionaries for the refinement were obtained using the Dundee PRODRG server[149]. Model geometry was analyzed using Procheck[150] and the figures were prepared using PyMOL[151].

2.1.5.2 Eg5 in complex with STLC or compound 6

The structures were solved by molecular replacement (MolRep[145]) using one molecule of Eg5 in the Eg5-monastrol structure (PDB code: 1X88)[146] as a search model. Three subunits were positioned and refined with Refmac5[147] for STLC and with simulated annealing using Phenix[152] for compound **6**. Electron-density and difference density maps all σ_A-weighted, were inspected and the model was improved using Coot[148]. The coordinates and the cif dictionary for the inhibitor molecule were calculated using the Dundee PRODRG server[149]. Model geometry was analysed using Procheck[150]. 96.49 % (880) of the residues are in the preferred regions, 2.30 % (21) are in the allowed regions, and 1.21 % (11) are outliers as shown by the Ramachandran Plot. Figures are prepared using PyMOL[151].

Since 3rd generation radiation was used for data collection, the crystal suffered slight radiation damage. The refined difference fourier map showed some negative density around the sulphur atom of STLC in all three molecules and also around the sulphur atoms of other residues at the surface. We also observed negative density around the sulphur atom of **6** in molecules B and C, but not in molecule A of the Eg5-**6** structure. As sulphur atoms absorb more photons, at

wavelength of about 1 Å, compared to other atoms (C, O & N) present in the protein, the radiation damage on sulphur is greater compared to that of the other atoms. Moreover, sulphur atoms that are more exposed (present at the surface) or are in close proximity to solvent water molecules experience more profound effect due to secondary radiation damage from the water molecules[153,154]. These negative densities could therefore be a result of radiation damage during data collection.

2.1.5.3 Eg5 in complex with compound 7, 8 or 9

The structures Eg5-**7**, Eg5-**8** and Eg5-**9** were solved by molecular replacement (Phaser[155]) using one molecule of Eg5 motor domain from structures with PDB code 3KEN[156], 1X88[146] and 3KEN[156] respectively. Refinement was carried out with Phenix[152]. Electron-density and difference density maps all σ_A-weighted, were inspected and the model was improved using Coot[148]. Model geometry was analysed using Molprobity[157]. For the Eg5-**7** complex, 95.2 % (316) of the residues are in the preferred regions, 3.61 % (12) are in the allowed regions, and 1.20 % (4) are outliers. For the Eg5-**8** structure, 95.7 % (2106) of the residues are in the preferred regions, 3.54 % (78) are in the allowed regions, and 0.77 % (17) are outliers as shown by the Ramachandran Plot. For the Eg5-**9** complex, 97.0 % (322) of the residues are in the preferred regions, 2.7 % (9) are in the allowed regions, and 0.3 % (1) are outliers. Figures are prepared using PyMOL[151].

2.1.6 Isothermal Titration Calorimetry (ITC)

ITC experiments were performed using a VP-ITC Isothermal Titration Calorimeter (MicroCal), with the assistance of Dr. Nahoum Anthony at the University of Strathclyde. Prior to performing the experiments, the motor domain of human Eg5 (residues 1-368) was cloned, expressed and purified as previously described (sections 1.1.1 and 1.1.2), apart from the following changes: the protein was incubated with 5 mM EGTA and 5 mM EDTA for 30 mins at 4°C before size exclusion chromatography was carried out to remove all nucleotides[64], and the gel filtration buffer contained no $MgCl_2$. The concentration of the protein was

measured in 6.7 M guanidine hydrochloride (buffered with 20 mM potassium dihydrogen phosphate at pH 7.0) using UV spectrophotometry at 280 nm and an extinction coefficient of 21200 M^{-1} cm^{-1}. The protein, diluted to about 1 mg/ml, was then dialysed in 20 mM PIPES pH 6.8, 300 mM NaCl, 2 mM ß-mercaptoethanol, 5 mM $MgCl_2$ and 500 µM ADP overnight at 4°C. 1 % DMSO was added to the dialysed protein before freezing the protein aliquots in liquid nitrogen and storing at -80°C.

The inhibitors, ispinesib and STLC, were prepared in the dialysis buffer mentioned above to concentrations of 250 µM and 200 µM respectively and the final concentration of DMSO in each inhibitor sample is 1 %. Protein samples were centrifuged at 13000 rpm for 5 mins at room temperature (rtp) prior to the experiment. Protein and inhibitors were degassed immediately before use. All titrations were carried out at 25°C with a stirring speed of 351 rpm. 10 µl of inhibitor was injected 26 times, with spacings of 240 secs, into the cell containing 24 µM Eg5 motor domain with 1 % DMSO.

For control experiments, the inhibitors were injected into dialysis buffer supplemented with 1 % DMSO. The heats of dilution were then subtracted from the respective inhibitor titrations before proceeding with data analysis using the Origin 5.0™ program (MicroCal). Two titrations were performed for each Eg5-inhibitor interaction and analysed separately. Thermodynamic parameters obtained, such as *N* (stoichiometry), K_a (association constant), ΔH (enthalpy change) and ΔS (entropy change), were then averaged from the two titrations. K_d (dissociation constant) was calculated using equation 1.

$$K_d = 1 / K_a \qquad \text{Equation 1}$$

2.2 Mitotic kinesin Eg5 stalk$_{364-520}$ domain

2.2.1 Molecular cloning of recombinant plasmid

Polymerase chain reaction (PCR) was carried out to amplify residues 364-520 from human Eg5 cDNA and to include restriction sites BamHI and XhoI. HotStar HiFidelity DNA Polymerase was used according to the manufacturer's protocol (Qiagen). The forward and reverse primers used were 5'-CGT ATG GGA TCC GAA GTG AAT CAG AAA CTC ACC-3' and 5'-CGT AGA CTC GAG TTA CTT ACG ATC CAG TTT GGA ATG G-3' (Sigma). The PCR product was then digested with restriction enzymes BamHI and XhoI (NEB), gel purified (Qiagen), and ligated (Roche) into a modified pET28a expression vector (gift from Prof. Sondermann), yielding a Ulp-1 protease-cleavable N-terminal SUMO fusion and hexahistidine-tagged protein.

2.2.2 Expression and purification of protein

The plasmid was transformed into BL21-CodonPlus competent *E. coli* (Stratagene). 12 liters of bacterial culture were grown at 37 °C in TB supplemented with 50 mg/l kanamycin to an A_{600} of approximately 0.7 and induced overnight with 0.5 mM IPTG (Melford) at 18°C. Harvested cells were resuspended in buffer A (50 mM PIPES pH 6.8, 2 mM $MgCl_2$, 250 mM NaCl, 20 mM imidazole, 1 mM EGTA) supplemented with 1 mM PMSF and 2.5 mg lysozyme, and subjected to one cycle of freeze-thaw and sonication, before 1 mM DNaseI and 10 mM $MgCl_2$ were added. Sonication was carried out using the Vibra-Cell VCX 750 sonicator (Sonics & Materials, Inc.) with a 13 mm probe, at 70 % amplitude and 8 x 8 secs pulses with an 8-secs pause in between each pulse.

Clear lysate was loaded onto a 1 ml HisTrapFF column (GE Healthcare) equilibrated in buffer A. The resin was washed with buffer A containing 50 mM imidazole and the proteins were eluted on a gradient of buffer A from 50 mM to 500 mM imidazole. Fractions containing protein of interest were pooled and the buffer was exchanged for protease buffer (50 mM PIPES pH 6.8 and 250 mM NaCl). 0.25 mg of Ulp-1 protease was added to the protein sample (~20 mg) and the reaction was incubated overnight at 4°C. Uncleaved protein and protease

were removed by NiNTA affinity chromatography. The cleaved protein was subjected to size exclusion chromatography on a Superdex200 column (GE Healthcare) equilibrated in gel filtration buffer (50 mM Tris pH 6.8, 50 mM KCl, 1 mM DTT, 1 mM EGTA, and 2 mM $MgCl_2$). Fractions containing the protein of interest were pooled and concentrated on an Amicon Ultra filtration device (Millipore), with size exclusion limit of 10 kDa, to a final concentration of approximately 20 mg/ml, frozen in liquid nitrogen, and stored at -80°C.

2.2.3 Analytical Ultracentrifugation (AUC)

AUC experiments and data analysis were carried out with the assistance of Dr. Olwyn Byron at the University of Glasgow. Prior to the experiments, the protein was dialysed in 50 mM PIPES pH 6.8, 150 mM NaCl and 1 mM tris(2-carboxyethyl)phosphine (TCEP) at 4°C overnight. Sedimentation velocity (SV) experiments were used to determine the sedimentation coefficient, while sedimentation equilibrium (SE) experiments were used to determine the oligomeric state. Both experiments were performed using a Beckman Coulter Optima XL-I ultracentrifuge, an 8-place An-50 Ti rotor and two-sector cells. Seven samples of different concentrations were used for the experiments: 20, 10, 2, 1, 0.5, 0.3 and 0.2 mg/ml.

For the SV experiments, 60 µl each of the 20 and 10 mg/ml samples were loaded into 3 mm centrepieces, while 360 µl each of the rest of the samples were loaded into 12 mm centrepieces. The dialysis buffer was loaded into the second-sector of each cell to be used as a reference. The experiment was carried out at 49000 rpm and 4°C, using both interference and absorbance optics, and scans were recorded every 5 mins with a step size of 0.001 cm. SEDNTERP[158] was used to calculate the partial specific volume (v-bar) of the protein. The buffer density (ρ) and viscosity (η) were calculated and provided by Christine Ebel from Institut de Biologie Structurale, France.

SEDFIT[159] was used to analyse the sedimentation profile and the data was fitted to a continuous c(s) distribution model. Subtraction of all systematic noise from the raw data was carried out only for data obtained from the interference

optics. The apparent sedimentation coefficient ($s_{4,b}$), obtained from the fitting of the data to the non-interacting discrete species model, was converted to the true sedimentation coefficient ($s_{20,w}$) using equation 2. $s_{20,w}$ was then plotted against protein concentration to obtain the sedimentation coefficient at zero concentration ($s^{\circ}_{20,w}$) for a given protein species.

$$s_{20,w} = \frac{(1 - \bar{v}\rho)_{20,w}}{(1 - \bar{v}\rho)_{4,b}} \times \frac{\eta_{4,b}}{\eta_{20,w}} \times s_{4,b} \qquad \text{Equation 2}$$

where 20,w = at 20°C in water; and 4,b = at 4°C in buffer.

For the SE experiments, 15 µl each of the 20 and 10 mg/ml samples were loaded into 3 mm centrepieces, while 80 µl each of the rest of the samples were loaded into 12 mm centrepieces. The second-sector of each cell contained the reference, which is the dialysis buffer. The SE experiments were carried out at 20000 and 30000 rpm at 4°C, using the interference optics. Scans were recorded every 3 hrs until equilibrium was reached. SEDPHAT[160] was used to analyse the data obtained at equilibrium. The apparent weight average molecular weight was obtained by fitting the data to the species analysis model individually and globally.

2.2.4 Circular Dichroism (CD)

Prior to the experiments, the protein was dialysed in 20 mM potassium dihydrogen phosphate (buffered at pH 7.0) and diluted to 1 mg/ml, as the original buffer absorbed strongly below 205 nm. Subsequent CD experiments and data analysis were carried out by Dr. Sharon Kelly at the Protein Characterisation Facility of the University of Glasgow. The CD spectra was recorded on a JASCO J-810 spectropolarimeter, at 25°C, in the near UV range (320 – 250 nm) using a 0.5 cm pathlength cell containing 1 mg/ml of protein. For the far UV range (260 – 180 nm), the CD spectra was recorded using a 0.02 cm pathlength cell containing 0.33 mg/ml of protein. The data obtained was

submitted to DichroWeb[161], an online server, for secondary structure analysis using the CONTINLL algorithm[162].

2.2.5 Small Angle X-ray Scattering (SAXS)

Prior to the experiments, the protein was dialysed in 50 mM PIPES pH 6.8, 150 mM NaCl and 1 mM TCEP. Six samples of different concentrations were used for the experiments: 19.97, 9.86, 2.14, 0.98, 0.49, 0.29 mg/ml. The accurate concentrations were determined using UV spectrophotometry at 280 nm. Data was collected by Dr. Olwyn Byron on the beamline X33 at Deutsches Elektronen-Synchrotron (DESY), European Molecular Biology Laboratory (EMBL). Background scattering was collected from the dialysis buffer and subtracted from the scattering profiles of the protein samples. All data were integrated, scaled and corrected for beam decay using PRIMUS[163].

With the given data, I then proceeded with data analysis. The radius of gyration (R_g) and the extrapolated intensity at zero scattering angle (I(0)) were determined by Guinier approximation[164]. Next, GNOM[165] was used to obtain the p(r) or pair-distance distribution function plot and to determine the maximum dimension (D_{max}) of the protein. More accurate values of R_g and I(0) were also obtained from the p(r) function. Then, using the p(r) plot as the fitting target, *ab initio* modelling of the molecular envelope was performed using GASBOR22[166] in reciprocal space. As the protein was found to exist as a dimer from AUC, the P2 symmetry was used during modelling. 20 independent simulations, consisting of 100 cycles of simulated annealing each, were carried out in batch mode for each of the six data sets. The solutions for each data set were then superimposed, averaged and filtered using DAMAVER[167] to obtain a consensus structure. Figures were prepared using PyMOL[151].

2.3 *Drosophila melanogaster* conventional kinesin

2.3.1 Molecular cloning of recombinant plasmid

The motor domain of *D. melanogaster* kinesin (residues 1-381) was initially cloned into the vector pET21[168]. PCR was carried out to amplify residues 1-365 and residues 1-375, and to include restriction sites BamHI and XhoI. HotStar HiFidelity DNA Polymerase was used according to the manufacturer's protocol (Qiagen). The forward primer used was 5' CAT ATG GGA TCC GCG GAA CGA GAG ATT CC-3' for both reactions, while the reverse primer used was 5'-CGT AGA CTC GAG TTA CTT ACC CTT TAG TCG GGC GTT CTT TTC C-3' for residues 1-365 and 5' CGT AGA CTC GAG TTA GCG CGC AAG CTC GAT CTC for residues 1-375 (Sigma). The PCR products were then digested with restriction enzymes BamHI and XhoI (NEB), gel purified (Qiagen), and ligated (Roche) into modified pET28a expression vector (Invitrogen) separately, yielding Ulp-1 protease-cleavable N-terminal SUMO fusion and hexahistidine-tagged proteins.

2.3.2 Expression and purification of protein

The plasmid containing residues 1-365 was transformed into BL21-CodonPlus competent *E. coli* (Stratagene). 12 liters of bacterial culture were grown at 37°C in TB supplemented with 50 mg/l kanamycin to an A_{600} of approximately 0.7 and induced overnight with 0.5 mM IPTG at 18°C. Harvested cells were resuspended in buffer A (20 mM Tris pH 8.8, 1 mM $MgCl_2$, 200 mM NaCl, 20 mM imidazole, 1 mM EGTA) supplemented with 1 mM PMSF, 1 mM MgATP, and 2.5 mg lysozyme, and subjected to one cycle of freeze-thaw and sonication, before 1 mM DNaseI and 10 mM $MgCl_2$ were added. Sonication was carried out using the Vibra-Cell VCX 750 sonicator (Sonics & Materials, Inc.) with a 13 mm probe, at 70 % amplitude and 8 x 8 secs pulses with an 8-secs pause in between each pulse.

Clear lysate was loaded onto a 1 ml HisTrapFF column (GE Healthcare) equilibrated in buffer A. The resin was washed with buffer A containing 50 mM Imidazole and the proteins were eluted on a gradient of buffer A from 50 mM to 500 mM Imidazole. Fractions containing protein of interest were pooled and the

buffer was exchanged for protease buffer (20 mM Tris pH 8.8 and 250 mM NaCl). 0.25 mg of Ulp-1 protease, 1 mM MgATP, and 2 mM $MgCl_2$ were added to the protein sample (~20 mg) and the reaction was incubated overnight at 4°C. Uncleaved protein and protease were removed by NiNTA affinity chromatography. The cleaved protein was subjected to size exclusion chromatography on a Superdex200 column (GE Healthcare) equilibrated in gel filtration buffer (20 mM Tris pH 8.8, 300 mM NaCl, 1 mM DTT, 1 mM EGTA, and 2 mM $MgCl_2$). Fractions containing the protein of interest were pooled and concentrated on an Amicon Ultra filtration device (Millipore), with size exclusion limit of 30 kDa, to a final concentration of approximately 20 mg/ml, frozen in liquid nitrogen, and stored at -80°C.

2.3.3 Crystallisation of dimer and dimer-tail complex

Crystals of the motor domain dimer (residues 1-365) appeared after 2 days in hanging drops by mixing 1 µl of protein with 1 µl of reservoir solution containing 24 % PEG-3350, 0.15 M ammonium sulphate, and 0.1 M HEPES sodium pH 7.8 in VDX plates at 19°C. Micro streak seeding was carried out to produce single and larger crystals. A block-shaped crystal with dimensions of approximately 0.1 x 0.1 x 0.1 mm was immersed in cryoprotectant solution (28.8 % PEG-3350, 0.18 M ammonium sulphate, 0.12 M HEPES sodium pH 7.8, 0.36 M NaCl, and 20 % erythritol) and flash frozen in liquid nitrogen.

Initially, I crystallised the motor domain dimer (residues 1-365) in complex with $tail_{910-952}$ peptide. However, the crystals diffracted no better than 2.7 Å. I was able to solve the structure and saw electron density for only ten residues of the peptide. Hence, we decided to use a shorter tail peptide for crystallisation. Purified motor domain (10 mg/ml) was incubated with $tail_{937-952}$ peptide (6.1 mg/ml) in a ratio of (1 monomeric motor : 2 tails) for 2 hrs on ice before setting up the crystal trays. The tail peptides were expressed and purified by our collaborator Prof. David Hackney (Carnegie Mellon University). Crystals of the motor domain dimer-tail complex appeared after 2 days in hanging drops by mixing 1 µl of protein complex with 1 µl of reservoir solution containing 18 % PEG-3350, 0.2 M KCl, and 0.1 M HEPES sodium pH 7.4 in VDX plates at 19°C.

Micro streak seeding was carried out to produce single larger crystals. A block-shaped crystal with dimensions of approximately 0.3 x 0.1 x 0.1 mm was immersed in cryoprotectant solution (21.6 % PEG-3350, 0.24 M KCl, 0.12 M HEPES sodium pH 7.4, 0.36 M NaCl, and 20 % PEG-200) and flash frozen in liquid nitrogen.

2.3.4 Data collection and processing

Diffraction data for the dimer and dimer-tail complex were recorded at the ESRF ID23-2 and Swiss Light Source PXI, with the assistance of Dr. David Flot and Dr. Marcus Muller respectively. Data were processed using iMosflm[140] and scaled using Scala[141] from the CCP4 suite of programs[142]. The calculation of R_{free} used 5 % of data.

2.3.5 Structure determination and refinement

The dimer and dimer-tail structures were solved by molecular replacement (Phaser[155]) using one molecule of human kinesin-1 motor domain (PDB code: 1BG2)[17] and one molecule of the refined dimer structure as search models respectively. Refinement was carried out with Refmac5[147]. Electron-density and difference density maps all σ_A-weighted, were inspected and the model was improved using Coot[148]. Model geometry was analysed using Molprobity[157]. For the dimer structure, 90.31 % (587) of the residues are in the preferred regions, 6.77 % (44) are in the allowed regions, and 2.92 % (19) are outliers as shown by the Ramachandran Plot. For the dimer-tail complex, 94.14 % (1270) of the residues are in the preferred regions, 4.97 % (67) are in the allowed regions, and 0.89 % (12) are outliers. Protein domain interfaces were analyzed using PDBePISA[169]. Figures were prepared using PyMOL[151].

2.3.6 Alanine scan peptide array

16-residue tail peptides, corresponding to a single, double, or triple alanine-scan, were synthesised and bound to the membrane by the Peptide Synthesis

Laboratory at the London Research Institute. Each residue was mutated to an alanine in turn, while an alanine was mutated to a glycine. Two identical membranes were synthesised and the experiment was repeated twice, once on each membrane, to validate the results. The membranes were soaked in 100 % ethanol for 15 secs, washed with TBS-T for 3 x 5 mins and blocked with 5 % milk in TBS-T for 1 hr at rtp. As a control for non-specific binding of the antibody, the membrane was incubated with 1:8000 dilution of HRP-conjugated anti-His_6 antibody (Clontech) for 1 hour (rtp) and developed like a western blot. Next, the membrane was washed with TBS-T as above, before incubating with 8 µg/ml of His_6-tagged motor domain dimer (residues 1-375) overnight at 4°C. The protein was expressed and purified as above (section 1.3.2), but the His_6 tag was not cleaved and the protein sample was not passed through a second Ni-NTA column. The membrane was then probed with antibody and developed as above.

3 Developing inhibitors of human mitotic kinesin Eg5

The results in this chapter have been published in peer-reviewed journals:

Kaan, H.Y., Ulaganathan, V., Hackney, D.D. & Kozielski, F. An allosteric transition trapped in an intermediate state of a new kinesin-inhibitor complex. *Biochem J* **425**, 55-60 (2010). (Appendix 1)

Kaan, H.Y., Ulaganathanm, V., Rath, O., Prokopcová, H., Dallinger, D., Kappe, C.O. & Kozielski, F. Structural basis for inhibition of Eg5 by dihydropyrimidines: stereoselectivity of antimitotic inhibitors enastron, dimethylenastron and fluorastrol. *J Med Chem* **53**, 5676-83 (2010). (Appendix 2)

Kaan, H.Y., Weiss, J., Menger, D., Ulaganathan, V., Tkocz, K., Laggner, C., Popowycz, F., Joseph, B. & Kozielski, F. Structure-activity relationship and multidrug resistance study of new S-trityl-L-cysteine derivatives as inhibitors of Eg5. *J Med Chem* **54**, 1576-86 (2011). (Appendix 3)

3.1 Aims and objectives

Human mitotic kinesin Eg5 is an interesting target for drug development in cancer chemotherapy, because its inhibition causes cells to arrest in mitosis and eventually die by apoptosis. Monastrol was the first specific inhibitor of Eg5 to be discovered. Our lab later identified *S*-trityl-L-cysteine (STLC) as a potent and specific inhibitor against Eg5. Employing a structure-based drug design method, we hope to develop more potent and efficient inhibitors that may be used as alternatives or in complement with taxanes and vinca alkaloids. These drugs are used successfully in clinics against cancers, but they have the tendency to cause neurotoxicities and develop resistance in patients. As Eg5 inhibitors do not target microtubules but act via a different mode of action, we believe that they are potential alternatives that are worth pursuing.

In this chapter, I will report the crystal structures of Eg5 in complex with three monastrol analogues (enastron, dimethylenastron and fluorastrol), STLC, and four STLC analogues (compounds **6**-**9**) separately (Figure 3-1). Based on the structures, I will discuss the structure-activity relationship (SAR) of each class of inhibitors. In addition, I will analyse the intermediate state of the Eg5-STLC structure to discuss the pathway of structural changes that occur upon inhibitor binding. Lastly, thermodynamic parameters of interaction between Eg5 and its inhibitors, determined by isothermal titration calorimetry (ITC), will be presented to help us gain a better understanding of the molecular mechanism of inhibition by an Eg5 inhibitor.

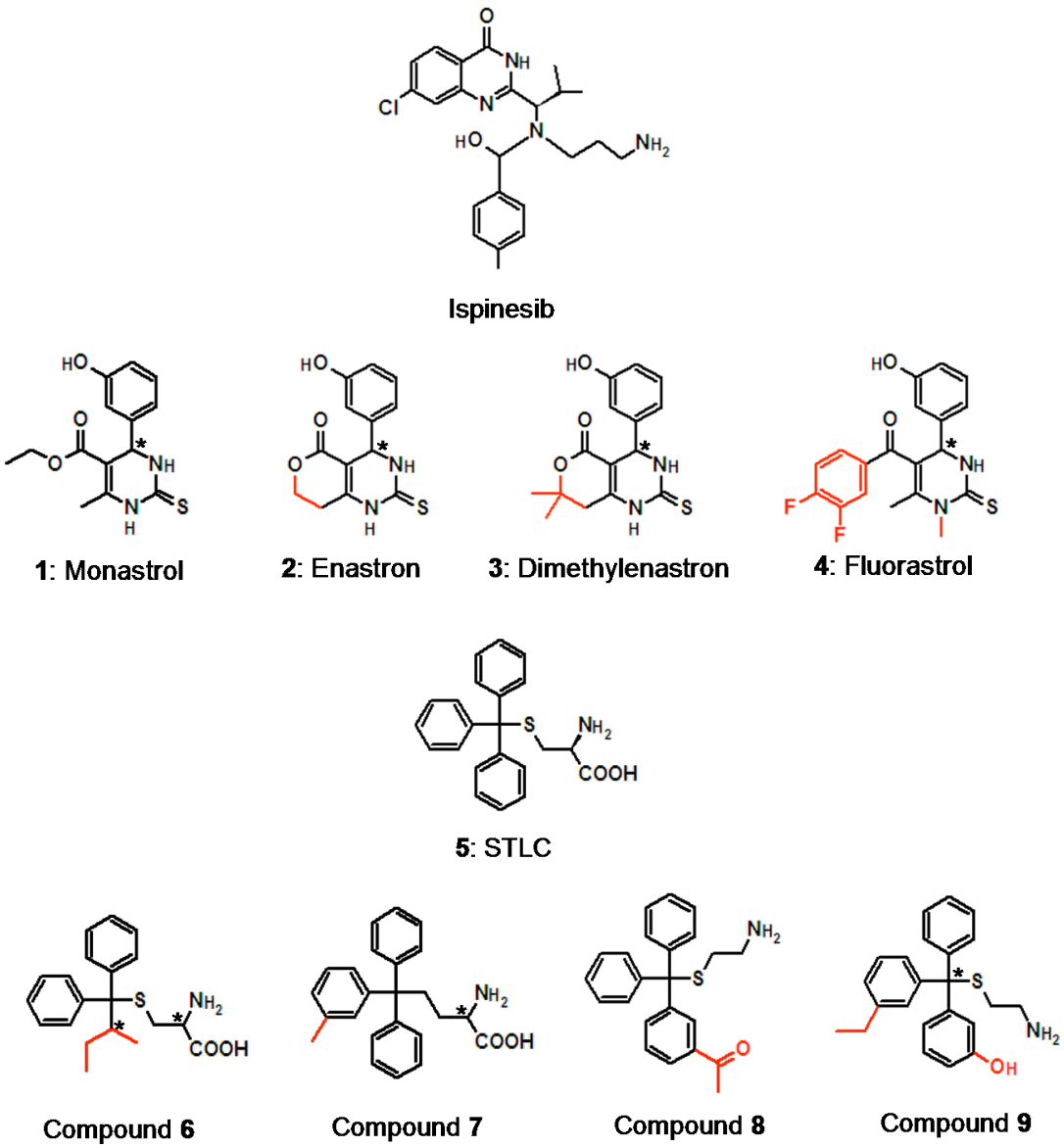

Figure 3-1. Chemical structures of Eg5 inhibitors.

Differences between monastrol and its analogues, and STLC and its analogues are shown in red. Asterisks mark chiral centers.

3.2 Results

3.2.1 Structures of Eg5 in complex with enastron, dimethylenastron and fluorastrol

We solved the crystal structures of human Eg5 in complex with enastron, dimethylenastron and fluorastrol. Each Eg5-inhibitor structure was solved in space group $P2_12_12_1$. Statistics for data collection and refinement are summarised in Table 3-1. All structures contain two molecules per asymmetric unit and are missing the first 15 residues at the N-terminus. Loop L11 is also absent as in most other kinesin structures, as it is flexible. All three structures have one molecule of Mg^{2+}ADP bound in the nucleotide-binding pocket with the magnesium coordinated octahedrically with the β-phosphate, the oxygen (OG1) of the hydroxyl side chain of Thr112 and four water molecules. The three inhibitors bind to Eg5 at the well-characterised inhibitor-binding pocket, bordered by helix α2, loop L5 and helix α3. Based on the chemical structure, the three distinct inhibitors share a common 3-hydroxyphenyl group, which occupies the same position in all the crystal structures and makes virtually identical interactions with the residues in the inhibitor-binding pocket.

Eg5 was crystallised in the presence of racemic enastron; yet, the structure revealed full occupancy of the inhibitor in the *S*-configuration and there is no evidence for binding in the *R*-configuration (Figure 3-2). The 3-hydroxyl group on the phenyl ring makes hydrogen bonds with the main chain carbonyl group of Glu118, the main chain amino group of Ala133 and the side chain nitrogen (NE) of Arg119. Moreover, the phenyl ring forms C—H---π interaction with the pyrrolidine ring of Pro137 and edge-to-face (T-shape) interactions with the phenyl rings of Trp127 and Tyr211. Next to the phenol group is the dihydropyrimidine ring. Here, the 2-thioxo group points towards the core of the protein and interacts with one water molecule. In addition, the nitrogen at position 1 (NAK) acts as a hydrogen donor and forms hydrogen bonds with two water molecules. Adjacent to the dihyropyrimidine ring is the oxo-cyclohexene ring system. The oxygen acts as a hydrogen bond acceptor and forms a hydrogen bond with the main chain amino group of Arg119 and with a structural water molecule.

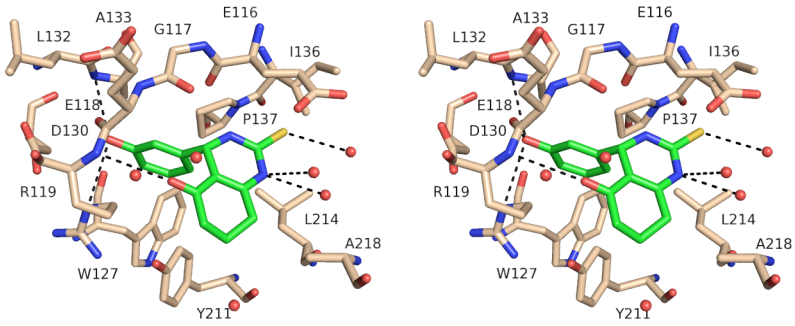

Figure 3-2. Stereoplot of enastron in the inhibitor-binding pocket.

Hydrogen bonds between inhibitor (green) and Eg5 residues (beige) or structural water molecules (red spheres) are depicted by black broken lines.

The racemic mixture of dimethylenastron was used for crystallisation with Eg5. However, the structure indicates a preference of Eg5 for the *S*-enantiomer, instead of the *R*-enantiomer. The overall conformation of dimethylenastron in the inhibitor-binding pocket (Figure 3-3) and the interactions with the residues of the allosteric binding site is virtually identical to that observed with enastron. The only difference between the Eg5-enastron and Eg5-dimethylenastron complexes is the additional dimethyl group on the oxo-cyclohexene ring system, which points towards the solvent region, but maintains hydrophobic interactions (≤ 3.9 Å) with the hydrophobic main chain of Ala218 that constitutes part of helix α3. In addition, one of the methyl groups (CAA) forms a C—H---π interaction with Tyr211.

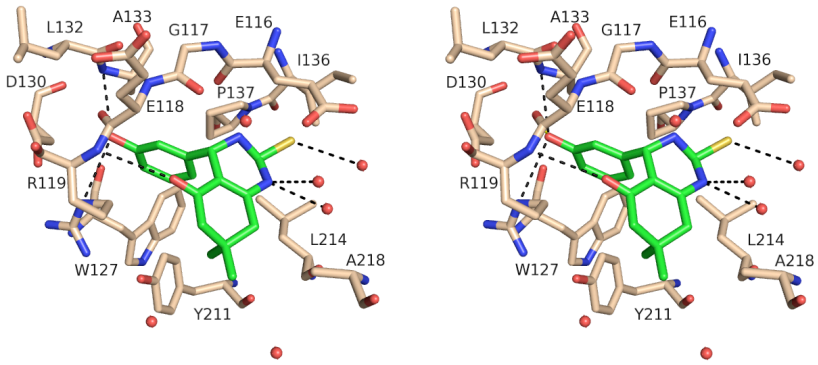

Figure 3-3. Stereoplot of dimethylenastron in the inhibitor-binding pocket.

Hydrogen bonds between inhibitor (green) and Eg5 residues (beige) or structural water molecules (red spheres) are depicted by black broken lines.

Eg5 was crystallised with the racemic mixture of fluorastrol and the structure revealed preferential binding of Eg5 to the *R* configuration, unlike enastron, and dimethylenastron, which bind in the *S* configuration. Consequently, the interactions in the inhibitor-binding pocket, apart from that of the 3-hydroxyphenyl group which is common in all three inhibitors, are strikingly different from that of enastron and dimethylenastron. In the *R* configuration, the 2-thioxo group points to the solvent-exposed region of the protein and interacts with two water molecules (Figure 3-4). The N1-H on the dihydropyrimidine ring interacts with a water molecule and the N3-H group interacts via a hydrogen bond with the main chain carbonyl group of Gly117. The 3',4'-difluorophenyl group, on the other hand, points towards the core of the protein. One of the fluorines (FAF) forms multipolar interactions[170] with the guanidinium side chain of Arg221, the main chain amide of Ala218 and the main chain carbonyl group of Gly217. In this configuration, the other fluorine (FAG), which points towards the edge of the phenyl ring of Phe239 and the carbonyl group (OAC) of the inhibitor do not form any hydrogen bonds with the rest of the protein.

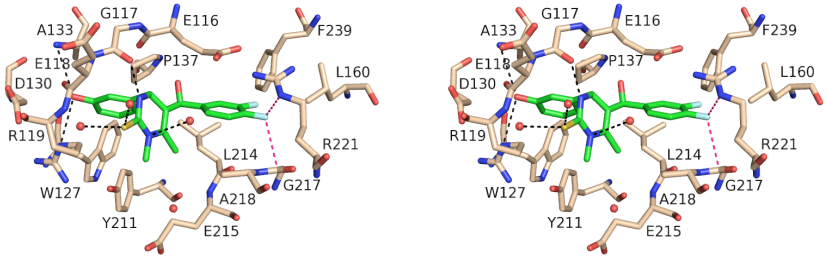

Figure 3-4. Stereoplot of fluorastrol in the inhibitor-binding pocket.

Hydrogen bonds between inhibitor (green) and Eg5 residues (beige) or structural water molecules (red spheres) are depicted by black broken lines. Multipolar interactions between the inhibitor and Eg5 residues are depicted by pink broken lines.

Table 3-1. Data collection and refinement statistics of Eg5 in complex with monastrol analogues.

	Enastron [a]	Dimethylenastron [a]	Fluorastrol [a]
Unit cell dimensions a, b, c, β (Å, °)	69.6, 79.8, 159.3, 90.0	69.5, 79.7, 159.3, 90.0	69.6, 79.8, 160.0, 90.0
Space group	$P2_12_12_1$	$P2_12_12_1$	$P2_12_12_1$
Beamline / Detector	ID23-1 / Q315R	ID23-1 / Q315R	ID14-1 / Q210
Molecules per asymmetric unit	2	2	2
Resolution range (Å)	30 - 1.9	30 - 2.30	30 - 2.40
No. of reflections	347186	314811	257554
No. of unique reflections	69235	40030	35497
Completeness (%)	98.2 (94.6) [b]	99.9 (99.4)	95.5 (93.4)
Multiplicity	5.0	7.9	7.3
R_{sym} (%)	11.8 (34.4)	10.3 (38.6)	9.6 (33.2)
I/σ(I)	10.0 (4.9)	16.0 (5.5)	10.8 (5.0)
Wilson B ($Å^2$)	14.57	28.48	33.70
Refinement statistics			
R_{work} / R_{free} (%)	16.31 / 23.16	17.59 / 24.05	19.58 / 27.32
Average B Factors			
Overall	19.49	21.42	23.41
Main chain / Side chain	16.58 / 21.72	19.58 / 22.93	21.97 / 24.67
No. of Mg^{2+}ADP / Inhibitor / Water	2 / 2 / 822	2 / 2 / 541	2 / 2 / 433
r.m.s.d. [c] in bond length (Å)	0.0126	0.0135	0.0133
r.m.s.d. in bond angle (°)	1.502	1.649	1.819

[a] The racemic mixture was used for crystallisation of the protein-inhibitor complex.

[b] Values in parentheses pertain to the highest resolution shell.

[c] r.m.s.d. is the root-mean-square deviation from ideal geometry.

3.2.2 Structures of Eg5 in complex with STLC and compound 6

The crystal structures of the Eg5-STLC and Eg5-**6** complexes were solved at a resolution of 2.0 and 2.2 Å respectively. Data collection and refinement statistics are shown in Table 3-2. Both complexes crystallised in the space group $P3_2$ with three molecules in the asymmetric unit. Loop L11 is flexible and missing as in most other kinesin structures. Mg^{2+}ADP is bound in all the nucleotide-binding pockets with the magnesium octahedrically coordinated. STLC and compound **6**, which have well-defined electron density, occupy the inhibitor-binding pocket similar to that of monastrol and its analogues. Although we used the diastereoisomeric mixture of **6** for crystallisation of the Eg5-inhibitor complex, we fitted only one of the diastereoisomers, *S*-(2-methyl-1,1-diphenylbutyl)-L-cysteine, into the structure.

The conformation of STLC and the interactions between STLC and Eg5 are virtually identical in all three molecules. The three phenyl rings in STLC, which represent the hydrophobic part of the inhibitor, are buried in the allosteric site and display several hydrophobic interactions with the alkyl side chains of Glu215, Glu116 and Arg119 (Figure 3-5). We also observed edge-to-face (T-shape) interaction between the first phenyl group of STLC and the phenyl ring of Trp127; C—H---π interaction between the first phenyl group of STLC and the pyrrolidine ring of Pro137; offset stacked π-π interaction between the second phenyl group and Tyr211; and C—H---π interaction between the third phenyl group and the side chain of Leu214[171].

On the other hand, the hydrophilic part of the inhibitor, namely the cysteine moiety, is exposed to the solvent and we observe several hydrogen bond interactions: the amino group of the cysteine moiety with the main chain carbonyl oxygen of Gly117, the side chain oxygen (OE1) of Glu116, and a structural water molecule; an oxygen (OXT) of the carboxyl group of the cysteine moiety with one of the side chain amino groups (NH1) of Arg221 and four structural water molecules; and the other oxygen of the carboxyl group with one structural water molecule. All structural water molecules mentioned are conserved in all three molecules of the asymmetric unit.

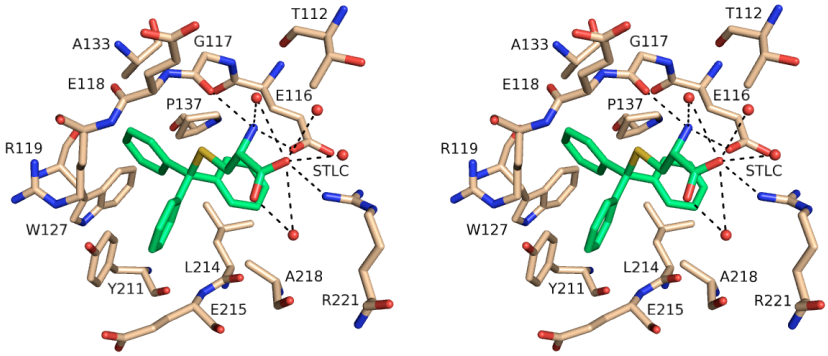

Figure 3-5. Stereoplot of STLC in the inhibitor-binding pocket.

Hydrogen bonds between inhibitor (green) and Eg5 residues (beige) or structural water molecules (red spheres) are depicted by black broken lines.

Upon analysing the inhibitor-binding pocket, we observe identical hydrogen bond interactions between Eg5 and the cysteine moieties of STLC and **6** (Figure 3-6). In addition, **6** appears to form one more hydrogen bond with water, as compared to STLC. This hydrogen bond — formed between an oxygen (OXT) of the carboxyl group of the cysteine moiety and a structural water molecule — is only observed in molecule A and B of the Eg5-**6** structure. With a high resolution structure and well-defined electron density map, we were able to determine undoubtedly the location of the alkyl chain substituent of **6**. The alkyl chain points toward the solvent-exposed region of the protein and the methyl group (CAA) forms a C—H---π interaction with the phenyl ring of Tyr211.

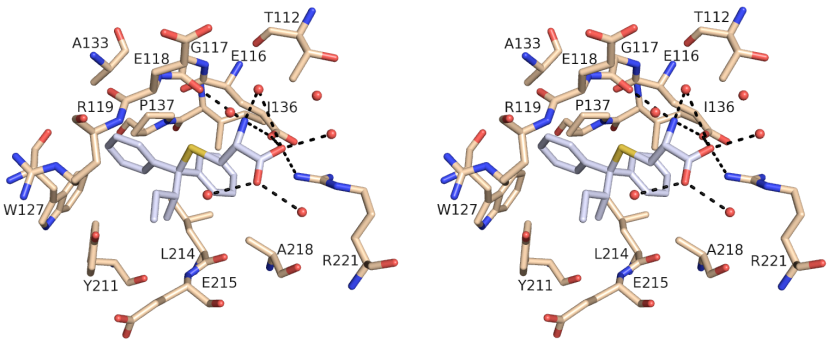

Figure 3-6. Stereoplot of compound 6 in the inhibitor-binding pocket.

Hydrogen bonds between inhibitor (grey) and Eg5 residues (beige) or structural water molecules (red spheres) are depicted by black broken lines.

Table 3-2. Data collection and refinement statistics of Eg5 in complex with STLC and compound 6.

	STLC [a]	Compound 6 [a]
Unit cell dimensions a, b, c, β (Å, °)	96.5, 96.5, 124.4, 120.0	96.4, 96.4, 124.4, 120.0
Space group	$P3_2$	$P3_2$
Beamline / Detector	ID23-1 / Q315R	ID29 / Q315R
Molecules per asymmetric unit	3	3
Resolution range (Å)	30 - 2.0	30.0 - 2.2
No. of unique reflections	87598	65550
Completeness (%)	99.9 (100.0) [b]	99.9 (100.0)
Multiplicity	5.8	6.3
R_{sym} (%)	8.9 (40.0)	8.6 (28.7)
I/σ(I)	12.8 (4.0)	14.3 (6.0)
Wilson B ($Å^2$)	27.2	33.4
Refinement statistics		
R_{work} / R_{free} (%)	15.9 / 21.8	17.4 / 22.4
Average B Factors		
Overall	35.9	34.9
Main chain / Side chain	33.6 / 37.7	33.1 / 36.3
No. of Mg^{2+}ADP / Inhibitor / Water	3 / 3 / 1192	3 / 3 / 783
r.m.s.d. [c] in bond length (Å)	0.0127	0.0130
r.m.s.d. in bond angle (°)	1.61	1.678

[a] The racemic mixture was used for crystallisation of the protein-inhibitor complex.

[b] Values in parentheses pertain to the highest resolution shell.

[c] r.m.s.d. is the root-mean-square deviation from ideal geometry.

3.2.3 Structures of Eg5 in complex with compounds 7, 8 and 9

The crystal structures of Eg5 in complex with **7**, **8** and **9** were solved to resolutions of 2.75, 2.75 and 2.65 Å respectively. Data collection and refinement statistics are presented in Table 3-3. Eg5-**7** and Eg5-**9** complexes crystallised in space group $I2_13$ with 1 molecule per asymmetric unit, while Eg5-**8** complex crystallised in space group $P2_12_12_1$ with 7 molecules per asymmetric unit. A closer look at the inhibitor binding pocket reveals that the three phenyl rings of **7**, **8** and **9** are buried in the same pockets as that of STLC. Consequently, the same hydrophobic and aromatic interactions between the three phenyl rings and the residues in the inhibitor-binding pocket were observed.

As the racemic mixture of **7** was used to crystallise the Eg5-inhibitor complex, electron density for both enantiomers were observed in the structure. Several hydrogen bond interactions between Eg5 and the cysteine moiety of (*S*)-**7** were apparent: the amino group with the main chain carbonyl oxygen of Gly117 and the side chain oxygen (OE1) of Glu116; and an oxygen (OXT) of the carboxylic group of the cysteine moiety with one of the side chain amino groups (NH1) of Arg221 (Figure 3-7). However, these interactions were not observed for the *R*-enantiomer. Instead, the amino group of the cysteine moiety forms a hydrogen bond with a structural water molecule.

Although the sulphur in STLC has been substituted by a carbon in **7**, the interactions between Eg5 and both inhibitors are virtually identical. The only difference lies in the length of the shorter C-C-C bonds (3.9 Å), as compared to the length of the longer C-S-C bonds (4.5 Å). With a well-defined electron density map, the position of the phenyl ring with the *meta*-substituted methyl group was determined unambiguously. It sits in the mainly hydrophobic pocket, formed by Ile136, Pro137, Leu160, Leu214 and Phe239. Consequently, the small lipophilic methyl substituent on the phenyl ring forms hydrophobic interactions with these Eg5 residues.

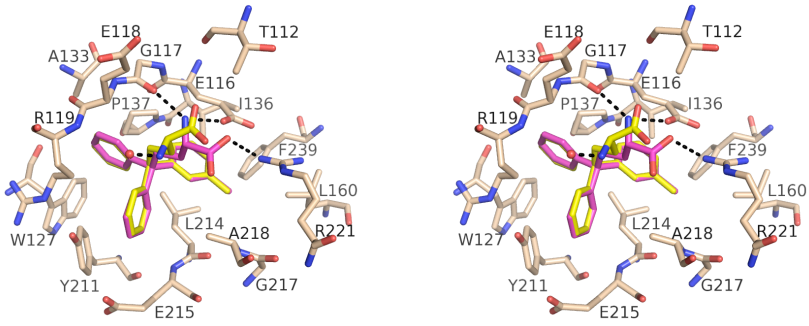

Figure 3-7. Stereoplot of compound 7 in the inhibitor-binding pocket.

Hydrogen bonds between inhibitor (magenta: *S*-enatiomer; yellow: *R*-enantiomer) and Eg5 residues (beige) or structural water molecules (red spheres) are depicted by black broken lines.

In the structure of Eg5 in complex with **8**, where the carboxylic acid in the amine tail is absent, hydrogen bond interactions were observed only between the amino group and the main chain carbonyl oxygen of Gly117 and the side chain oxygen (OE1) of Glu116 (Figure 3-8). The loss of the carboxylate group not only removes a hydrogen bond interaction, but also reduces restraints on the amine tail and increases its conformational freedom, as evident from one molecule (chain D) where the amino group points away from the side chain of Glu116 and towards the amino group of Arg221 instead. Based on the electron density map, the phenyl ring carrying the *meta*-substituted acetate group is positioned in the same pocket as the *meta*-substituted phenyl ring of **7**. The methyl of the acetate group forms hydrophobic interactions with Phe239, Leu160, Ile136 and Leu214, similar to the methyl substituent of **7**. The carbonyl oxygen of the acetate group of **8** forms a hydrogen bond with one of the side chain amino groups (NH1) of Arg221.

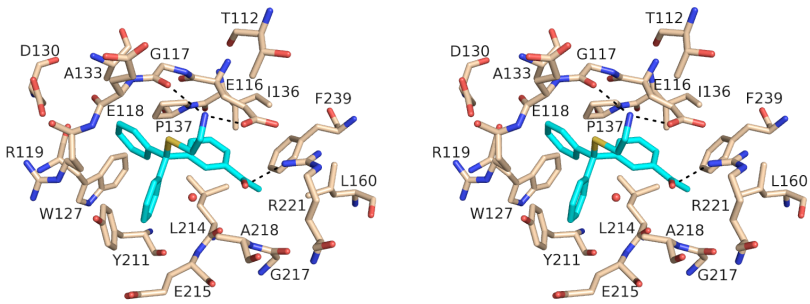

Figure 3-8. Stereoplot of compound 8 in the inhibitor-binding pocket.

Hydrogen bonds between inhibitor (blue) and Eg5 residues (beige) or structural water molecules (red spheres) are depicted by black broken lines.

Compound **9** is similar to **8** in that it lacks the carboxylic acid in the amine tail. Correspondingly, the amine tail of compound **9** adopts the same conformation as that of **8**. In the crystal structure, the amino group of **9** points towards the side chain oxygen of Glu 116 and forms similar hydrogen bond interactions as **8** (Figure 3-9). As there is only one molecule in the asymmetric unit, flexibility of the amine tail lacking the carboxylic acid was not observed. Despite the similar amine tail, compound **9** consists of a chiral carbon while **8** does not. Although the racemic mixture of compound **9** was used for crystallisation, only the *R*-enantiomer was found to bind in the inhibitor-binding pocket.

According to the well-defined electron density map, the phenyl ring carrying the *meta*-substituted ethyl group sits in the same pocket as the *meta*-substituted phenyl rings of **7** and **8**. Hence, similar hydrophobic interactions form between the ethyl group and the residues of the hydrophobic pocket, such as Ile136, Leu160 and Leu214**.** Compound **9** also consists of a second phenyl ring that has a *meta*-substituted hydroxyl group. It is shown to fit in a pocket formed by Ala133, Leu132, Asp130, Trp127, Arg119, Glu118 and Pro137. In this position, the hydroxyl substituent points towards the core of the protein instead of outwards towards the solvent. The hydroxyl group also forms a hydrogen bond with the main chain nitrogen of Ala133.

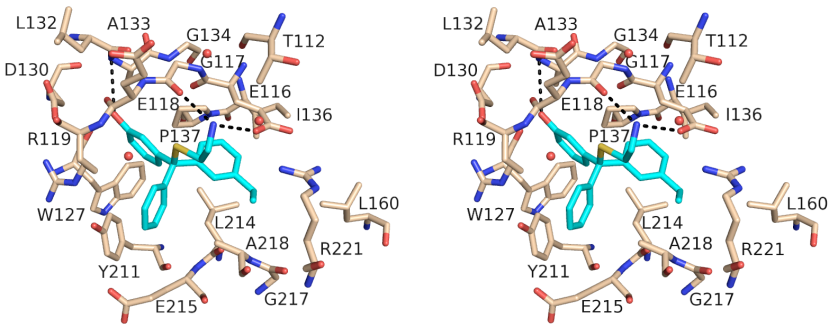

Figure 3-9. Stereoplot of compound 9 in the inhibitor-binding pocket.

Hydrogen bonds between inhibitor (blue) and Eg5 residues (beige) or structural water molecules (red spheres) are depicted by black broken lines.

Table 3-3. Data collection and refinement statistics of Eg5 in complex with compounds 7, 8 and 9.

	Compound 7 [a]	Compound 8	Compound 9 [a]
Unit cell dimensions a, b, c, γ (Å, °)	158.6, 158.6, 158.6, 90.0	145.7, 156.2, 170.0, 90.0	158.3, 158.3, 158.3, 90.0
Space group	$I2_13$	$P2_12_12_1$	$I2_13$
Beamline / Detector	I23-2 / MAR 225	ID23-1 / Q315R	I23-2 / MAR 225
Molecules per asymmetric unit	1	7	1
Resolution range (Å)	30 - 2.75	30.0 - 2.75	30 – 2.65
No. of unique reflections	17322 (2496) [b]	98930 (14132)	19305 (2826)
Completeness (%)	99.8 (99.8)	97.7 (96.6)	99.9 (100.0)
Multiplicity	5.8 (5.4)	5.4 (5.5)	7.5 (7.6)
R_{sym} (%)	8.3 (60.9)	9.4 (57.7)	8.7 (58.5)
I/σ(I)	12.2 (3.2)	13.0 (2.7)	15.4 (3.9)
Wilson B ($Å^2$)	77.98	70.75	66.89
Refinement statistics			
R_{work} / R_{free} (%)	19.76 / 24.30	22.06 / 28.04	18.53 / 22.76
Average B Factors			
Overall	66.54	64.67	60.50
Main Chain / Side Chain	65.34 / 67.72	63.94 / 65.39	58.93 / 61.95
No. of Mg^{2+}ADP / Inhibitor / Water	1 / 1 / 41	7 / 7 / 302	1 /1 / 110
r.m.s.d. [c] in bond length (Å)	0.012	0.013	0.012
r.m.s.d. in bond angle (Å)	1.75	1.70	1.68

[a] The racemic mixture was used for crystallisation of the protein-inhibitor complex.

[b] Values in parentheses pertain to the highest resolution shell.

[c] r.m.s.d. is the root-mean-square deviation from ideal geometry.

3.2.4 Structure of the intermediate state of inhibitor-bound Eg5

To study the intermediate state of inhibitor-bound Eg5, we examine the structure of the Eg5-STLC complex, which crystallises with 3 molecules per asymmetric unit. The three molecules reveal a variety of conformational changes throughout the molecule, when compared with the native structure of the Eg5 motor domain[58] in the absence of an inhibitor. The most obvious changes occur in the inhibitor-binding pocket. In all three molecules, Arg119 and Tyr211 move outwards, while Trp127 of the Loop L5 region (Gly117 to Ala133) swings downwards, by about 7 Å, from a solvent-exposed region in the native structure to form an aromatic edge-to-edge π-interaction with the phenol ring of Tyr211 in the inhibitor-bound structure (Figure 3-10).

In the native and STLC-bound structures, Mg^{2+}ADP occupies the active site through binding of the α- and β-phosphates to the P-loop. The overlay of molecules A, B and C with the native structure showed no differences in conformation of the P-loop. We then investigated helix α3. In all three molecules, the apex of the helix α3 is shifted towards the solvent by a maximum of about 2 Å at Glu209, when compared to the native structure (Figure 3-11). Following helix α3 is switch I, which adopts the same conformation in all three molecules, but differ from that of the native structure. Loop L9 is shifted towards the solvent by about 6 Å and displays an additional one-turn of a helix. The hydroxyl group of Tyr231, which is originally solvent-exposed in the native structure, moves by about 12 Å into the hydrophobic environment of the protein.

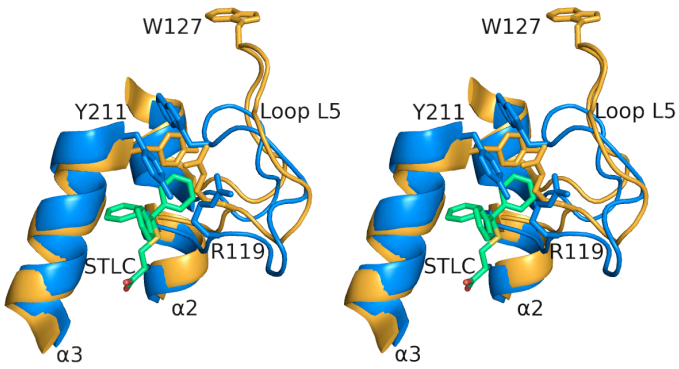

Figure 3-10. Stereoplot showing overlay of the inhibitor-binding pocket of native Eg5 and Eg5-STLC complex.

Yellow: native Eg5 (PDB ID: 1II6)[58]; blue: Eg5-STLC molecule B; and green: STLC.

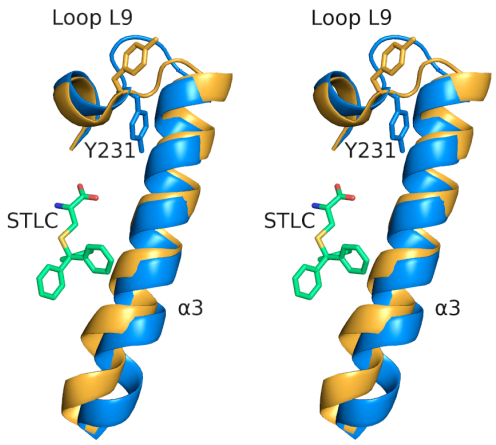

Figure 3-11. Stereoplot showing overlay of helix α3 of native Eg5 and Eg5-STLC complex. Yellow: native Eg5 (PDB ID: 1II6)[58]; blue: Eg5-STLC molecule B; and green: STLC.

Upon overlaying molecules A, B and C, using the main chain Cα atoms from residues 19 to 363, molecules A and B were found to be almost identical with a root mean square deviation of 0.33 Å. However, a larger deviation of 1.32 Å was observed when molecules A and B were overlaid with C. While the conformation of the inhibitor-binding pocket and structural motifs, such as the P-loop, helix α3 and switch I are virtually identical in all three molecules, the conformation of the switch II cluster (helix α4, loop L12 and helix α5) and neck linker differs greatly in molecule C.

Comparing molecule C with molecule B and the native structure, I observe a clear progression of the switch II cluster as it rotates about 15° from the native structure to the intermediate state of molecule C and eventually to the final state in molecule B (Figure 3-12). In fact, this progression can be seen as two distinct movements: first an anti-clockwise rotation of approximately 10° about the origin around residue Leu293, then a similar rotation of approximately 5° about an origin beyond the apex of helix α4. On the other hand, the neck linker appears to be in the same conformation in native Eg5 and in the intermediate state (molecule C). It is in an undocked position, perpendicular to the helix α6. The neck-linker eventually moves by about 32 Å to adopt a docked position, parallel to helix α6 in the final state in molecule B (Figure 3-12).

The occurrence of this intermediate state in molecule C, in particular the structural differences at the switch II cluster and the neck linker, is not caused

by crystal contacts with the symmetry-related molecule and is not a crystallographic artifact (Figure 3-13). The B-factors for the switch II cluster and neck linker region, though higher than the average B-factor of the entire molecule, are consistent throughout molecules A, B and C.

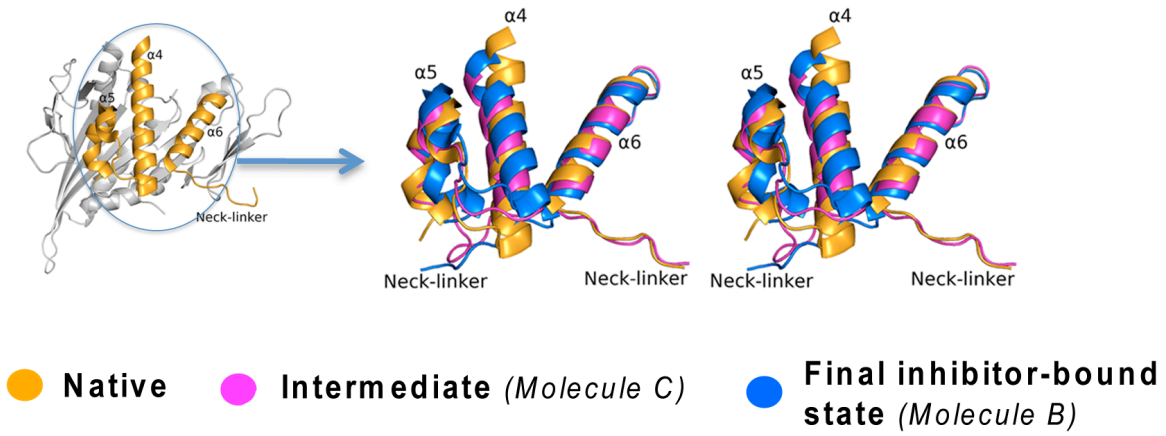

Figure 3-12. Overlay of native, intermediate and final states of the switch II cluster and neck linker region.

The switch II cluster (helix α4, loop L12 and helix α5) and the neck linker region, enlarged and shown as stereoplot insets, undergo conformational changes from native to intermediate (molecule C) to final inhibitor-bound state (molecule B). Helix α4 opens up space for the neck linker to dock.

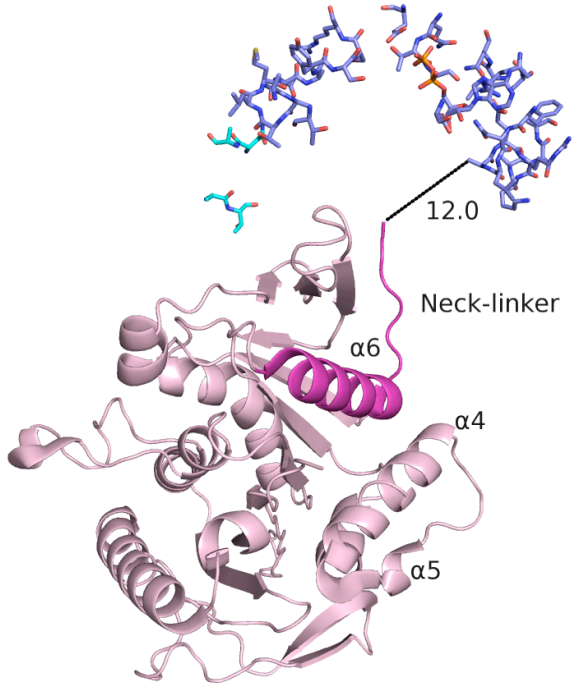

Figure 3-13. Closest crystal contacts to the neck linker of the intermediate state.

The neck linker of the intermediate state (molecule C) is extended perpendicular to helix α6. This figure shows all the residues within a 20 Å radius of Pro363 of the neck-linker. Ala31 of the symmetry-related molecule is the closest residue to Pro363, with a distance of 12 Å between them. There are no residues close enough to form crystal contacts with the neck linker.

3.2.5 Isothermal Titration Calorimetry

To obtain a thermodynamic analysis of STLC binding to Eg5, ITC binding studies were performed. The titration of Eg5 with ispinesib, a specific inhibitor currently in clinical trials, was used as a control and the values obtained were compared to those found in a similar study by Sheth *et al.*[172]. Representative calorimetric titrations of Eg5 with ispinesib and STLC, fitted to a standard single-binding site model, are shown in Figures 3-14a and b respectively. The averaged and calculated thermodynamic parameters of Eg5-ligand binding are shown in Table 3-4.

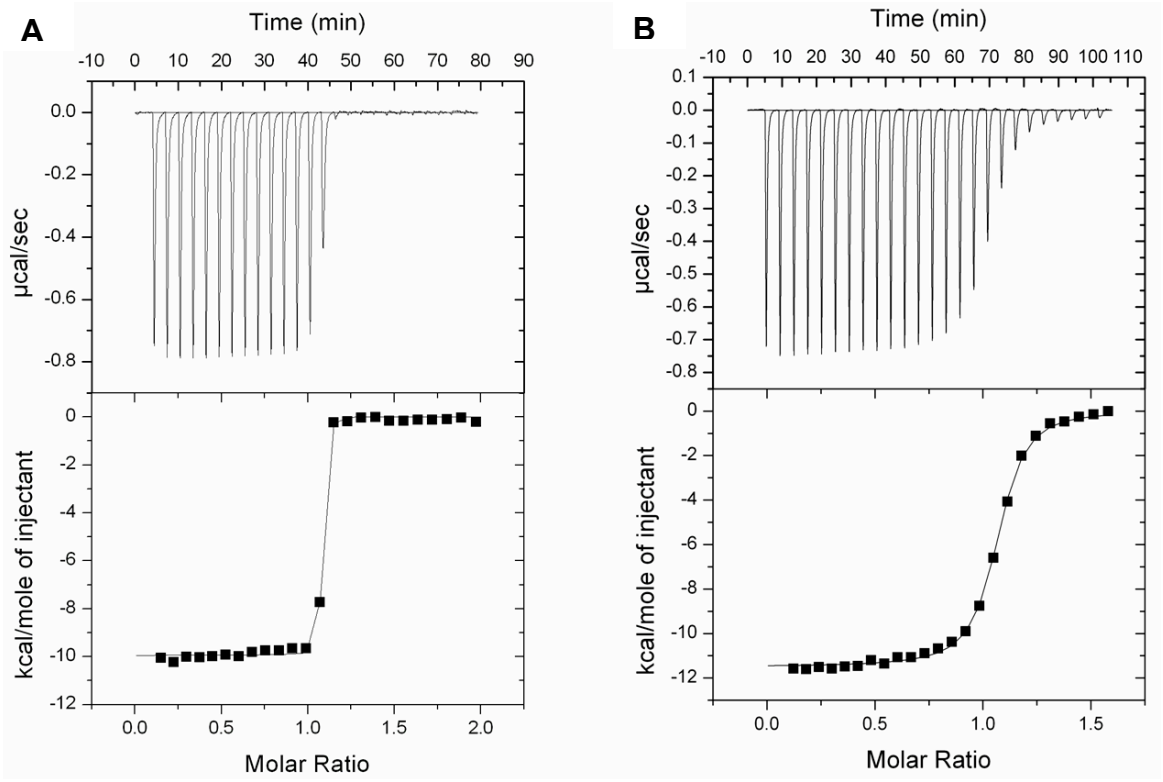

Figure 3-14. Representative calorimetric titrations of Eg5 with ispinesib and STLC.

Upper panel shows the raw ITC data (exothermic heat exchange) of inhibitor binding to Eg5, while the bottom panel shows the normalised ITC data (after subtracting the heats of dilution) plotted against the molar ratio of ligand to protein, and fitted to a standard single-binding site model. Titration of **(A)** ispinesib and **(B)** STLC with Eg5.

Table 3-4. Thermodynamic parameters of ligand binding to Eg5.

	Eg5-ispinesib	Eg5-STLC
Stoichiometry (no. of sites per mole of protein)	1.05 ± 0.002	1.08 ± 0.002
K_a (10^8 M^{-1}) [a]	5.58 ± 2.68	0.104 ± 0.006
K_d (μM)	0.002	0.096
ΔH (kcal/mol) [a]	-9.98 ± 0.05	-11.17 ± 0.04
TΔS (kcal/mol) [a]	1.79 ± 0.70	-1.59 ± 0.42

[a] Values determined at 298.15 K, T = temperature in Kelvin.

The binding stoichiometries of ispinesib and STLC to Eg5 were calculated to be 1:1, which means that there is one ligand binding site per protein. From the binding curves (Figure 3-14), it can be seen that the data fits well to the standard single-binding site model. The association constant for the Eg5-ispinesib complex is higher than that of the Eg5-STLC complex. Thus, the dissociation constant, which is inversely proportional to the association constant, is smaller for the Eg5-ispinesib complex than the Eg5-STLC complex. Both binding events of Eg5-ispinesib and Eg5-STLC are enthalpically favourable, as shown by the negative enthalpy change. On the other hand, the binding event of Eg5-ispinesib is entropically favourable, as shown by the positive entropy change, while that of Eg5-STLC is entropically unfavourable.

3.3 Discussion

3.3.1 Structure-activity relationship study of monastrol analogues

Based on the *in vitro* microtubule-stimulated ATPase assays done by Gartner *et al.*[82], enastron (IC_{50} = 2 μM) and dimethylenastron (IC_{50} = 200 nM) have been shown to be 15 and 150 times more potent than monastrol (IC_{50} = 30 μM). By comparing the crystal structures of Eg5 in complex with each of the three inhibitors, we hope to understand how the structural differences of the three inhibitors could contribute to the varying levels of potency. Upon overlaying the

Eg5-enastron and Eg5-dimethylenastron structures with Eg5-monastrol[91], no differences in the positions of the three inhibitors in the allosteric binding site were observed. The interactions between the inhibitors and the residues in the inhibitor-binding pocket are also virtually identical. The only striking difference is that enastron and dimethylenastron have the oxo-cyclohexene system, while monastrol has a C5-ester group.

The crystal structure of the Eg5-monastrol complex[91] shows that the ester group of monastrol extends out of the allosteric binding site into the solvent-exposed region, but does not completely fill the space in the solvent-exposed sub-pocket (Figure 3-15). In contrast, the oxo-cyclohexene group of enastron results in a better fit of the inhibitor in the solvent-exposed sub-pocket formed by Glu215, Tyr211 and Arg119. Therefore, we concur with Gartner *et al.*[82] that the cyclisation of the side chain, resulting in a cyclic ketone, confers rigidity to the conformation of the inhibitor. The rigid conformation and the better fit of the inhibitor are the likely reasons for the 10 times increase in potency of enastron as compared to monastrol. In view of the small structural difference — namely the two methyl groups — between enastron and dimethylenastron, it seems surprising that the latter is about 10 times more active than enastron *in vitro*. The increase in potency would most likely be due to the C—H---π interaction that one of the methyl groups forms with Tyr211. In addition, the dimethyl group of dimethylenastron occupies the space of the solvent-exposed sub-pocket with a better fit to the allosteric binding site than enastron.

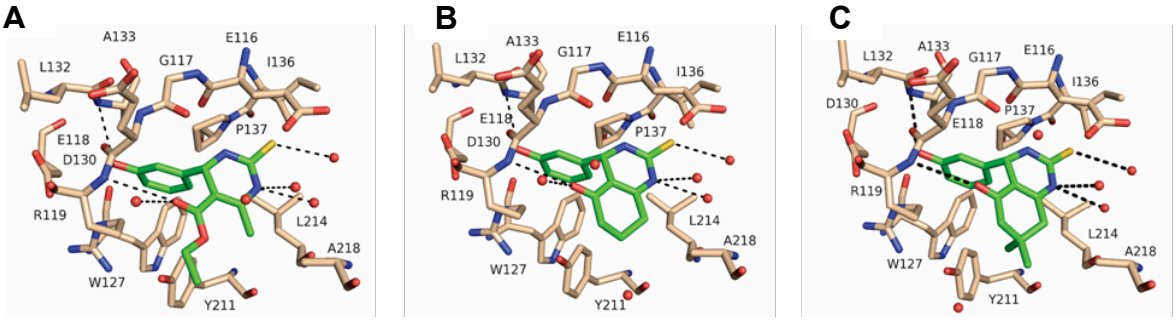

Figure 3-15. Crystal structures reveal better fit of inhibitor as reason for increased potency.
Crystal structures of **(A)** Eg5-monastrol (PDB ID: 1X88)[91], **(B)** Eg5-enastron and **(C)** Eg5-dimethylenastron.

By comparing the crystal structure of Eg5-fluorastrol to that of a structurally similar inhibitor mon97[138] (Figure 3-16), we can try to understand the reason behind the approximate five-fold increase in potency of fluorastrol as compared to mon97 in cell-based assays (Table 3-5). Upon overlaying the two structures, no differences in the positions of the main scaffold or interactions of the two inhibitors with the rest of the protein were observed. The only difference between the two inhibitors is the two fluorines that are attached to the phenyl ring in the *meta*- and *para*-positions. One of these fluorines plays an important role in forming multipolar interactions with the residues at the allosteric binding site, while the other fluorine points towards Phe239.

Additionally, the aromatic ring stacks with the salt bridge formed by the side chain residues of Glu116 and Arg221. The two fluorine atoms and the carbonyl group withdraw electron density from the phenyl ring by inductive and mesomeric effects respectively. Thus, the fluorine atoms, bearing higher electron density, are closer to the positively-charged side chain of Arg221 and the electron-poor edge of Phe239, while the phenyl ring that has lower electron density is closer to the negatively-charged side chain of Glu116. This explains the overall improved affinity of this compound. In fact, there have been previous examples where the addition of fluorines to lead compounds has beneficial effects on the physico-chemical properties of the drug, and has strengthened the protein-ligand interactions. These major fluorinated drugs include Prozac, an antidepressant, and Lipitor, a cholesterol-lowering drug[170].

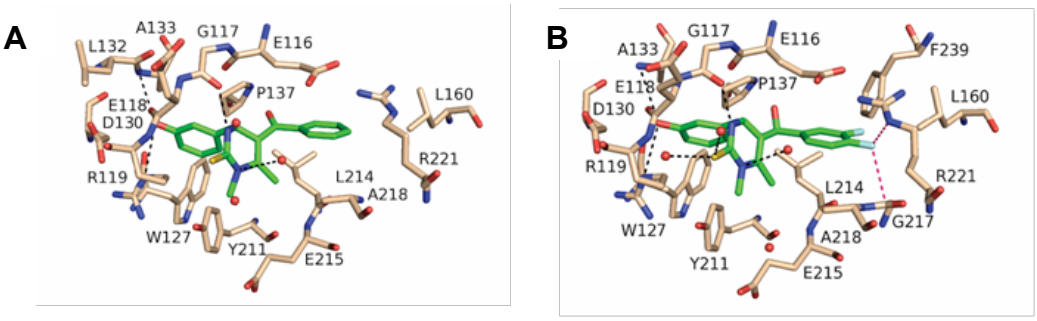

Figure 3-16. Crystal structures reveal addition of fluorine atoms as reason for increased potency.

Crystal structures of **(A)** Eg5-mon97 (PDB ID: 2IEH)[138] and **(B)** Eg5-fluorastrol.

Table 3-5. Growth inhibition assays of monastrol-like compounds conducted in different cell lines.

	EC_{50} [nM] [a]			
Compound	HCT116	hTERT-HME1	BxPC3	K562
rac-monastrol	24155 ± 2848	45082 ± 21354	> 100 µM	> 100 µM
rac-enastron	1811 ± 175	2443 ± 245	2072 ± 483	4775 ± 337
rac-dimethylenastron	330 ± 17	603 ± 44	743 ± 104	769 ± 71
rac-fluorastrol	387 ± 22	247 ± 42	601 ± 105	1149 ± 46
fluorastrol-E1	15171 ± 1582	> 100 µM	33651 ± 10182	26607 ± 1465
fluorastrol-E2	327 ± 54	223 ± 48	736 ± 91	820 ± 20
rac-mon97	1832 ± 182	1778 ± 140	5000 ± 671	5688 ± 648
mon97-E1	6502 ± 487	> 50000	14421 ± 1753	11405 ± 671
mon97-E2	1740 ± 111	1187 ± 87	3597 ± 193	3695 ± 507

[a] Growth inhibition assays were carried out by Oliver Rath and published in Kaan *et al*., 2010, J. Med. Chem.[173], using human colon (HCT116), lung (NCI-H1299), pancreas (BxPC3) and leukemia (K562) tumour cell lines. rac = racemic, E1 = enantiomer 1 and E2 = enantiomer 2.

Besides providing structural evidence for the increased potency of inhibitors, the crystal structures also reveal the preferential binding modes of the inhibitors. For the improvement of small molecule inhibitors, it is essential to understand the stereoselectivity of the compound. By crystallising the racemic mixture of enastron and dimethylenastron with Eg5, it was found that the *S*-enantiomer of both inhibitors binds preferentially to Eg5 in the respective crystal structures. Therefore, we predict that the *S*-enantiomer of enastron and dimethylenastron, rather than the *R*-enantiomer, is the active agent. Consequently, they belong to class I of dihydropyrimidine (DHPM)-derived inhibitors that bind in the *S* configuration, similar to monastrol.

Though all three small molecules, enastron, dimethylenastron, and fluorastrol, are DHPM inhibitors, they exhibit different stereoselectivity. While enastron and dimethylenastron bind preferentially to Eg5 in the *S* configuration, fluorastrol

binds preferentially in the *R* configuration as shown by the crystal structure. This unexpected configuration is backed by results of *in vitro* assays[174] (Table 3-6), which show that the preferred binding mode (*R*-enantiomer) is the more active agent. Likewise, based on the structure of the Eg5-mon97 complex solved by Garcia-Saez *et al*.[138], the inhibitor mon97 was found to bind preferentially in the *R* configuration and hence belong to class II of DHPM inhibitors. Accordingly, fluorastrol is also a class II DHPM inhibitor.

Table 3-6. Inhibition of basal ATPase activity of Eg5 by fluorastrol and mon97.

Compound	IC_{50} [nM] [a]
rac-fluorastrol	393.8 ± 59.6
S-fluorastrol	3457.4 ± 118.6
R-fluorastrol	279.1 ± 59.7
rac-mon97	466.5 ± 41.4
S-mon97	952.6 ± 70.0
R-mon97	334.8 ± 12.8

[a] Values taken from Prokopcova *et al*., 2010, Chem. Med. Chem.[174]

3.3.2 Structure-activity relationship study of STLC and its analogues

Determination of the Eg5-STLC structure has revealed several important interactions between the cysteine moiety and Eg5 residues that contribute to the potency of STLC. The three phenyl rings of the inhibitor are buried in the mostly hydrophobic part of the inhibitor-binding pocket and form aromatic interactions with several Eg5 residues. To further improve the potency of STLC, our lab decided to synthesise STLC analogues bearing a *para*-substitution on one of its phenyl rings. As free rotation is possible around the C-S bond, the phenyl rings can interchange positions in the three sub-pockets of the inhibitor-binding site. Hence, it is difficult to determine where the *para*-substituted phenyl ring will be placed. Nevertheless, the new crystal structures of Eg5 in complex with

these STLC analogues will shed light on the position of the *para*-substituted phenyl ring.

Ms. Katarzyna Tkocz, a six-month internship student under my supervision, solved the crystal structure of Eg5 in complex with an STLC analogue carrying a *para*-substituted chlorine on one of its phenyl rings (compound **10**). The structure is published in Kaan *et al.*, 2011, J. Med. Chem.[175]. The well-defined electron density map revealed that the substituted phenyl ring is buried in the mainly hydrophobic pocket formed by Ile136, Pro137, Leu160, Leu214, Phe239 and the salt bridge between Glu116 and Arg221 (Figure 3-17). Taken together with the structures of Eg5-STLC and Eg5-**6**, and the *in vitro* ATPase assay results (Table 3-7), one can begin to understand the factors affecting the potency of these small molecule inhibitors.

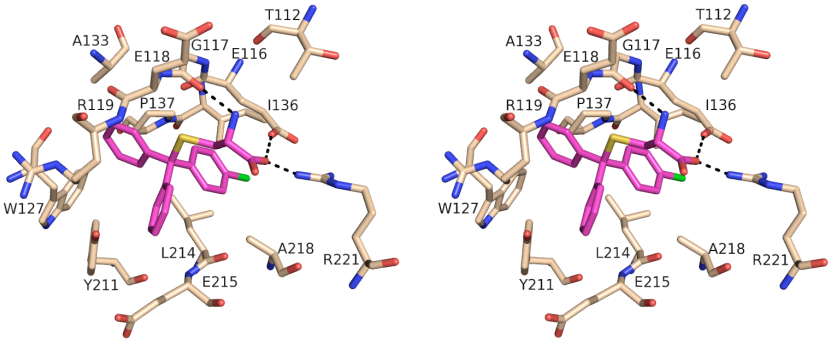

Figure 3-17. Stereoplot of compound 10 in the inhibitor-binding pocket.

Hydrogen bonds between inhibitor (pink) and Eg5 residues (beige) or structural water molecules (red spheres) are depicted by black broken lines.

Table 3-7. Inhibition of microtubule-stimulated ATPase activity of Eg5 by STLC, compound 6 and 10.

Compound	IC_{50} [nM] [a]
STLC	284.9 ± 13.7
Compound **6**	548.9 ± 130.0
Compound **10**	53.3 ± 1.5

[a] Values taken from Kaan *et al.*, 2011, J. Med. Chem.[175].

Compound **6**, which has a phenyl ring replaced by a –CH(Me)Et alkyl chain, has a slight decrease in potency compared to STLC. The substitution of the phenyl ring by the alkyl chain results in the loss of an offset stacked π-π interaction between the phenyl group and Tyr211. This could be the main reason for the slight decrease in potency; thus, substitution of an entire phenyl ring by an alkyl chain is unlikely to improve the potency of an inhibitor. Hence, *para*-substitution on the phenyl ring was considered. From the data above, it can seen that a small lipophilic *para*-substitution on one of the phenyl rings can increase the potency of STLC by approximately five times. This is further substantiated by the SAR study described in Kaan *et al.*[175], which showed that when one phenyl ring carries a small lipophilic *para*-substituent, such as iodine, bromine, methyl or ethyl, the potency of the small molecule is greatly improved. The crystal structure also reveals that the small lipophilic group sits in the complementary hydrophobic environment (P3 sub-pocket, Figure 3-18), which could be a factor resulting in improved potency.

With the knowledge gained from this SAR study, the next step was to synthesise STLC analogues with *meta*-substituents on one or more of its phenyl rings to confirm the trend that a small lipophilic substituent on a phenyl ring can improve the potency of the inhibitor. In addition, we decided to probe the importance of the sulphur atom and the carboxylic group in relation to the potency of the small molecule. Thus, in this second SAR study, we discuss the crystal structures together with the *in vitro* ATPase assay results and the multidrug resistance (MDR) ratio (Table 3-8) for compounds **7** to **9**.

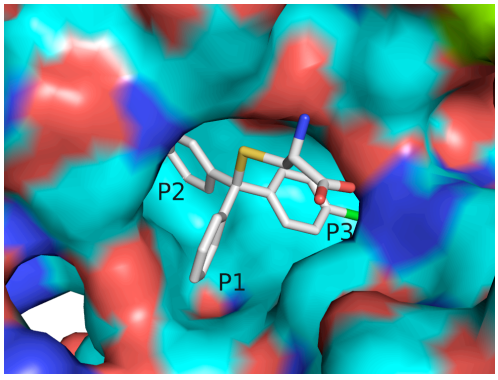

Figure 3-18. Surface diagram showing the three sub-pockets in the inhibitor-binding pocket. Compound 10 is shown in the pocket with the *para*-substituted phenyl ring in the P3 sub-pocket.

Table 3-8. Compounds tested in basal ATPase assay and growth inhibition assay.

Compound	K_i^{app} [nM] [a]	EC_{50} [nM] [b]	MDR ratio [c]
STLC	185.9 ± 20.5	1452 ± 76	42
Compound **7**	12.2 ± 3.8	73 ± 3	83
Compound **8**	185.8 ± 30.4	706 ± 47	nt
Compound **9**	16.0 ± 3.5	260 ± 19	9.1
Ispinesib	nt	nt	9.6

[a] Unpublished K_i^{app} values for the inhibition of basal Eg5 ATPase activity.

[b] Unpublished EC_{50} values for the growth inhibition of K562 human leukemia tumour cell line.

[c] Unpublished MDR ratios (EC_{50} value obtained with KB-V1 cells overexpressing P-glycoprotein divided by EC_{50} obtained with isogenic parental KB-3-1 cell line). nt = not tested.

Compound **7**, which is approximately 15 times more potent than STLC, has a *meta*-substituted methyl group on one of its phenyl rings and its sulphur atom has been replaced by a carbon. The crystal structure reveals that the methyl group sits in the same pocket as the chlorine substituent of compound **10**. This is in agreement with the trend that a small lipophilic substituent would fit into the complementary hydrophobic sub-pocket (P3) and improve the potency of the inhibitor. As the sulphur atom has not been shown to make any important interactions with the residues of the inhibitor-binding pocket, the substitution of sulphur with carbon does not appear to decrease its potency. In fact, the carbon analogue could be a better alternative as the sulphur has been shown to be a site for metabolism by the enzyme phenylalanine monoxygenase found in the human body[176]. Hence, the carbon analogue, which is less susceptible to acid hydrolysis and *S*-oxidation, may prove to be a more stable chemotherapeutic agent.

Nevertheless, compound **7** has a high MDR ratio of 83 compared to that of ispinesib, an Eg5 specific inhibitor in clinical trials; thus making it less than ideal for drug development in cancer therapy. It has long been known that tumours and tumour cell lines may develop drug resistance, *de novo* or acquired, against current microtubule-targeting drugs through a variety of putative mechanisms,

including the expression of point mutations in tubulins, overexpression of certain tubulin isoforms that are able to evade drug treatment, or multidrug resistance[77-79]. The best-known and probably the most important transporter for MDR is P-glycoprotein (Pgp, encoded by *ABCB1*), an efflux pump present in many tissues and tumours that has a very broad substrate specificity and is capable of eliminating xenobiotics, such as taxanes and vinca alkaloids from the cell[177]. To fight these liabilities associated with current treatments, efforts are underway to develop improved drugs with reduced susceptibility to MDR.

As the results show, compound **9** has a low MDR ratio, which is comparable to ispinesib. The low MDR ratio is attributed to the loss of the carboxylate group from the cysteine moiety and is backed up by more unpublished cell-based assay results of STLC analogues without the carboxylate group. However, the loss of the carboxylic acid, as shown by the crystal structures of **8** and **9**, results in the loss of a hydrogen bond with the Eg5 residue Arg221 and several hydrogen bonds with structural waters that act to stabilise and maintain rigidity of the amine tail. Due to the loss of the carboxylic acid, compound **8** though carrying a *meta*-substituted acetate group is about 15 times less potent than **7**. Nevertheless, the potency of compound **8** is comparable to STLC, thus demonstrating that the decrease in potency due to the loss of the carboxylate group may be compensated by the new hydrogen bond interaction between the acetate group and Arg221.

Lastly, arriving at compound **9**, we observe that *meta*-substitutions on two phenyl rings could greatly improve potency, while keeping the MDR ratio low by removing the carboxylate group. From the crystal structure, it can be seen that the lipophilic substituent (ethyl group) is positioned in the predicted P3 sub-pocket. The unexpected finding is the position of the second *meta*-substituent (hydroxyl group). It sits in the P2 sub-pocket, which is in the core of the protein, instead of the P1 sub-pocket that is solvent exposed. However, by placing the crystal structure of Eg5-**9** alongside Eg5-monastrol, one can see that the 3-hydroxyphenyl group that is common to both inhibitors and to other monastrol analogues, sits in the same P2 sub-pocket (Figure 3-19). In this position, it forms a hydrogen bond with Ala133, stabilises the inhibitor in the allosteric site and increases the affinity of the ligand to the protein.

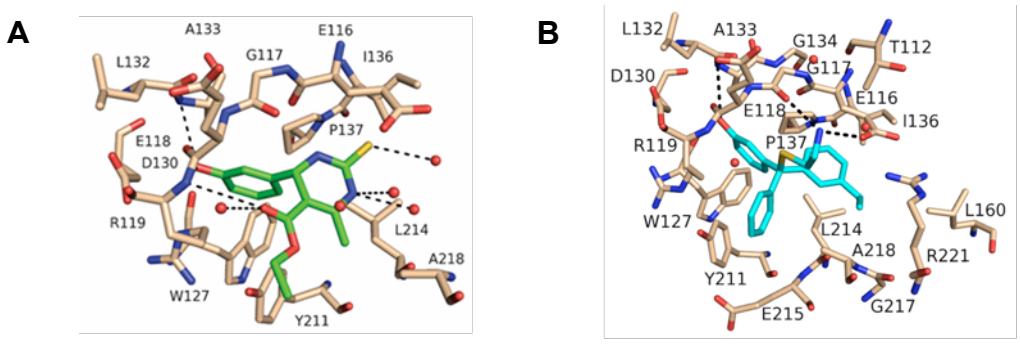

Figure 3-19. Comparison of Eg5-monastrol and Eg5-9 structures.

Inhibitor-binding pocket of **(A)** Eg5-monastrol (PDB ID: 1X88)[91] and **(B)** Eg5-9 complex. The 3-hydroxyphenyl group, common to both inhibitors, sits in the P2 sub-pocket in the core of the protein.

3.3.3 Pathway of structural change upon inhibitor binding

Although several crystal structures of Eg5 in complex with inhibitors have been deposited in the Protein Data Bank, all of them exhibit the same conformation and structural changes representative of the final state of the inhibitor-bound Eg5. As the crystal structures are static images, it remains unclear how these structural changes come about and what the sequence of events leading to the final inhibitor-bound state may be. Kinetic studies by Maliga *et al.*[92] propose a model in which, following monastrol binding to the Eg5 motor domain, the downward swing of loop L5 occurs first, followed by conformational changes in the switch II cluster, which allows the neck linker to dock.

In this chapter, we report the crystal structure of an unprecedented intermediate state (molecule C) of the Eg5-STLC complex. By comparing the structure of native Eg5 with molecules C and B of the Eg5-STLC complex, we can dissect the pathway of structural changes that occur upon inhibitor binding. Hereafter, the structures of molecules A and B, which have similar conformations, will be referred to as the final inhibitor-bound state, while the structure of molecule C will be referred to as the intermediate state.

From the crystal structures, it can be seen that upon inhibitor binding, local changes in the inhibitor-binding pocket and at the switch I region have taken place in the intermediate and final states. However, in the intermediate state, the switch II region has not reached the conformation observed in the final state, and the neck linker remains undocked. The conformational changes observed in the intermediate state of the Eg5-STLC structure is consistent with that expected after initial inhibitor binding — significant local changes at the inhibitor-binding pocket — but before the docking of the neck linker.

Significantly, the changes in the intermediate state are moving in the direction of the final state. Complete conversion only occurs in the final inhibitor-bound state, where the neck linker becomes docked. Therefore, we propose that the binding of STLC to Eg5 causes drug-induced structural transition in 3 steps: first, loop L5 swings downwards to close the inhibitor-binding pocket, which then translates to an upward shift of the switch II cluster toward the N-terminal of helix α4, and finally the neck linker docks onto the motor domain (Figure 3-20).

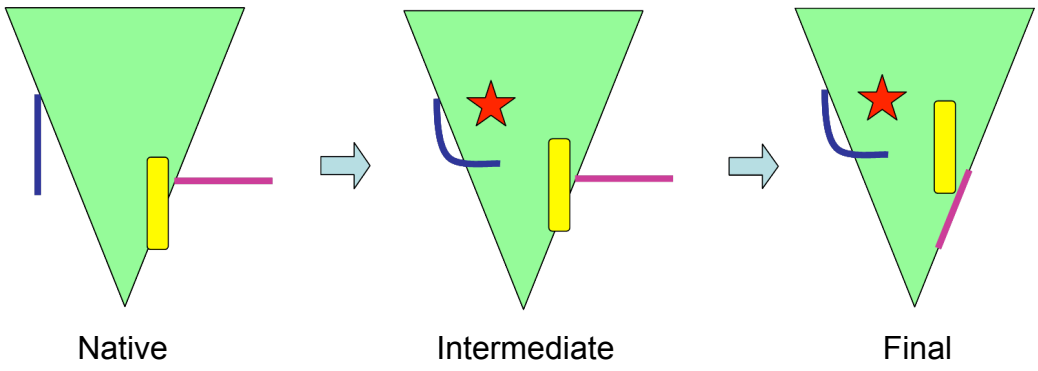

Figure 3-20. Schematic diagram of the proposed pathway of structural changes upon inhibitor binding.

From native to intermediate to final inhibitor-bound state. Green: Eg5, red: inhibitor, blue: loop L5, yellow: switch II cluster and magenta: neck linker.

3.3.4 Biophysical characterisation of Eg5-inhibitor complexes

ITC binding study was performed to obtain a thermodynamic analysis of STLC binding to Eg5. A control experiment was also carried out for the binding of ispinesib to Eg5 at 25°C and the results obtained were compared to that of a similar study conducted by Sheth *et al*.[172] at 20°C. The binding stoichiometry of ispinesib to Eg5 obtained from our study is 1.05 ± 0.002, which is in close agreement with the value obtained from their study (0.85 ± 0.2). Our study revealed a dissociation constant of 0.002 μM, which also agrees with their result of < 0.01 μM. As ispinesib is a very potent inhibitor, the association constant is large and only one data point is observed at the slope of the titration curve before the system becomes saturated. Hence, the K_a and K_d cannot be accurately determined, but are considered estimates.

While our study showed an enthalpy change of -9.98 ± 0.05 kcal/mol, theirs showed an enthalpy change of -6.1 ± 0.2 kcal/mol. Lastly, our study revealed an entropy change of 1.79 ± 0.70 kcal/mol, while theirs revealed an entropy change of 5.2 kcal/mol. The slight difference in values obtained could be attributed to the fact that both experiments were conducted at difference temperatures. Nevertheless, both studies showed a negative enthalpy change and a positive entropy change; thus confirming that the binding event of ispinesib to Eg5 is enthalpically and entropically favourable.

Having confirmed that the results obtained from our control experiment is reliable and in accordance with a similar study, I went on to analyse the binding event of STLC to Eg5. The calculated binding stoichiometry (1:1) is in full agreement with the crystal structure of the Eg5-STLC complex, which shows one inhibitor binding site per protein molecule. By fitting the data to a standard single-binding model, I obtained a dissociation constant of 0.096 μM, which is approximately 50 times larger than that for Eg5-ispinesib. This alludes to the fact that the binding of ispinesib to Eg5 is much tighter than that of Eg5-STLC.

Under my supervision, Ms. Katarzyna Tkocz also solved the crystal structure of Eg5 in complex with ispinesib (unpublished data). The four aromatic rings of ispinesib are buried in the allosteric site and display several hydrophobic

interactions with residues of the inhibitor binding pocket (Figure 3-21). The coupled rings (quinazoline ring) of ispinesib are stabilised on one side by a salt bridge formed between side chains of Glu116 and Arg221 and on the other side by C—H---π interaction with Leu214. The phenyl ring that is linked to the quinazoline ring stacks on the Pro137 ring, and is also involved in edge-to-face (T-shape) interaction with the phenyl ring of Trp127. The isopropyl group of ispinesib forms C—H---π interaction with the phenyl ring of Tyr211. Hydrogen bonds are also observed between the nitrogen (NAD) of ispinesib and the side-chain oxygen (OE1) of Glu116 and between the oxygen (DAE) of the inhibitor and a structural water molecule.

Comparing the structures of Eg5-ispinesib and Eg5-STLC, we see many similar hydrophobic and hydrogen bond interactions between both ligands and the protein. The only outstanding interaction is the stacking of the quinazoline ring with the salt bridge in the Eg5-ispinesib complex, which is not present in the Eg5-STLC complex. This interaction could be one of the reasons for the strong binding affinity of ispinesib to Eg5. Though we did not quantify the affinity of the bonds between the ligands and protein, nor did we measure the contributions of individual interactions to the changes in enthalpy and entropy for both Eg5-ispinesib and Eg5-STLC complexes, the thermodynamic parameters obtained from ITC give us information, in addition to the crystal structure, for gaining a better understanding of the binding event of ligand to protein.

Despite the big difference in binding affinities, the change in enthalpy for both binding events are negative, favourable and relatively similar. This shows that both reactions are exothermic and spontaneous. On the other hand, the entropy change for both events are opposite, with the change in entropy of Eg5-ispinesib being positive and favourable, while that of Eg5-STLC is negative and unfavourable. Nevetheless, the values are small with both being less than 2 kcal/mol. In short, the binding of ispinesib to Eg5 is tighter, more favourable and more spontaneous than that of STLC to Eg5. Hence, this could explain why ispinesib is approximately 20 times more potent than STLC in cell-based assays performed in various cell lines (Table 3-9).

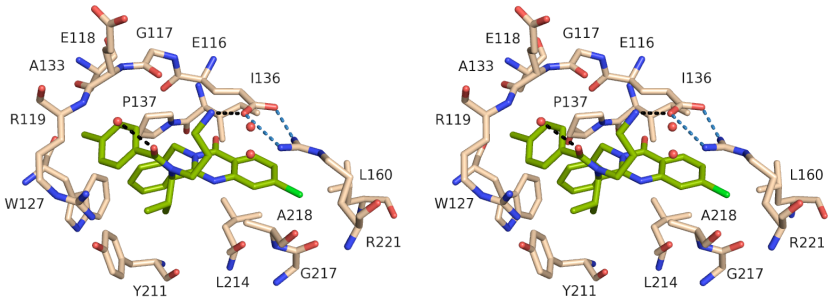

Figure 3-21. Stereoplot of ispinesib in the inhibitor-binding pocket.

Hydrogen bonds between inhibitor (green) and Eg5 residues (beige) or structural water molecules (red spheres) are depicted by black broken lines. Blue broken lines depict the salt bridge formed between Glu116 and Arg221.

Table 3-9. Growth inhibition assays of ispinesib and STLC conducted in different cell lines.

	EC_{50} [nM] [a]			
Compound	HCT116	NCI-H1299	BxPC3	K562
Ispinesib	25 ± 3	82 ± 10	80 ± 15	71 ± 8
STLC	553 ± 57	1549 ± 111	1563 ± 155	1452 ± 76

[a] Unpublished results from growth inhibition assays carried out by Oliver Rath, using human colon (HCT116), lung (NCI-H1299), pancreas (BxPC3) and leukemia (K562) tumour cell lines.

4 Mitotic kinesin Eg5 stalk$_{364-520}$ domain facilitates dimerisation

4.1 Aims and objectives

Eg5 consists of a 457-residue stalk domain in the middle of the protein that connects the motor to the tail domain. Unlike the motor domain, there is little information about and no crystal structures available for the stalk domain. Using a coil prediction program and based on the heptad repeats in its sequence, the stalk domain is predicted to form an interrupted coiled-coil structure. This special quaternary structure could help to explain the stalk domains involvement in the function of Eg5. Firstly, it is believed to facilitate oligomerisation of the Eg5 molecule into a bipolar tetramer, so that it can bind anti-parallel microtubules and slide them apart. Secondly, it may be involved in coordinating the 'hand-over-hand' motility of the molecular motor along microtubule tracks.

In this chapter, I will report the characterisation of the first 157 residues of the stalk domain, hereafter called the stalk$_{364-520}$ domain. Using analytical ultracentrifugation, I will determine the oligomerisation state and sedimentation coefficient of this region of the stalk domain. Then, I will present results obtained from a circular dichroism facility that reveal the percentage of helical content in the stalk$_{364-520}$ domain. Finally, I will describe the molecular envelope of the low resolution structure of stalk$_{364-520}$, determined by small angle X-ray scattering. Taken together, these results provide us with a glimpse into the structural characteristics of the Eg5 stalk$_{364-520}$ domain.

4.2 Results

4.2.1 Analytical Ultracentrifugation (AUC)

To start with, sedimentation velocity (SV) experiment was carried out to investigate if there is concentration-dependent oligomerisation behaviour and to

determine the sedimentation coefficient of the $stalk_{364-520}$ domain. Seven different concentrations of the $stalk_{364-520}$ domain were used for the experiment, which utilised both interference and absorbance optics. The resulting sedimentation profiles and data were fitted to a continuous c(s) distribution model using SEDFIT[159]. Individual size distribution c(s) profiles from the SV experiment using the interference optics are shown for all concentrations of samples in Figures 4-1a to g. Results from the SV experiment utilising the absorbance optics are not shown as the absorbance of the 20 mg/ml high concentration sample was beyond the linear range.

A

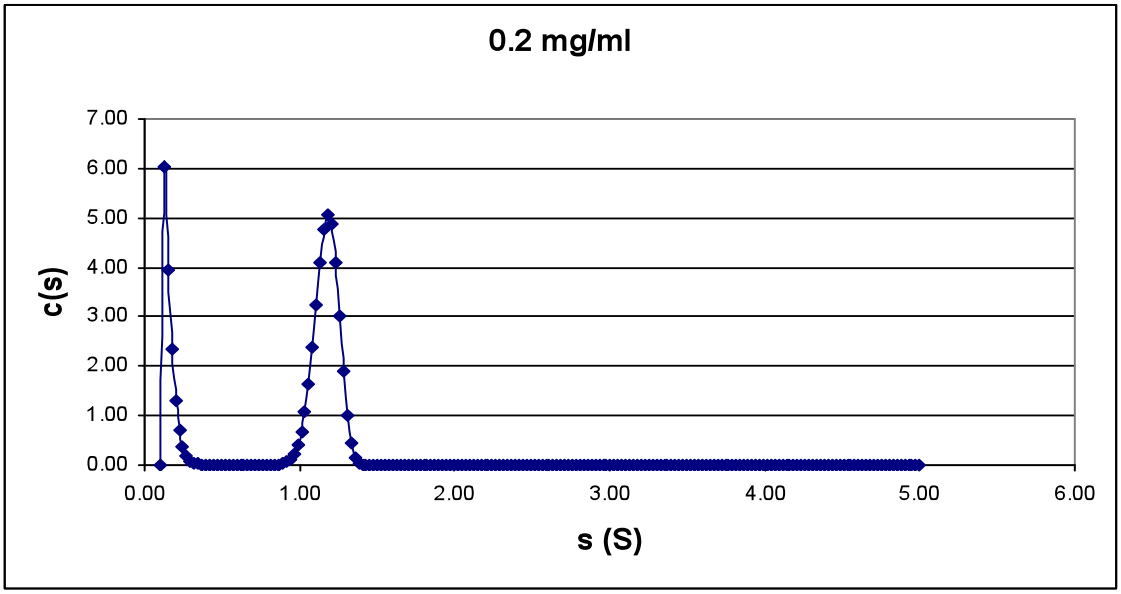

B

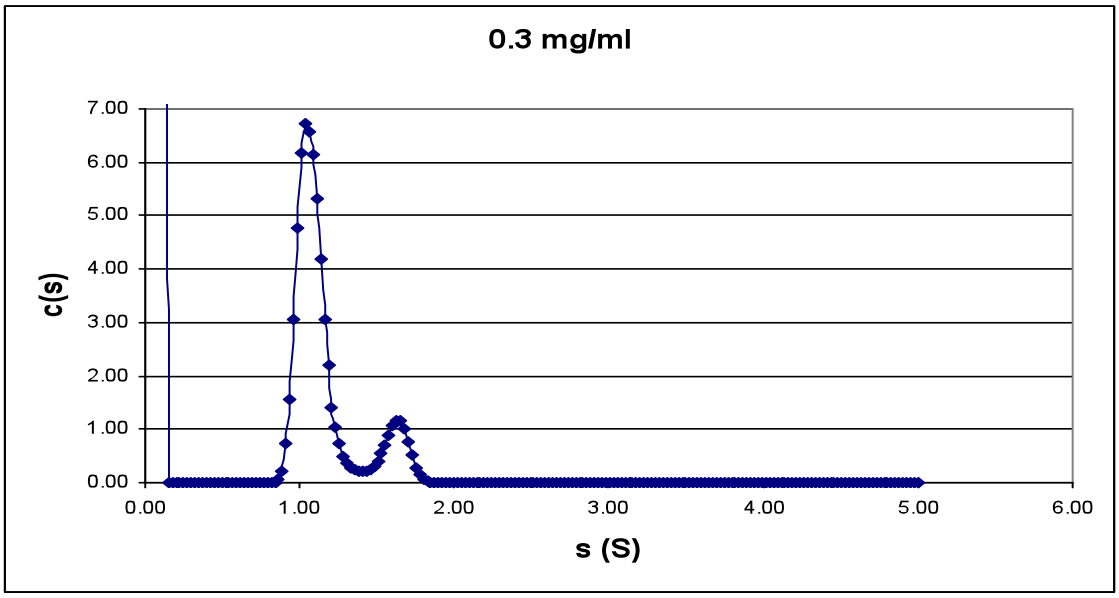

C

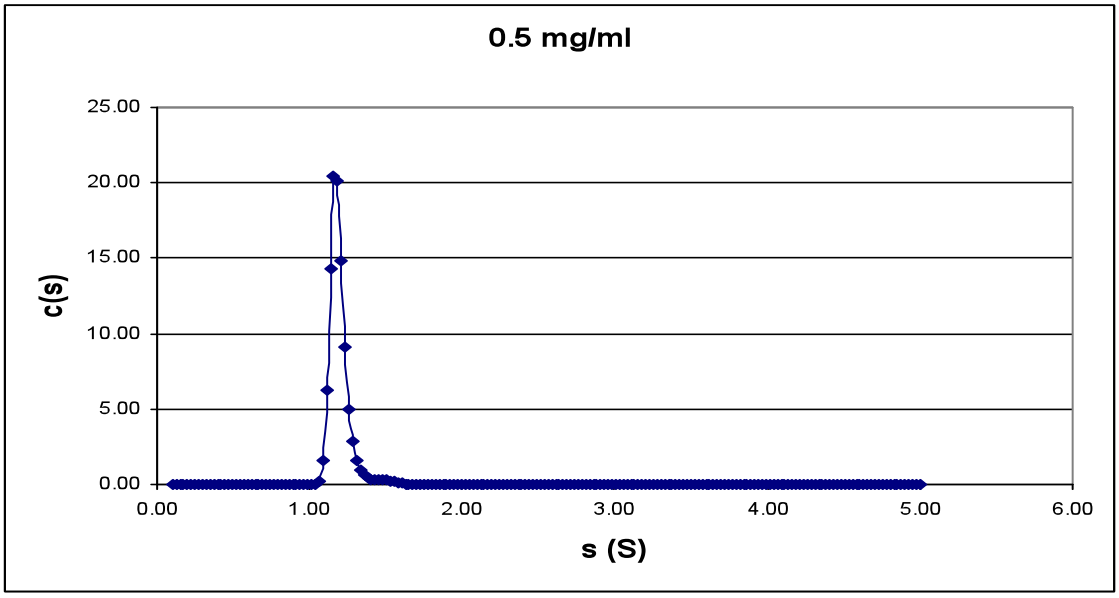
0.5 mg/ml
25.00
20.00
15.00
10.00
5.00
0.00
c(s)
0.00
1.00
2.00
3.00
4.00
5.00
6.00
s (S)

D

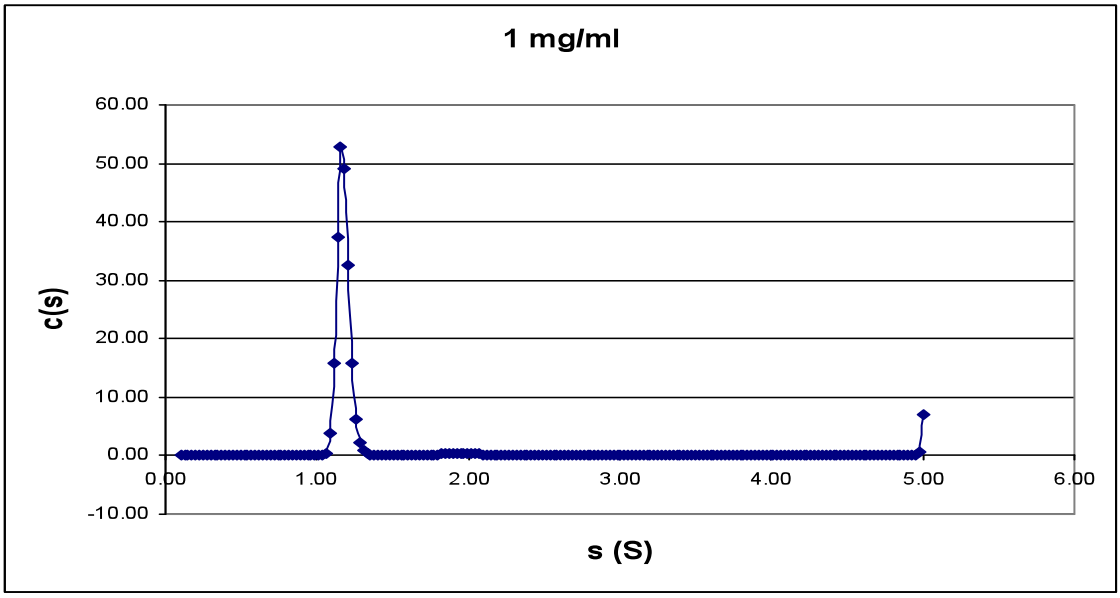
1 mg/ml
60.00
50.00
40.00
30.00
20.00
10.00
0.00
-10.00
c(s)
0.00
1.00
2.00
3.00
4.00
5.00
6.00
s (S)

E

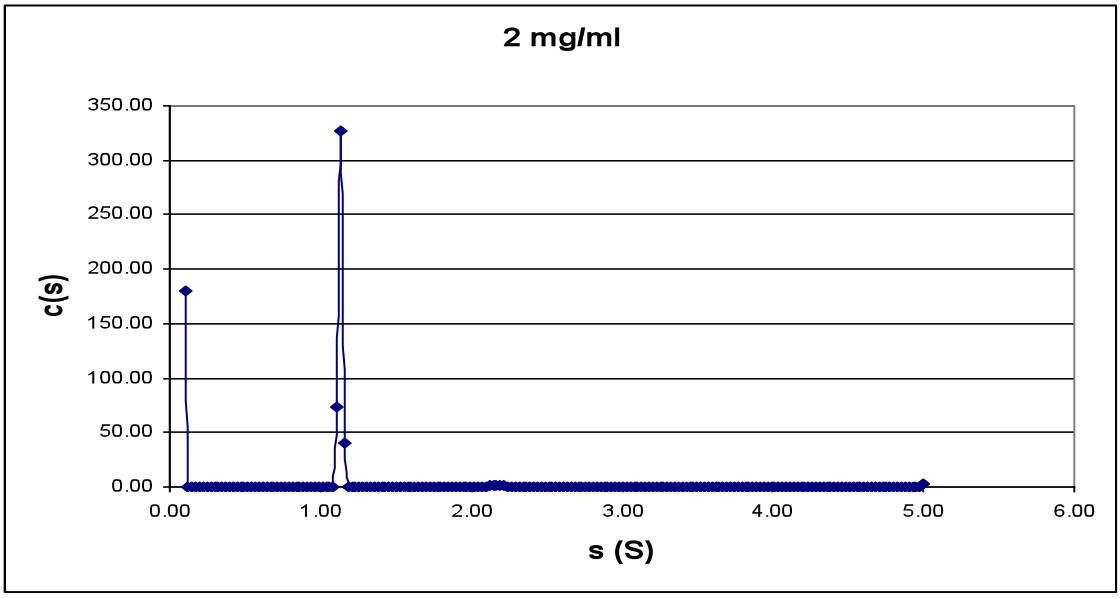
2 mg/ml
350.00
300.00
250.00
200.00
150.00
100.00
50.00
0.00
c(s)
0.00
1.00
2.00
3.00
4.00
5.00
6.00
s (S)

F

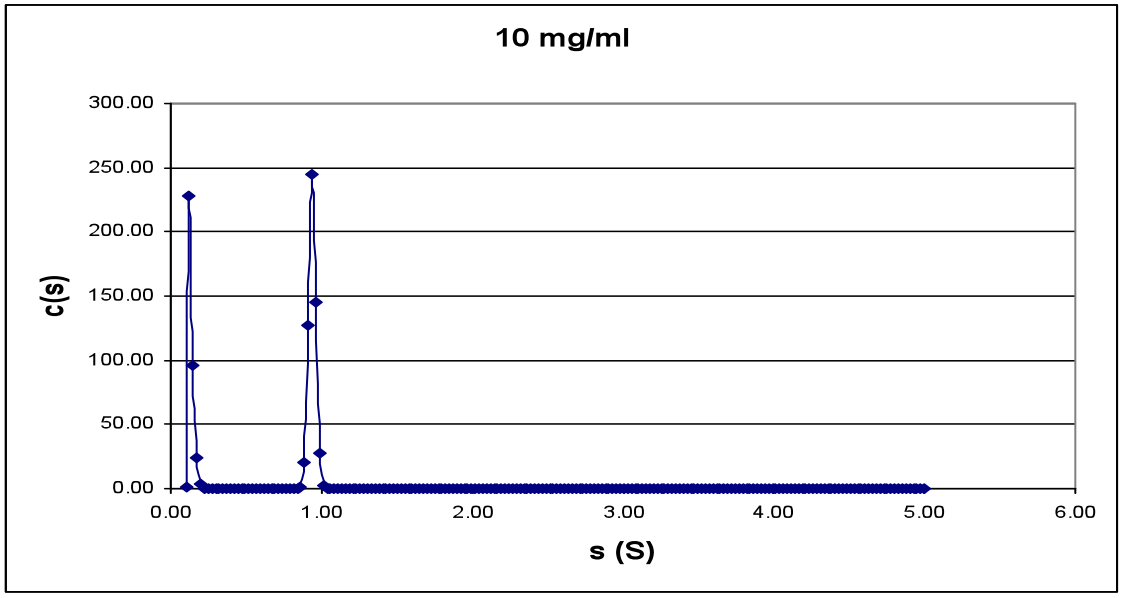

G

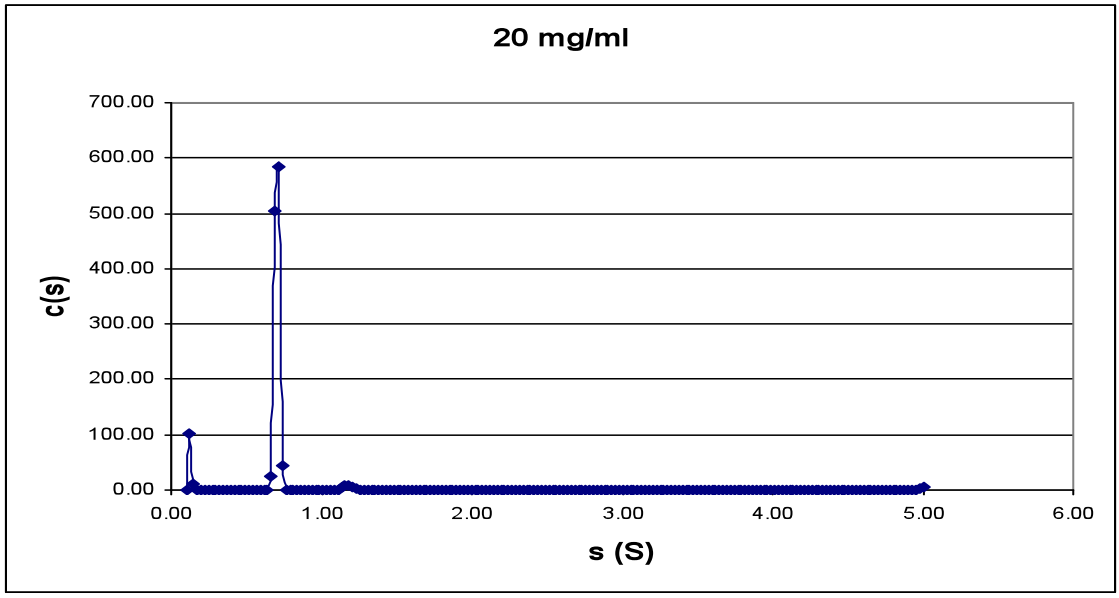

Figure 4-1. Individual size distribution c(s) profiles of samples analysed by SV experiment.

Size distribution profiles of Eg5 stalk$_{364\text{-}520}$ domain at concentrations of **(A)** 0.2, **(B)** 0.3, **(C)** 0.5, **(D)** 1.0, **(E)** 2.0, **(F)** 10 and **(G)** 20 mg/ml from the SV experiment utilising the interference optics.

From the size distribution profiles of the seven samples, one significant peak is observed for all concentrations. This peak corresponds to a sedimentation coefficient of about 1.2 S for samples with concentrations equal to or lower than 2.0 mg/ml. It then gradually shifts to a sedimentation coefficient of slightly less than 1.0 S for samples with concentrations equal to or higher than 10 mg/ml. Comparison and overlaying of the size distribution c(s) profiles shown below illustrates the gradual shift of the peak from about 1.2 to below 1.0 S (Figure 4-

2). In addition, a second smaller peak is observed for sample concentration of 0.3 mg/ml. This peak has a sedimentation coefficient slightly above 1.5 S. There is also a buffer peak at about 0.0 S for several sample concentrations.

From the c(s) profiles, the apparent sedimentation coefficient at 4°C in buffer ($s_{4,b}$) of the single species at different concentrations were extracted and listed in Table 4-1. The corresponding true sedimentation coefficient at 20°C in water ($s_{20,w}$) was calculated using equation 2 in section 2.2.3, to correct for the solvent viscosity and density. These values are also listed in Table 4-1. Subsequently, the $s_{20,w}$ values were plotted against the concentration of Eg5 stalk$_{364\text{-}520}$ domain and a linear regression was fitted to the data points (Figure 4-3). The y-intercept provides the value for the true sedimentation coefficient that is independent of concentration ($s^{\circ}_{20,w}$). Based on the good fit of the linear regression to the data points, $s^{\circ}_{20,w}$ of Eg5 stalk$_{364\text{-}520}$ domain is 1.76 S.

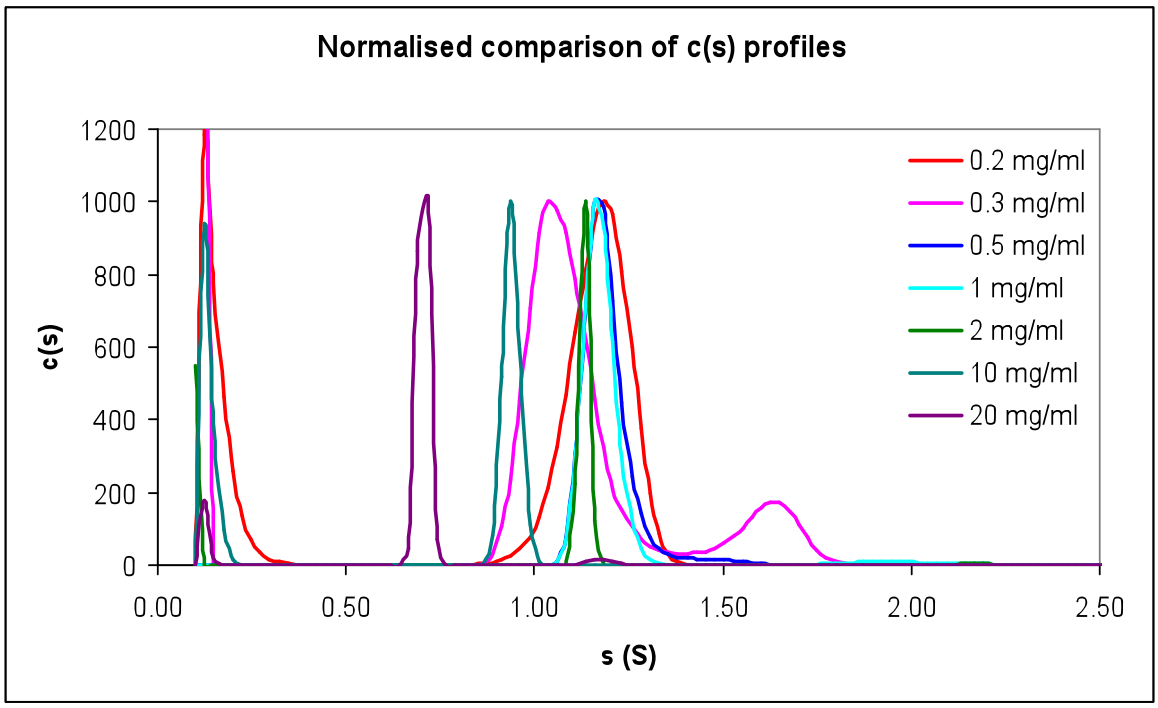

Figure 4-2. Normalised comparison of size distribution profiles.

Overlay of the normalised size distribution c(s) profiles of the seven samples of different concentrations obtained from the SV experiment utilising the interference optics. Gradual shifting of the peak from a sedimentation coefficient of approximately 1.2 to less than 1.0 S is observed with increasing concentrations of Eg5 stalk$_{364\text{-}520}$ domain.

Table 4-1. Apparent and true sedimentation coefficients for Eg5 stalk$_{364-520}$ domain.

Protein concentration (mg/ml)	$s_{4,b}$	$s_{20,w}$
0.2	1.11	1.70
0.3	1.17	1.79
0.5	1.17	1.79
1	1.13	1.72
2	1.11	1.69
10	0.87	1.33
20	0.68	1.04

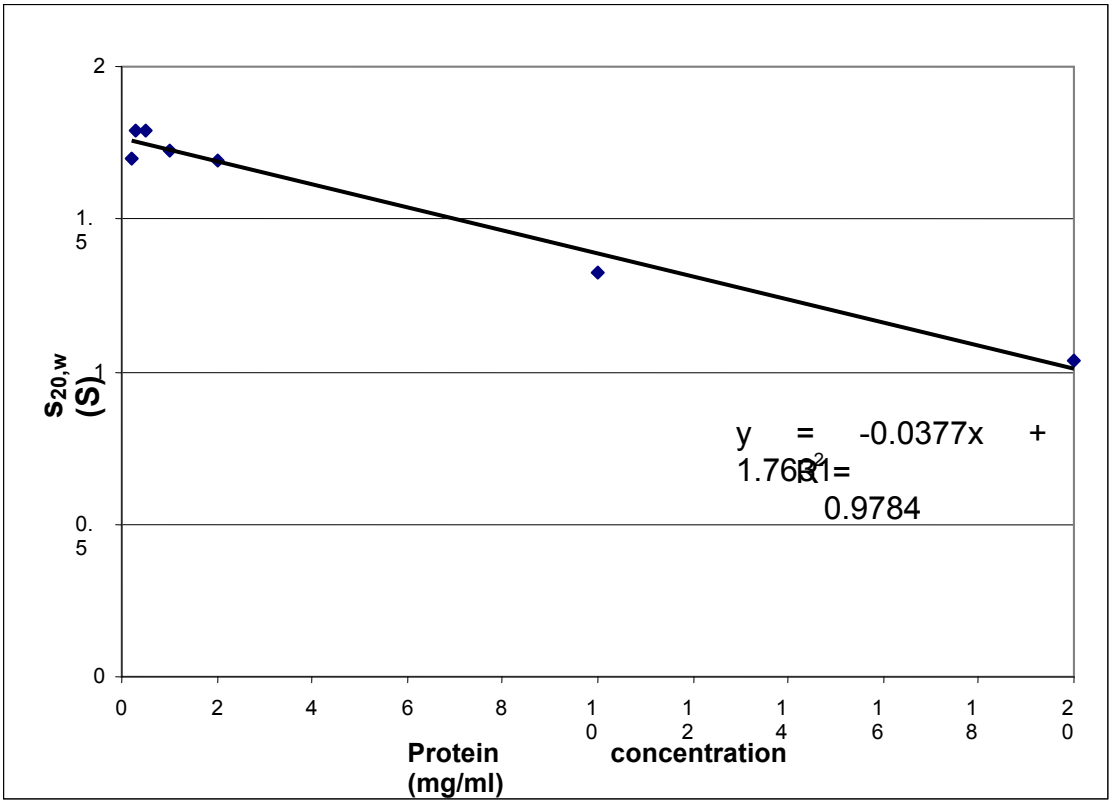

Figure 4-3. Plot of true sedimentation coefficient against concentration of Eg5 stalk$_{364-520}$ domain.

The calculated values of $s_{20,w}$ are plotted against the concentration of Eg5 stalk$_{364-520}$ domain. The y-intercept of the curve gives the true sedimentation coefficient that is independent of concentration. R^2 = goodness of fit, the closer the value is to 1, the better the linear regression fits the data.

A sedimentation equilibrium (SE) experiment utilising the interference optics was carried out for the seven samples, at two rotor speeds (20000 and 30000

rpm), to determine the apparent weight average molecular weight ($M_{w,app}$) of the single species observed in the SV experiment. The data quality and results were analysed using SEDPHAT[160]. All the data sets were individually fitted with the species analysis model under the assumption that the protein is dimeric and has an approximate dimeric mass of 36325 Da. Overall, the fit of most data to the model were good, as evident from the almost perfect superimposition of the data and model, low r.m.s.d. values and small residuals that are well-dispersed (Figure 4-4).

The $M_{w,app}$ and r.m.s.d. value for each protein sample is presented in Table 4-2. Subsequently, the $M_{w,app}$ values were plotted against the concentration of Eg5 $stalk_{364-520}$ domain (Figure 4-5). The distribution of points on the plot reveal a trend in which the $M_{w,app}$ value decreases with increasing concentration, for both rotor speeds. Hence, the $M_{w,app}$ is close to the molecular weight of dimeric Eg5 $stalk_{364-520}$ domain at low concentrations, near 0 mg/ml. Finally, the data sets for the SE experiment at each rotor speed were globally fitted to the above-mentioned model to obtain the global $M_{w,app}$ (Table 4-3). However, the global fit of the data to the model was not as good as the individual fits. Hence, data sets that have relatively higher r.m.s.d. values (10 and 20 mg/ml) were excluded from the subsequent global fit of the data sets at 30000 rpm. As a result, the overall $M_{w,app}$ of the Eg5 $stalk_{364-520}$ domain is 37826 Da.

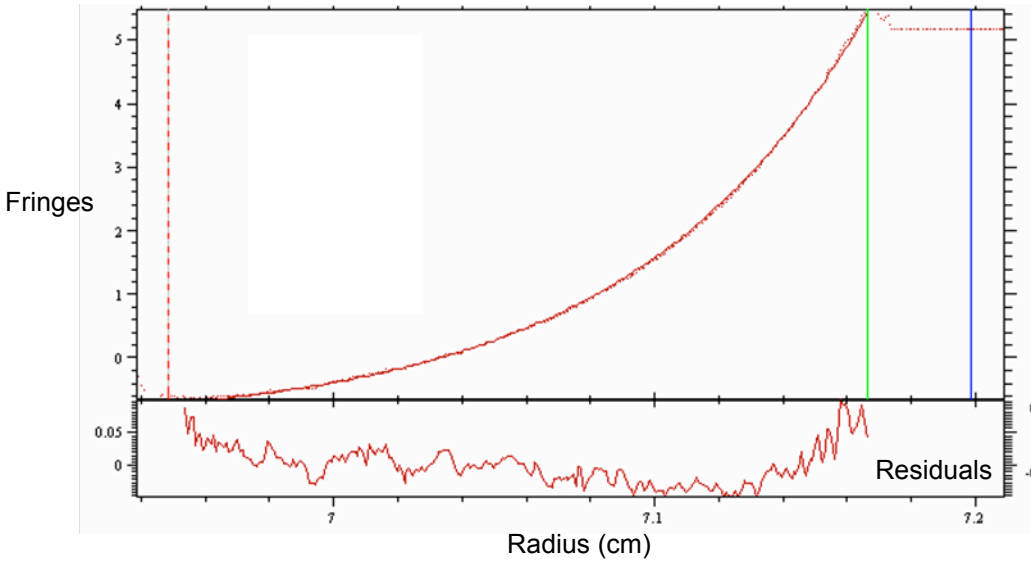

Figure 4-4. Representative SE profile fitted almost perfectly to the model.

Good fit of the data to the model is evident from the almost perfect superimposition of the data and model, small residuals that are well-dispersed and a low r.m.s.d. value of 0.028.

Table 4-2. $M_{w,app}$ and r.m.s.d. of all samples determined by SE experiments at 20000 and 30000 rpm.

Rotor speed (rpm)	Protein conc. (mg/ml)	$M_{w,app}$ (Da)	r.m.s.d. (fringes)
20000	0.2	37617	0.01
	0.3	34679	0.11
	0.5	35877	0.03
	1	34292	0.20
	2	31068	0.45
	10	22366	0.74
	20	23987	0.67
30000	0.2	40744	0.04
	0.3	39398	0.02
	0.5	38679	0.03
	1	38830	0.04
	2	37116	0.09
	10	27340	0.24
	20	21349	0.40

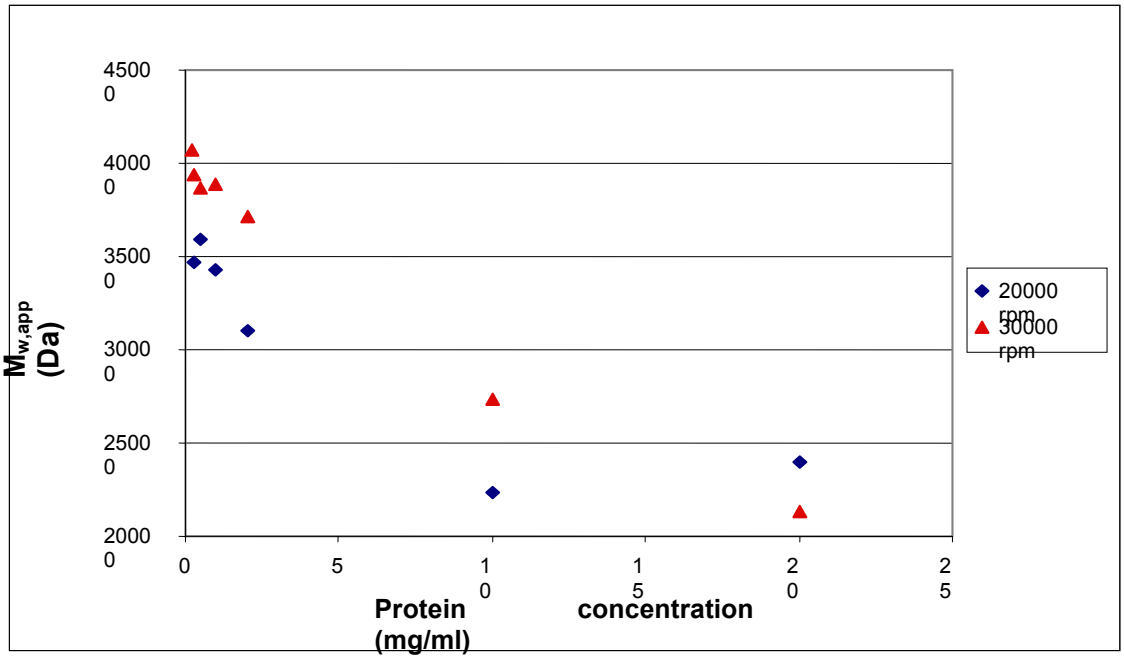

Figure 4-5. Plot of $M_{w,app}$ against concentration of Eg5 stalk$_{364-520}$ domain.

Data sets from both the 20000 (diamond) and 30000 (triangle) rpm runs show the same trend of decreasing $M_{w,app}$ with increasing concentrations of protein.

Table 4-3. Global $M_{w,app}$ obtained from global fitting of data sets to model.

Rotor speed (rpm)	Global $M_{w,app}$ (Da)
20000	26295
30000	28413
30000 (excluding 10 & 20 mg/ml data)	37826

4.2.2 Circular Dichroism (CD)

CD experiment was carried out to determine the secondary structure content of the Eg5 $stalk_{364-520}$ domain in 20 mM potassium dihydrogen phosphate (buffered at pH 7.0). The CD spectra obtained in the far UV region (260 – 180 nm) relates to secondary structure elements present in the sample. A maximum is observed at about 190 nm and a double minimum is observed at 208 and 222 nm (Figure 4-6). The ratio of molar ellipticity (Θ) at 222 to 208 nm is calculated to be 0.95. The data was then submitted to DichroWeb[161], an online server, for secondary structure analysis using the CONTINLL algorithm[162]. The results, presented in Table 4-4, show that the Eg5 $stalk_{364-520}$ domain contains approximately 52 % of helices and 5 % of strands.

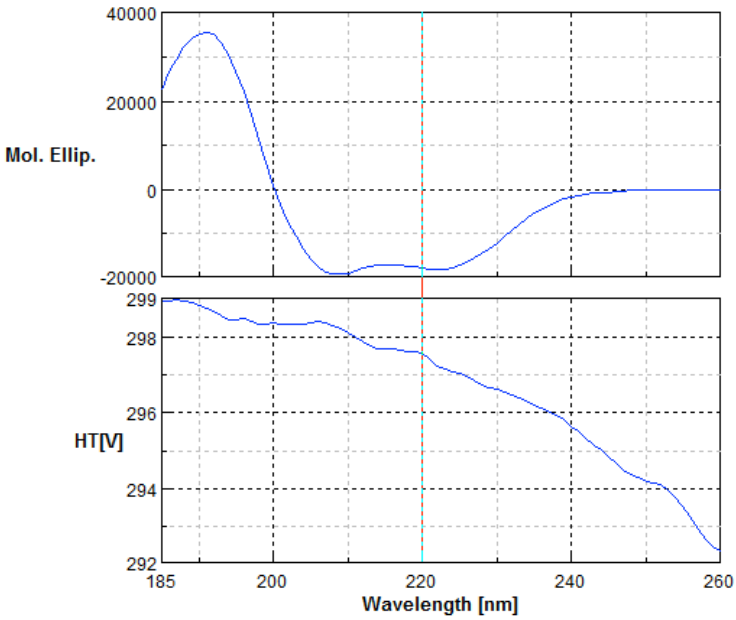

Figure 4-6. Far UV spectrum of Eg5 $stalk_{364-520}$ domain.

A maximum is observed at about 190 nm and a double minimum is observed at 208 and 222 nm.

Table 4-4. Estimates of secondary structure elements in Eg5 stalk$_{364-520}$ domain.

Protein	Helix (%)	Strand (%)	Turns (%)	Unordered (%)	Total (%)
Eg5 stalk$_{364-520}$ domain	52.2	5.2	15.3	27.3	100.0

4.2.3 Small Angle X-ray Scattering (SAXS)

In order to gain insight into the molecular shape of the Eg5 stalk$_{364-520}$ domain, SAXS was carried out on six different concentrations of the protein (19.97, 9.86, 2.14, 0.98, 0.49, 0.29 mg/ml), in 50 mM PIPES pH 6.8, 150 mM NaCl and 1 mM TCEP buffer. The data quality was examined using PRIMUS[163] and the data sets from samples with concentrations of 0.49 and 0.29 mg/ml were excluded due to aggregation and poor signal-to-noise ratio respectively. A representative scattering curve of one of the samples is shown in Figure 4-7. Based on the Guinier plot, the values of R_g and I(0) were extracted and listed in Table 4-5. These values are relatively close for all four samples of different concentrations, with the average R_g and I(0) being 4.95 and 42.49 respectively. The errors are generally small, but increases with decreasing concentration of sample.

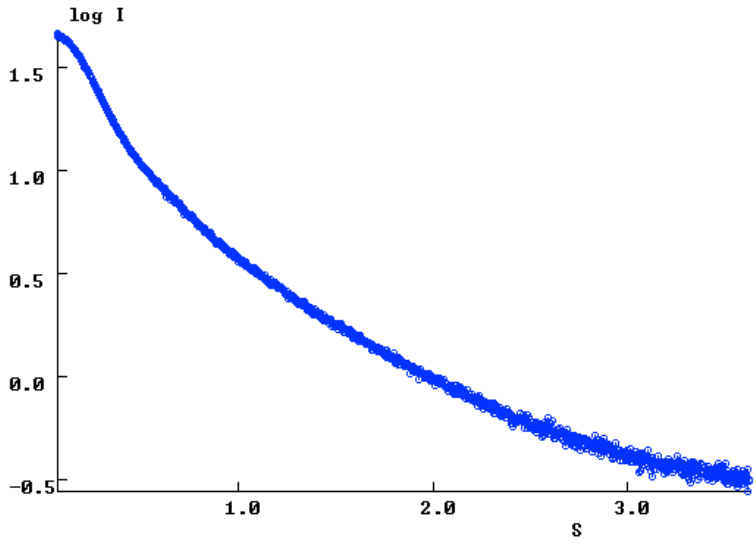

Figure 4-7. Representative scattering profile of Eg5 stalk$_{364-520}$ domain obtained from SAXS.

Scattering curve (intensity versus scattering angle) of 19.97 mg/ml of Eg5 stalk$_{364-520}$ domain reveals no aggregation and good signal-to-noise ratio.

Table 4-5. R_g and I(0) obtained from the Guinier and p(r) plots, and D_{max} for four concentrations of Eg5 stalk$_{364-520}$ domain.

Conc. (mg/ml)	Guinier plot		p(r) plot		D_{max} (nm)
	R_g (nm)	I(0)	R_g (nm)	I(0)	
19.97	5.31 ± 0.03	48.03 ± 0.19	5.64	49.05	19
9.86	5.13 ± 0.03	44.34 ± 0.23	5.74	46.69	20.5
2.14	4.67 ± 0.07	42.13 ± 0.50	5.31	44.72	19
0.98	4.67 ± 0.20	35.45 ± 1.17	5.32	37.04	18.5
Average	4.95	42.49	5.50	44.38	19.3

Next, the p(r) plots were generated using GNOM[165] and the D_{max} values of the protein samples were determined (Table 4-5). A representative p(r) plot is shown in Figure 4-8. The peak position is located at approximately 2.5 nm for all samples and the shape of the p(r) plot, which shows a roughly linear decrease with increasing r, is indicative of an elongated rod-shaped protein[178]. The D_{max} values generally agree for all four concentrations and the average is 19.3 nm. From the p(r) analysis, the R_g and I(0) values obtained were similar for all concentrations and the average R_g and I(0) are 5.50 and 44.38 respectively. The R_g and I(0) values obtained from the Guinier plot are consistently smaller than those from the p(r) function, but the differences are relatively small.

The molecular envelope of Eg5 stalk$_{364-520}$ domain was then generated by *ab initio* modelling from the scattering profile using GASBOR[166] in reciprocal space and incorporating P2 symmetry, as the protein has been shown to exist predominantly as a single dimeric species by AUC. Twenty independent simulations of each protein sample produced molecular envelopes of largely reproducible shape. Thus, DAMAVER[167] was utilised to obtain an average and filtered model. The results revealed an elongated rod-shaped molecular envelope that is approximately 165 Å long and 18 Å wide (Figure 4-9). However, it is not a straight rod-shaped molecular envelope, but one that has several kinks along its length.

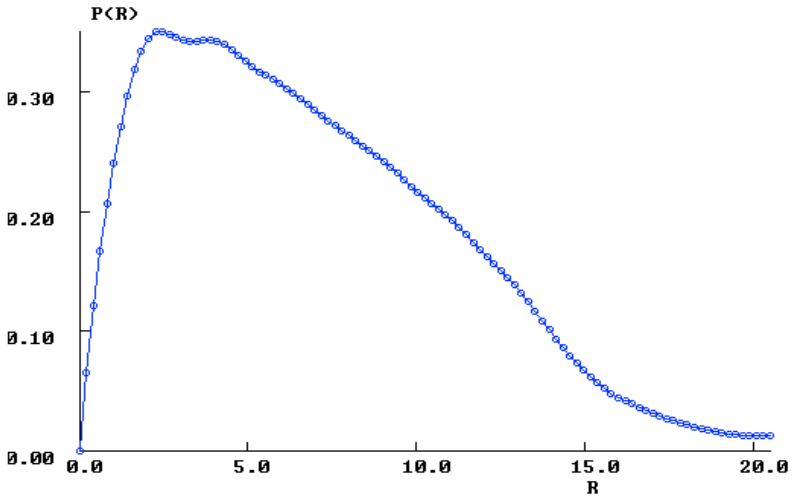

Figure 4-8. Representative p(r) plot of Eg5 stalk$_{364-520}$ domain (9.86 mg/ml).

The peak location is ~2.5 nm and the shape of the curve is indicative of a rod-shaped molecule.

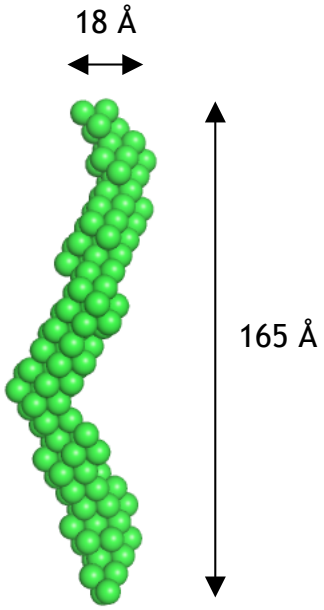

Figure 4-9. Elongated rod-shaped molecular envelope of Eg5 stalk$_{364-520}$ domain.

An averaged and filtered model of the Eg5 stalk$_{364-520}$ domain reveals a molecular envelope that is approximately 165 Å long and 18 Å wide, with several kinks along its length.

4.3 Discussion

4.3.1 Sedimentation coefficient of Eg5 stalk$_{364-520}$ domain

The SV experiments were performed for seven different concentrations of Eg5 stalk$_{364-520}$ domain, using both the interference and absorbance optics. The

individual data sets were fitted to the continuous c(s) distribution model. Going through all the size distribution c(s) profiles individually, several conclusions that are consistent for all concentrations and optical systems can be made. Firstly, only one significant peak is observed; thus, revealing that Eg5 stalk$_{364\text{-}520}$ domain exists predominantly as one species, instead of an equilibrium of several species, at all concentrations. Although the c(s) profile of the 0.3 mg/ml sample revealed a second smaller peak, the anomaly could be attributed to a contaminant or lysed sample. Based on this first conclusion, we can also confirm that there is no concentration-dependent oligomerisation effect, as the protein exists as one species at both low and high concentrations.

Secondly, the position of the single significant peak is fairly consistent and shifts gradually, from 1.2 S at low concentrations to less than 1.0 S at high concentrations. The gradual migration of the peak, which is illustrated in Figure 4-2, is most likely due to the effects of non-ideal behaviour of the protein. This occurs when the overcrowding of protein molecules at higher concentrations prevents proper packing of the molecules at the base of the cell. The proposed rod-shaped structure of the protein could further exacerbate the effects of non-ideal behaviour of the protein, which may not be as obvious in globular structures. Finally, by plotting the true sedimentation coefficient against the concentration of the protein and fitting a linear regression through the data, the $s^{\circ}_{20,w}$ of Eg5 stalk$_{364\text{-}520}$ domain is revealed to be 1.76 S. Since the goodness of fit is 0.98, this value is highly reliable.

4.3.2 Oligomerisation state of Eg5 stalk$_{364\text{-}520}$ domain

As the stalk$_{364\text{-}520}$ domain is expected to be an elongated coiled-coil structure, the use of analytical gel filtration would not be ideal for determining the molecular mass and oligomerisation state of the non-globular polypeptide. Hence, SE experiment was carried out on seven different concentrations of Eg5 stalk$_{364\text{-}520}$ domain, at two rotor speeds (20000 and 30000 rpm) using the interference optics. Based on the results obtained from the SV experiments, I tried to fit the SE data sets individually to the species analysis model, with the assumption that the Eg5 stalk$_{364\text{-}520}$ domain exists as a single dimeric species with

a calculated molecular mass of 36325 Da. Going through all the individually fitted data sets, a good fit of the data to the model is observed for the majority of data sets.

The resulting $M_{w,app}$ for each sample of different concentration consistently follows a trend: the mass decreases with increasing concentration of protein. This is most likely a consequence of concentration- and shape-dependent non-ideal behaviour of the protein, as seen in the SV experiments. The failure of the protein molecules to pack properly prevents the formation of steep concentration gradients in the cell. In addition, the $M_{w,app}$ values obtained from the SE experiment conducted at 20000 rpm is generally lower than that of the 30000 rpm run. This could be because the protein molecules have not reached a full equilibrium, that is the formation of a steep concentration gradient in the cell, at the lower speed of 20000 rpm.

Nevertheless, all $M_{w,app}$ values obtained are above the monomeric molecular mass of 18163 Da; thus, indicating that the protein does not exist as a single monomeric species. Further fitting of the data sets to the monomer-dimer, monomer-trimer and monomer-tetramer self-association models revealed poor fits, high r.m.s.d. values, and large residuals (results not shown). Together with the SV results that showed a single significant peak, we can confirm that Eg5 $stalk_{364-520}$ domain does not exist as an equilibrium of different oligomeric states. Finally, by performing a global fit of the model with data sets obtained at each rotor speed, a $M_{w,app}$ value of approximately 27 kDa was obtained. This is roughly 25 % less than the expected molecular weight of the dimeric species.

Given that some data sets do not fit very well with the model, as evident by their relatively higher r.m.s.d. values, they were excluded from the subsequent global fitting of data to the model. Consequently, the $M_{w,app}$ of Eg5 $stalk_{364-520}$ domain is approximately 37 kDa. This value is very close to the expected dimeric molecular mass of 36 kDa. The data sets that were excluded from this global fitting are mainly from samples of high protein concentrations, which are more prone to non-ideal behaviour. Hence, the low $M_{w,app}$ value obtained from the global fitting of all data sets may be accounted for by the non-ideal behaviour of the protein. In short, the SE experiment reveals that the Eg5 $stalk_{364-520}$ domain

most likely exists as a single dimeric species at both low and high concentrations.

4.3.3 Secondary structure elements in Eg5 stalk$_{364-520}$ domain

Prior to CD analysis, the Eg5 stalk$_{364-520}$ domain protein sample had to be dialysed in 20 mM potassium dihydrogen phosphate (pH 7.0). This is because both the buffers used in gel filtration and AUC contain chloride ions that absorb strongly in the far UV region, below 205 nm. The peak produced from the absorption of the buffer could overlap with the peak that relates to the secondary structure elements present; thus, interfering with analysis of the secondary structure composition of the Eg5 stalk$_{364-520}$ domain. The CD spectrum reveals a maximum at about 190 nm and a double minimum at 208 and 222 nm. In general, the shape of the CD spectrum is characteristic of α-helices.

The ratio of $\Theta_{222}/\Theta_{208}$ is telling of the presence of coiled-coil helices in the protein sample. For non-coiled helices, the typical ratio is around 0.83 and this increases to about 1.03 for coiled-coils[179]. As the $\Theta_{222}/\Theta_{208}$ ratio calculated from the CD spectra is 0.95, the Eg5 stalk$_{364-520}$ domain is neither fully coiled-coil nor entirely made up of non-coiled helices. While it tends to be closer to a coiled-coil structure, it may still contain some non-coiled regions. This finding is supported by the estimated percentage of helices (52 %) and turns and unordered regions (total of 43 %) in the protein sample. This is in contrast to the human kinesin-1 construct (residues 771-963), which revealed a higher α-helical content (~70 %) in CD analysis[180]. Thus, the results from the CD analysis point towards an interrupted coiled-coil Eg5 stalk$_{364-520}$ domain.

4.3.4 Low resolution structure of Eg5 stalk$_{364-520}$ domain in solution

As attempts to crystallise the Eg5 stalk$_{364-520}$ domain were unsuccessful, we turned to SAX to gain insights into the molecular shape of the protein in solution. The scattering profiles of the four samples of protein with different

concentrations (ranging from 1 to 20 mg/ml) are similar, which concurs with the conclusion from AUC that there is no concentration-dependent oligomerisation behaviour. The shape of the scattering curve hints at a rod-shaped molecule. D_{max} value for all four concentrations is very close and is approximately 19.3 nm. The values of R_g and I(0) obtained through the Guinier and p(r) analyses, for all four concentrations, are also highly consistent, although the values obtained from the Guinier analysis are generally lower than that of the p(r) plot.

For a protein that is predicted to be a coiled-coil structure, the values obtained using the p(r) plot is deemed more accurate than that obtained from the Guinier analysis[181]. This is because for an elongated rod-shaped protein, only a small angle region is applicable for the Guinier approximation; thus, resulting in less reliable values of R_g and I(0). On the other hand, the p(r) function, which is calculated from the overall scattering profile, is more tolerant to the limited small angle region; hence, the values obtained are deemed as reliable estimates of R_g and I(0). In short, the mean R_g and I(0) values for the Eg5 $stalk_{364-520}$ domain, obtained from the p(r) function, are 5.5 nm and 44.4 respectively.

Individual *ab initio* modelling of the molecular envelope of Eg5 $stalk_{364-520}$ domain from the scattering profiles reveal a reproducible rod-like molecular envelope that is approximately 165 Å long and 18 Å wide. To validate this structure, we compare it with the *Drosophila melanogaster* homologue that has 10 residues more than human Eg5. Electron micrographs of the rotary-shadowed fruit fly homologue revealed a bipolar kinesin that is ~956 Å in length[57]. The rod-shaped structure connecting the motor domain to tail domain has a length of ~613 Å. If the 157-residue Eg5 $stalk_{364-520}$ domain is ~165 Å in length as shown by SAXS, the entire 457-residue stalk domain would be approximately 484 Å long. This value is less than the length of the stalk domain observed in the electron micrographs of the rotary-shadowed *D. melanogaster* homologue.

However, it is important to note that the platinum coating of the rotary-shadowed protein is generally 25 Å thick; thus, making it appear larger than it actually is. Hence, the length of the molecular envelope of the Eg5 $stalk_{364-520}$ domain determined by SAXS is probably not far from its actual length. The molecular envelope also appears to contain several kinks along its length. This

could indicate an interrupted coiled-coil structure, as supported by the $\Theta_{222}/\Theta_{208}$ ratio and α-helical content from CD analysis. In short, we propose that the Eg5 stalk$_{364\text{-}520}$ domain facilitates dimerisation of the protein by forming an elongated coiled-coil structure that may be interrupted by kinks along its length (Figure 4-10).

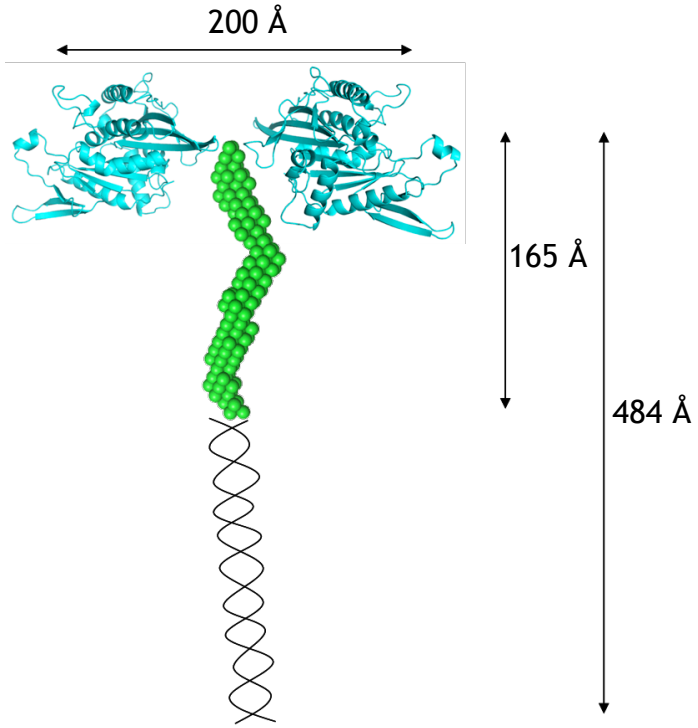

Figure 4-10. Proposed model of dimeric Eg5 motor domains linked by the stalk domains.

Two motor domains (cyan, PDB ID: 1X88[91]), spanning approximately 200 Å, are brought together by the dimerisation of the Eg5 stalk$_{364\text{-}520}$ domains (green, bead model), which is ~165 Å in length. The rest of the stalk domain has been drawn with black lines to show the length of the entire stalk domain (~ 484 Å). The Eg5 tail domain, whose structure is not known, is not shown in the diagram.

5 Autoinhibitory mechanism of kinesin-1

The results in this chapter have been published in a peer-reviewed journal:

Kaan, H.Y., Hackney, D.D. & Kozielski, F. The structure of the kinesin-1 motor-tail complex reveals the mechanism of autoinhibition. *Science* **333**, 883-5 (2011). (Appendix 4)

5.1 Aims and objectives

Kinesin-1 is a processive, plus-end directed motor that uses energy from ATP hydrolysis to carry out various functions, including cargo transport along axons, and transport of organelles along microtubules. It is widely accepted that dimeric kinesin-1 moves along microtubules in a 'hand-over-hand' manner. However, the exact details of its motility remain unclear. On the other hand, when kinesin-1 is not transporting cargo along the microtubule track, it has to be regulated to prevent squandering of ATP and overcrowding of the microtubule highway. The tail domain has been implicated in an autoinhibitory mechanism that keeps the kinesin in a compact, folded and inactive conformation in the absence of cargo. Several models of autoinhibition have been proposed, including steric and allosteric inhibition; however, there are no high resolution structures available to validate the proposed models.

In this chapter, I will report the crystal structures of kinesin-1 motor domain dimer alone and in complex with the tail domain, to 2.7 Å and 2.2 Å respectively. The structure of the motor domain dimer serves as additional structural information for docking onto cryo-EM maps of microtubules decorated with kinesins and for modelling of kinesin-1 motility. It will also serve as a comparison for the dimer-tail structure, in order to tease out the conformational changes that occur when kinesin-1 is autoinhibited. The dimer-tail structure will be complemented with a peptide array assay to reveal important residues involved in the binding of the tail to the motor domain. Lastly, together with results from single turnover experiments conducted by our collaborator, we will propose a novel model for the autoinhibition mechanism of kinesin-1.

5.2 Results

5.2.1 Structure of the kinesin-1 motor domain dimer

The crystal structure of *D. melanogaster* kinesin-1 motor domain dimer was solved at a resolution of 2.7 Å. Data collection and refinement statistics are shown in Table 5-1. The final model comprises of residues Glu10 to Lys356 (excluding residues 246 to 258) and Glu10 to Lys354 (excluding residues 244 to 259) for molecules A and B respectively. The excluded region is loop L11, which is disordered and not modelled. The asymmetric unit consists of a dimer, where the monomers are not related by crystallographic symmetry. Each monomer has one molecule of Mg^{2+}ADP bound in the nucleotide-binding site.

The motor domains of the dimer have the same fold as other kinesin-1 homologues: eight major ß-strands in the core, surrounded by three major α-helices on each side. Overall, the two monomers are related by a non-crystallographic two-fold symmetry (180°) and interact mainly at the coiled-coil domain via the neck linker (Figure 5-1). Four residues in the catalytic core are shown to contribute to the interfacial surface with the coiled-coil domain: Asn167 and Arg168 of molecule B and Lys166 of both molecules A and B. The two monomers of the kinesin-1 dimer overlay very well in the catalytic core up to the neck linker, but differ slightly in the position of the α-helix forming the coiled-coil domain (r.m.s.d. = 0.84).

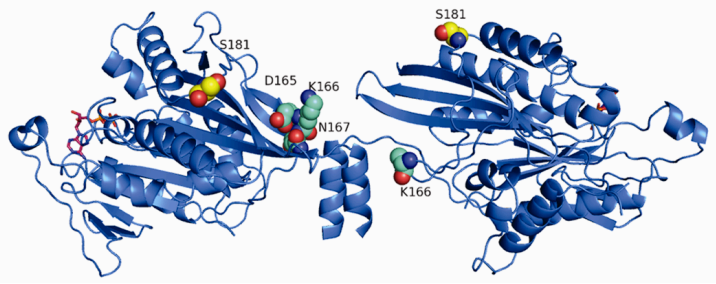

Figure 5-1. Crystal structure of kinesin-1 motor domain dimer.

D. melanogaster kinesin motor domain dimer with Mg^{2+}ADP (red, sticks) bound in the nucleotide-binding pocket. Ser181 (yellow, spheres), will be modified to cysteine for cross-linking experiments, and catalytic core residues (green, spheres) interacting with the coiled-coil domain are shown.

Table 5-1. Data collection and refinement statistics for kinesin-1 motor domain dimer and dimer-tail complex.

	Dimer	Dimer-tail
Unit cell dimensions a, b, c, β (Å, °)	76.9, 89.2, 138.4, 90.0	113.8, 190.7, 146.0, 90.0
Space group	$P2_12_12_1$	$C222_1$
Beamline / Detector	ID23-2 / Q315R	PXI / Pilatus 6M
Molecules per asymmetric unit	2	4
Resolution range (Å)	30.0 - 2.7	30.0 - 2.2
No. of unique reflections	35890	80517
Completeness (%)	99.9 (100.0) [b]	99.9 (99.6)
Multiplicity	4.1 (4.1)	8.8 (8.3)
R_{sym} (%)	8.3 (39.5)	5.7 (36.6)
I/σ(I)	12.0 (3.6)	21.7 (5.5)
Wilson B ($Å^2$)	55.87	41.38
Refinement statistics		
R_{work} / R_{free} (%)	21.0 / 28.9	19.5 / 25.2
Average B Factors		
Protein	41.3	43.1
Ligand and ions / Water	30.0 / 35.5	28.9 / 43.0
No. of Mg^{2+}ADP / Water	2 / 181	4 / 656
r.m.s.d. [c] in bond length (Å)	0.012	0.012
r.m.s.d. in bond angle (°)	1.82	1.79

[a] Values in parentheses pertain to the highest resolution shell.

[b] r.m.s.d. is the root-mean-square deviation from ideal geometry.

5.2.2 Structure of the kinesin-1 motor domain dimer-tail complex

We have solved the first crystal structure of a kinesin motor domain dimer in complex with the tail domain at a resolution of 2.2 Å (Figure 5-2a). Data collection and refinement statistics are shown in Table 5-1. The asymmetric unit comprises of four molecules of the kinesin-1 motor domain, with two molecules (chains C and D) forming a dimer via interactions of the coiled-coil domains and the other two molecules (chains A and B) forming dimers with their symmetry-related molecules (A' and B' respectively). Each monomer has one molecule of Mg^{2+}ADP bound in the nucleotide-binding site. The motor domains in the dimer-tail complex share many similarities with that of the kinesin-1 dimer structure described above. First, they exhibit the same fold. Second, the catalytic core of the motor domains in the free dimer and dimer-tail complex overlay very well, only differing in the positions of the neck linker and α-helix forming the coiled-coil domain (mean r.m.s.d. = 0.765) (Figure 5-2b). Third, the motor domain dimer of both structures exhibit a two-fold symmetry.

The major difference between the dimer-tail complex and the dimer structure is the global conformation of the two monomers forming the dimer, due to the binding of the tail domain. Each motor domain dimer is complexed with a monomeric tail domain and the final model of the tail domain comprises of residues Gln939 to Ser948, with the rest of the tail domain being disordered and not modelled. The 10-residue tail peptide has an extended and linear conformation, which resembles a ß-strand. Owing to its amino acid sequence, the peptide is almost symmetrical, in terms of side chain properties, about the Lys944 residue. This distinctive feature of the tail peptide allows it to bind in two directions between the motor domain dimer, which also exhibits a two-fold symmetry (Figure 5-2c and d). As such, we observe pseudosymmetry in the crystal structure and the tail domains binding to the AA' and BB' dimers lie on the two-fold symmetry axis. The tail peptide binds simultaneously to ß4 of both motor domains in the dimer and the total buried surface area between the dimer and the tail domain is approximately 1000 $Å^2$.

The crystal structure of the motor domain dimer-tail complex has given us an insight into the dimer-tail interface. Taking a closer look at the dimer-tail

interface, hydrogen bond interactions between the main chain carbonyl and amino groups of the tail domain and the N-terminal of the ß4 strand of each motor domain are observed (Figure 5-3). Consequently, the 10-residue tail peptide, with its extended and linear conformation, may be seen as an extension of the eight-stranded ß-sheet of the monomeric motor domain. Besides the hydrogen bond interactions that are characteristic of a ß-sheet, hydrophobic interactions between Ile942, Ile946 of the tail domain and Phe123, Ile126, and Phe135 of each motor domain are observed. In addition, a C—H--π interaction between the pyrrolidine ring of Pro945 and Phe179 is observed. Finally, the His136 side chains of each motor domain are in close proximity in the interface (~2.9 Å) (Figure 5-4).

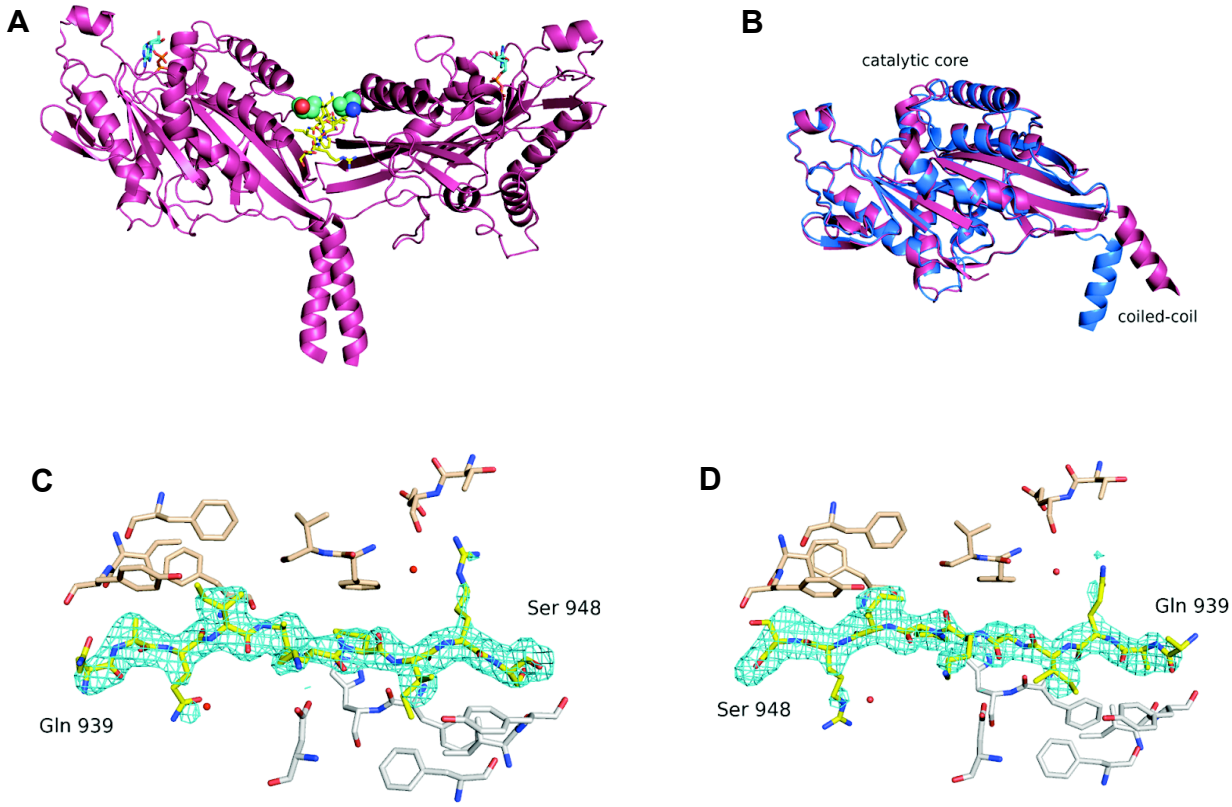

Figure 5-2. Overall structure of kinesin-1 motor domain dimer-tail complex.

(A) *D. melanogaster* kinesin-1 motor domain dimer complexed with tail domain (yellow). Cyan sticks: Mg^{2+}ADP; green spheres: Ser 181. **(B)** Overlay of a monomer of the dimer structure (blue) with that of the dimer-tail complex (magenta), revealing differing positions of the α-helix forming the coiled-coil domain. **(C)** Dimer-tail interface showing residues of motor domain (chain A: grey, B: beige), tail domain (yellow) and omit map (F_o-F_c) (contoured at σ=3.00). The tail domain binds in one direction with residue Gln939 on the left and Ser948 on the right, and fits well into the electron density. **(D)** The tail domain is seen binding in the opposite direction with Ser948 on the left and Gln939 on the right, but it still fits well into the electron density map.

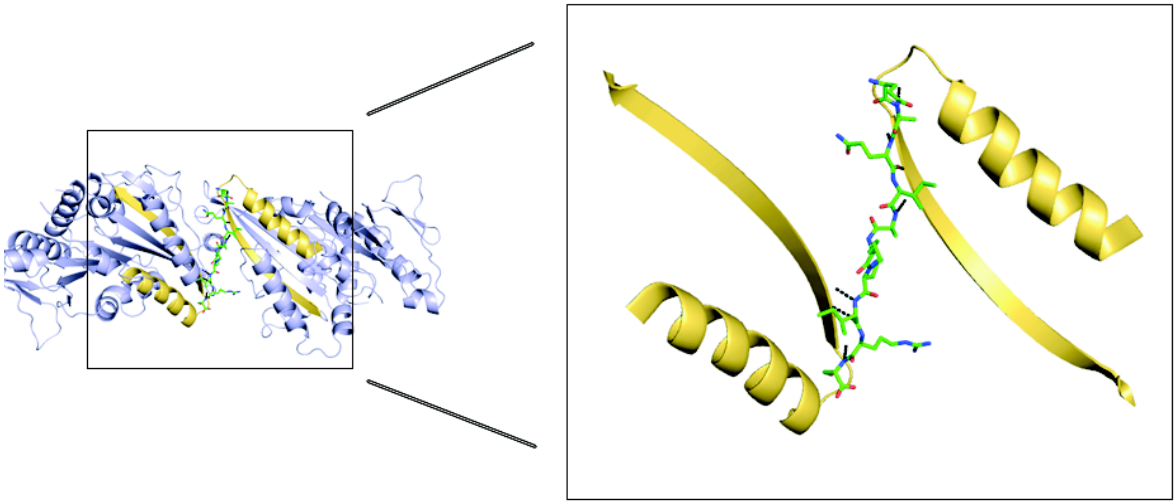

Figure 5-3. Motor domain dimer-tail interface.

The tail domain and its interactions with the motor domain shown as an enlarged inset. The motor domain dimer (grey, left) is viewed from the top of Figure 5-2a and downwards onto the start of the α-helix forming the coiled-coil domain. The hydrogen bond interactions (dotted lines, right), between the tail domain (green) and the N-terminal of the β4 strand of each motor domain, are characteristic of a β-sheet.

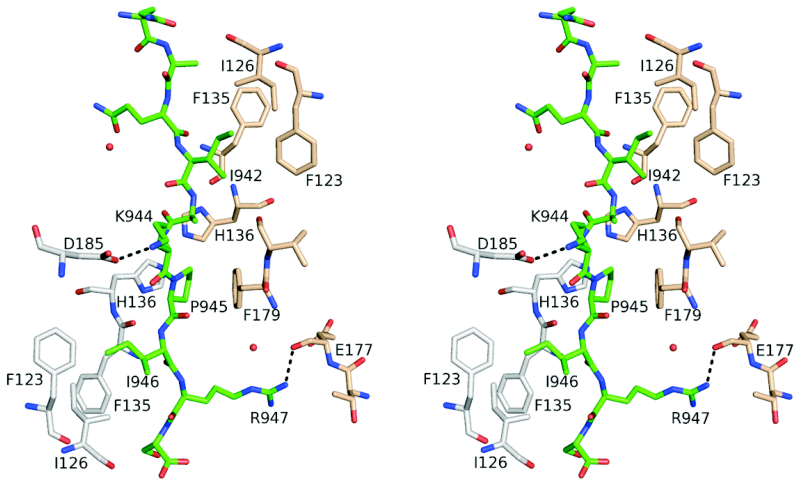

Figure 5-4. Residues involved in the binding of the tail to the motor domains.

Stereoplot showing C—H---π and hydrogen bond interactions (dotted lines) between the tail (green) and motor domains (chain A: grey, chain B: beige). His136 side chains of each motor domain are in close proximity in the interface (~2.9 Å).

5.2.3 Peptide array

To determine which residues in the tail peptide are crucial for binding to the motor domain, I did a single alanine-scan peptide array study, where each residue of the tail peptide is mutated to an alanine in turn. The results revealed that when Lys944 and Arg947 are mutated to alanine, the binding of the tail to motor domains is abolished (Figure 5-5). Double and triple alanine-scan peptide array, where two and three residues of the tail peptide are mutated to alanines in turn respectively, were also used to confirm the results. All experiments performed in duplicates revealed the same result, which confirms undoubtedly that Lys944 and Arg947 are the two crucial residues that allow the tail to bind to the motor domains.

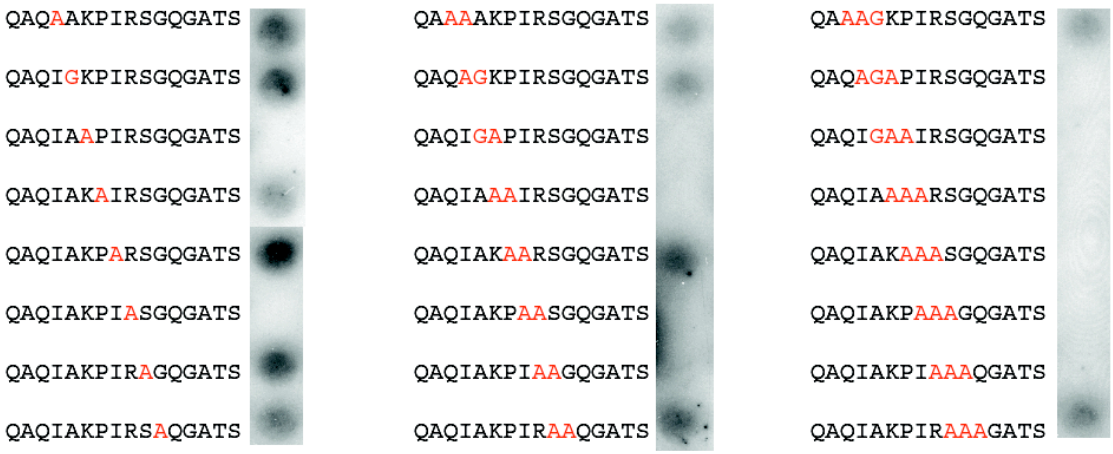

Figure 5-5. Single, double and triple alanine-scan peptide arrays reveal crucial residues involved in dimer-tail binding.

Single (left), double (middle) and triple (right) alanine-scan peptide arrays, with the native peptide sequence in black and mutated residues in red.

5.3 Discussion

5.3.1 Docking of kinesin-1 motor domain dimer on microtubules

In order to study how kinesins move along microtubule tracks, several groups have produced cryo-EM maps and three-dimensional image reconstructions of microtubules decorated with kinesin monomers or dimers, with different

nucleotides bound, to create static images of kinesins frozen in each step of the processive motion[127,128,182-184]. Here, I overlay the monomers of the kinesin-1 dimer structure with the human monomeric kinesin-1 structure docked into the highest resolution cryo-EM map obtained thus far (9 Å, PDB ID: 2P4N)[184]. The least squares fit (LSQ) superpose method was used to overlay helix α4 of each monomer of the dimer structure with that of the human monomeric kinesin-1 structure, because this motif is conserved and forms the main interactions with the tubulin heterodimer[185]. For both overlays, the second unattached motor domain points toward the direction of movement (plus end); however, helix α2 of the second motor domain inadvertently clashes with α-tubulin (Figure 5-6), indicating that the dimer structure is not compatible with its binding to microtubules in this conformation.

Nevertheless, the unsuccessful docking of the kinesin-1 dimer structure onto microtubules should not come as a surprise. This is because the cryo-EM map shows microtubules decorated with kinesin monomers; thus it may not reflect the exact conformation of the kinesin dimer bound to microtubules. Moreover, if the asymmetric 'hand-over-hand' model holds true for kinesin motility, the conformation of each motor at the end of a step would be different from the conformation at the beginning of the step. Since the cryo-EM map only shows one conformation of the bound kinesin monomer, we are missing crucial details of the other conformation, which may be applicable for the docking of the kinesin-1 dimer structure onto the cryo-EM map.

Lastly, the crystal structure with Mg^{2+}ADP bound in both motor domains does not reflect the alternating head catalysis model of microtubule-stimulated ATP hydrolysis[186], whereby each motor domain of the dimer undergoes ATP hydrolysis in turn, while the other retains a tightly-bound ADP during processive movement. According to the model, Mg^{2+}ADP bound kinesin represents either a detached or a weakly-bound state of kinesin[187]. By trying to dock the dimer structure onto the map, we are assuming that the attached monomer is either in the 'initial' weakly-bound state after binding to a new tubulin site, or in the 'final' weakly-bound state just before detachment. Consequently, the crystal structure of the kinesin-1 dimer provides a new conformation for modelling the mechanism of motility, but does not provide sufficient information to explain it.

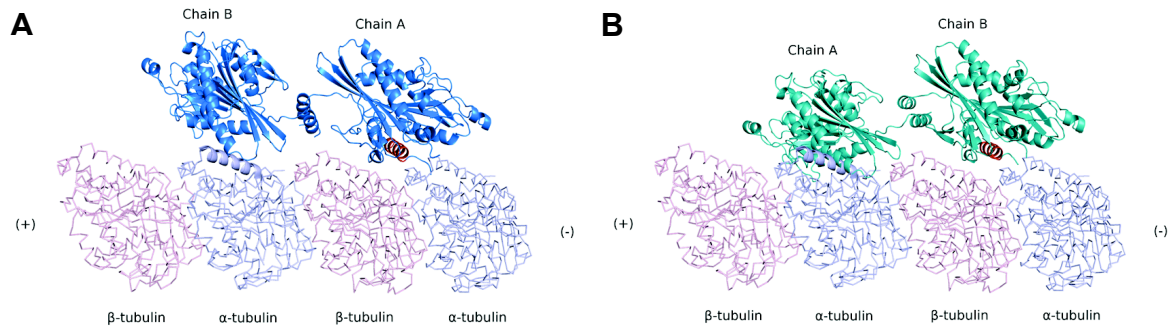

Figure 5-6. Docking of kinesin-1 dimer structure onto cryo-EM map.

Kinesin-1 dimer structure docked onto cryo-EM map of kinesin-tubulin complex (PDB ID: 2P4N)[184], by overlaying helix α4 (red) of **(A)** chain A and **(B)** chain B of the dimer with that of human monomeric kinesin, reveals clash of helix α2 with α-tubulin.

5.3.2 Covalent mimic of tail-inhibited kinesin-1

Comparison of the dimer and dimer-tail structures reveals a global conformational change of the dimer. Binding of the tail domain to the motor domains bring the latter closer together, such that the motor domain dimer no longer forms a T-shape, but resembles an inverted umbrella (Figure 5-7). The distance between the Cα atoms of Phe179 of both motor domains was approximately 48 Å in the dimer structure, but decreased to 10 Å upon binding of the tail domain. Similarly, the angle between ß7 of both motor domains was about 180° in the dimer structure, but decreased to about 100° upon binding of the tail domain.

To mimic inhibition of kinesin-1 by the tail domain, our collaborator (Prof. David Hackney, Carnegie Mellon University) introduced a covalent cross-link between the motor domains at the tail interface. Ser181 residues in the two motor domains (Figure 5-1) were substituted with cysteine in a background with the other reactive cyteines removed. A covalent cross-link between them could be readily formed by oxidation to a disulfide and reversed by reduction with DTT (Figure 5-8a). In this preparation, about 10 % of the motor domain monomers were refractory to cross-linking, as determined by densitometry of stained SDS gel samples. Microtubule-stimulated ATPase activity was lost and regained in parallel with the extent of cross-linking, indicating that cross-linking strongly inhibits hydrolysis (Figure 5-8b).

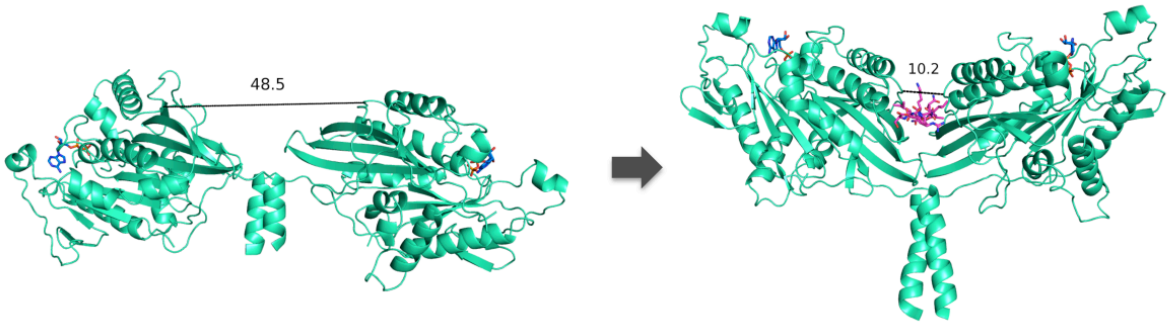

Figure 5-7. Global conformational change of kinesin-1 dimer upon tail-binding.

Binding of tail domain (magenta) brings motor domains (green) closer together, such that the motor domain dimer no longer forms a T-shape, but resembles an inverted umbrella. The distance between Cα of Phe179 decreases from 48.5 to 10.2 Å and the angle between β7 of motor domains decreases from 180° to about 100° upon tail binding. ADP in the nucleotide pockets are represented by blue ball-and-stick models.

A

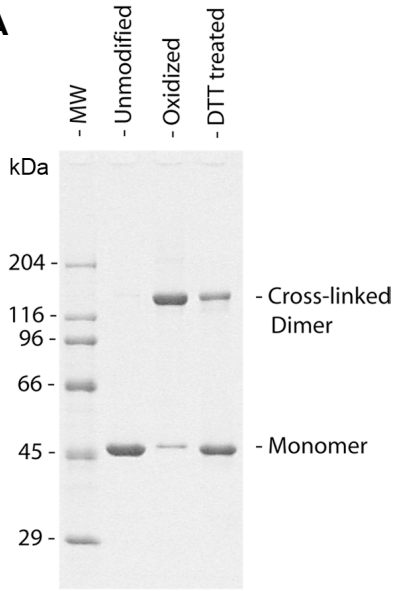

B

	MT-ATPase (Relative)	[Monomer] (Relative to unmodified)
Unmodified	100.0 ± 2.4	100.0 ± 1.8
Oxidized	9.5 ± 1.2	10.6 ± 0.5
DTT-treated	74.5 ± 1.9	70.1 ± 0.4

Figure 5-8. Influence of cross-linking on microtubule-stimulated ATPase activity.

(A) The amount of cross-linked dimer and uncross-linked monomer, remaining in the oxidised and DTT-treated samples, were visualised and determined by densitometry of stained SDS gel samples (reducing agents were not used in the running of the gel). **(B)** The concentration of monomer in each preparation is indicated as a value relative to that of the unmodified sample (100 %). Microtubule-stimulated ATPase assay was performed as previously described[133] at 25°C, and in duplicate or greater with the standard deviation indicated. The activity of each preparation is indicated as a value relative to that of the unmodified sample (100 %).

Single turnover experiments were then carried out by Prof. Hackney to allow direct evaluation of the high extent of inhibition of the cross-linked fraction (Figure 5-9a). In this experiment, a dimer with S181C substitutions was equilibrated with the fluorescent ADP analogue mant-ADP before oxidation. Mant-ADP is released from kinesin with kinetics similar to those of unmodified ADP and gives a fluorescence decrease[188]. In the absence of microtubules, ADP release from the uncross-linked dimer is slow (red trace) and is further decreased when the dimer is cross-linked (blue trace). Microtubules greatly accelerate the rate of mant-ADP release from uncross-linked dimers (black trace), but produces a biphasic transient with cross-linked dimers (green trace).

In the biphasic curve, the amplitude of the fast phase is small and similar to the active fraction that is refractory to cross-linking in this preparation (Figure 5-9b). However, the majority of the cross-linked preparation exhibits no stimulation of mant-ADP release by microtubules, as can be seen by the slow phase of the green trace, which is approximately parallel to the blue trace (very slow ADP release from cross-linked dimer in the absence of microtubules). Partial reversal of cross-linking by DTT (orange trace) restores the amplitude of the fast phase in parallel to regain of uncross-linked protein (Figure 5-9b). In short, the covalent cross-link, which mimics the tail-inhibited kinesin-1 dimer, prevents ADP release from the motor domains.

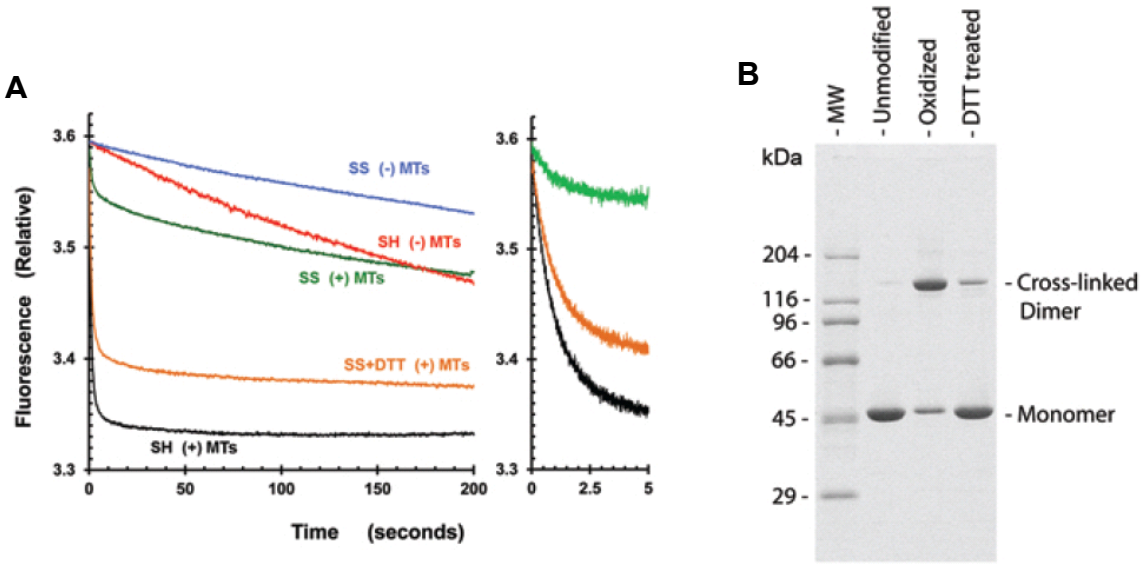

Figure 5-9. Covalent mimic in single turnover mant-ADP experiment.

(A) Release of mant-ADP from unmodified (SH), oxidised (SS) and DTT treated (SS + DTT) species after mixing with a chase of excess unlabeled ATP, with and without microtubules (MTs). **(B)** Samples were analyzed by denaturing SDS-PAGE in the absence of reducing agents.

5.3.3 Proposed autoinhibition mechanism of kinesin-1

Several models for the mechanism of inhibition by the tail domain are eliminated by the structure of the dimer-tail complex. Firstly, the tail domain does not bind to the microtubule-binding site (helix α4-loop L12-helix α5) of the motor domain and the microtubule-binding sites on the motor domains of the complex are fully exposed (Figure 5-10). Hence, the tail domain cannot cause steric interference with microtubule binding. Next, it does not bind to the neck linker or coiled-coil domain, so it cannot prevent the 'power stroke' or interfere with coordination of the coiled-coil domain to inhibit movement. Thirdly, the binding site for the tail domain is on the opposite side of the motor domain from the nucleotide-binding site; thus, ruling out models in which the tail sterically blocks the release of ADP or interacts with switch I or switch II[137] that play critical roles in coupling conformational changes to nucleotide binding[189].

Finally, binding of the tail to the motor domains also does not cause conformational changes in the catalytic core of the motor domain. The structural similarity between the catalytic core of the free motor domain dimer and the dimer-tail complex (Figure 5-2b) argues against an allosteric model proposed by Dietrich *et al*.[137]. They published an 8 Å cryo-EM map of the kinesin-1 monomer-tail-microtubule complex, which shows the tail domain binding simultaneously to the microtubule and to switch I of the motor domain[137]. Accordingly, they deduced that the binding of the tail to the motor domain induces a conformational change that prevents the release of ADP; hence, the motor domain is halted in an ADP state on the microtubule track.

However, the lack of agreement between their results and ours can be attributed to the fact that they photochemically cross-linked the tail to the motor domain by modifying and derivatising cysteine residues in the motor domain with benzophenone. They did not test any residues in the motor-tail interface as revealed by the crystal structure and the observed cross-linking of modified cysteines to the motor domain could be due to flexibility. Therefore, the high resolution crystal structure of the motor domain dimer in complex with the tail refutes the allosteric model of autoinhibition, while providing us with structural evidence for a novel mechanism of autoinhibition.

From the crystal structures of the dimer and dimer-tail complex, we identified one significant difference between the free dimer and the tail-inhibited dimer: the relative movement of the two motor domains is highly restricted in the latter because the motor domains are cross-linked at two positions: coiled-coil and tail interface. In the absence of tail binding, the motor domains likely have considerable freedom of movement, as evident from the different orientation of the *Rattus norvegicus* dimer structure[115] (Figure 1-21, PDB ID: 3KIN) as compared to our dimer structure. In the dimer-tail complex, however, the 'double lockdown' at both the neck coil and the tail interface freezes out major relative movements of the motor domains. This could prevent the undocking of the neck linker and the overlying N-terminal strand[190].

The undocking of the neck linker has been hypothesised and shown to be linked to hydrolysis and release of ADP[18,191]. Coupling of neck linker undocking and ADP release is also supported by a study, which showed that the introduction of a cross-link between the neck linker and core motor domain inhibits ADP release[192]. Conequently, the dimer-tail crystal structure and the covalent mimic of tail-inhibited dimer suggests that the observed inhibition of ADP release could be due to blocking of neck linker undocking through a double lockdown mechanism. In short, we propose a double lockdown autoinhibition mechanism, whereby cross-linking at both the coiled-coil and tail interface prevents the movement of the motor domains that is needed to undock the neck linker and release ADP (Figure 5-11). This opens up the possibility that other kinesins may be regulated by a common autoinhibitory mechanism.

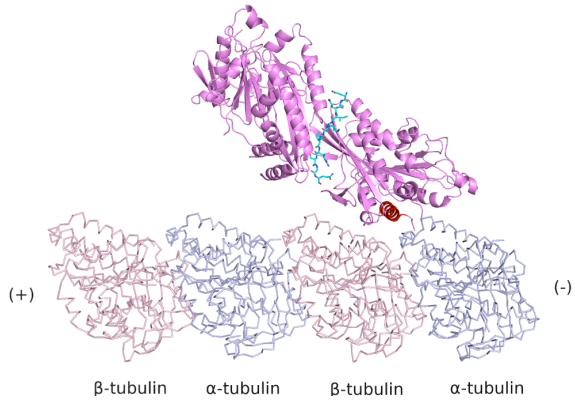

Figure 5-10. Docking of the kinesin-1 dimer-tail structure onto cryo-EM map.

The tail domain does not cause steric hindrance at the microtubule-binding site of the motor domains (helix α4 colored in red). (PDB ID: 2P4N)[184].

Our proposed model sufficiently explains and confirms the half-site inhibition stoichiometry (one monomeric tail binds to one motor domain dimer) and that dimerisation of the motor domains is required for tight binding of the tail domain[133]. Nevertheless, it is inadequate in explaining the role of the other tail domain. We speculate that when one monomeric tail domain binds to the dimeric motor domains in an inhibitory manner, the other tail domain could interact with the microtubule and immobilise the kinesin on the track while waiting for cargo to arrive. Alternatively, the second tail domain could interact with a kinesin-associated protein, such as UNC-76, which could further regulate cargo-binding and transport abilities of kinesin-1[28].

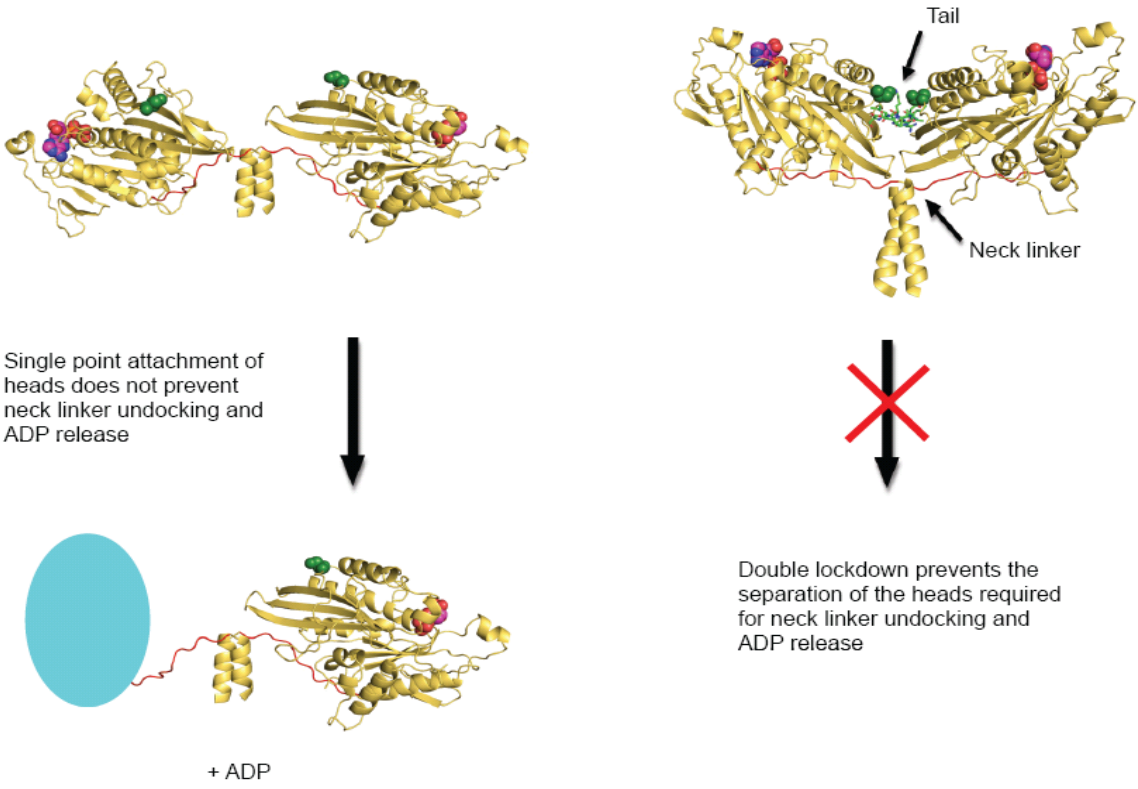

Figure 5-11. Proposed model for double lockdown mechanism of autoinhibition.

In the absence of tail (green, sticks) binding, the motor domains (yellow, cartoon) have considerable freedom of movement for neck linker (red) undocking and ADP (red, spheres) release. Cyan oval represents nucleotide-free motor domain with neck-linker undocked. However, when the tail binds, the motor domains are also cross-linked at the tail interface. This double lockdown mechanism prevents the separation of the motor domains, which is required for neck linker undocking and ADP release. Ser181 residues (green) are far apart in the free dimer but close together in the dimer-tail complex, and are on opposite sides of the tail interface.

5.3.4 Important residues involved in motor-tail interaction

The crystal structure of the motor domain dimer-tail complex not only provides us with a new model for the autoinhibitory mechanism of kinesin-1, it also reveals the important residues involved in motor-tail binding. In support of the crystal structure, the alanine-scan peptide array confirms that Lys944 and Arg947 of the tail domain are two crucial residues involved in the binding of the tail to the motor domains. Additional support for the structure in the form of mutagenesis studies was provided by Prof. Hackney. Analysis of the motor-tail interface reveals that Asp185 of the motor domain directly interacts with Lys944 of the tail region and the His136 side chains of each motor domain are in close proximity in the interface (~2.9 Å) (Figure 5-4). Hence, mutations of the Asp185 and His136 residues of the motor domain should abolish binding.

These positions are far removed from the nucleotide-binding pocket and the microtubule-binding surface. Microtubule-stimulated single turnover assay was carried out to show that the D185R and H136E substitutions do not affect the normal ATPase function of the motor domain (Table 5-1). However, upon interaction with the tail domain, both D185R and H136E mutated motor domain dimers were not significantly inhibited by the tail domain, instead the basal ATPase activity was preserved (Figure 5-12). In conclusion, structural and biochemical evidences reveal that Lys944 and Arg947 of the tail and Asp185 and His136 of the motor are essential residues involved in the binding of the tail to the motor domain dimer, in order to keep the latter in an inactive conformation.

Table 5-1. Microtubule-stimulated mant-ADP release rates of wild-type and mutant motor domains.

Construct	Rate ($\mu M^{-1}s^{-1}$)
Wild-type	11.6 ± 0.9
H136E	11.8 ± 0.5
[a] CLM-S156C	10.4 ± 0.7
CLM-S156C-D185R	11.6 ± 0.9

[a] CLM is 'Cys-lite mutant'

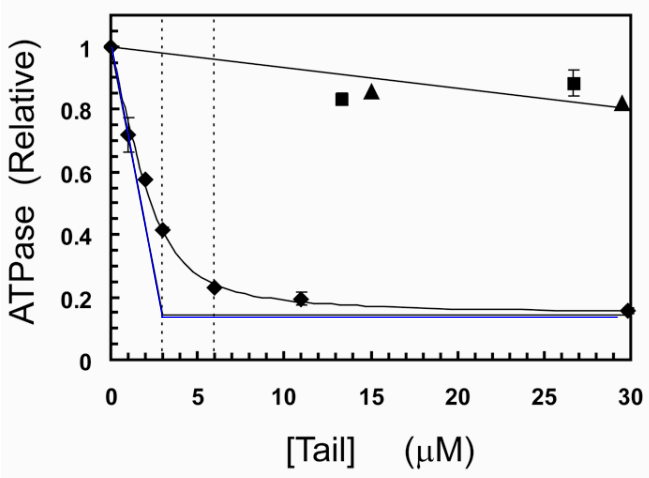

Figure 5-12. Influence of the tail domain on basal ATPase activity of wild-type and mutant motor domains.

Blue profile: wild-type; diamonds: CLM-S156C; triangles: H136E; squares: CLM-S156C-D185R.

6 Summary and future directions

6.1 Summary

6.1.1 Mitotic kinesin Eg5 and its inhibitors

The structures of Eg5 in complex with enastron, dimethylenastron, fluorastrol, STLC, compounds **6**, **7**, **8** and **9** have been solved separately. They provide information for structure-activity relationship (SAR) studies and future structure-guided drug design. The crystal structures of Eg5 in complex with enastron, dimethylenastron and fluorastrol reveal the main reasons for increased potency of these inhibitors as compared to monastrol: namely the better fit of the ligand to the allosteric binding site for enastron and dimethylenastron and the addition of two fluorine atoms for fluorastrol. The structures also show that monastrol, enastron and dimethylenastron belong to class I DHPM inhibitors that bind in the *S* configuration, whereas fluorastrol is a class II DHPM inhibitor that binds preferentially in the *R* configuration.

In the Eg5-STLC structure, the three phenyl rings are buried in the allosteric site and form hydrophobic interactions with the residues in the inhibitor-binding pocket. On the other hand, the cysteine moiety is exposed to the solvent and forms hydrogen bond interactions with Eg5 residues. This binding conformation is observed in and further confirmed by the structures of Eg5 in complex with STLC analogues **6** to **9**. In the structure of Eg5 in complex with **6**, which has one of the phenyl rings substituted by an alkyl chain, the substituent points towards the solvent-exposed region of the protein. The reason for the slight decrease in potency of compound **6** as compared to STLC is attributed to the loss of a π-π interaction, due to the substitution of the phenyl ring by an alkyl chain.

Compound **7**, which has a *meta*-substituted methyl group on one of its phenyl rings, is 15 times more potent than STLC. The crystal structure of the complex reveals that the small lipophilic substituent sits in a complementary hydrophobic sub-pocket and improves the potency of the inhibitor. The structure of Eg5 with compound **8**, which has a *meta*-substituted acetate group on one of its phenyl rings, also shows that the substituent sits in the same hydrophobic sub-pocket.

However, as it lacks the carboxylic acid group in its amine tail, it is about 15 times less potent than **7**, due to the loss of hydrogen bonds and lack of rigidity.

Finally, compound **9** also lacks the carboxylic acid in its amine tail, but it has *meta*-substitutions on two phenyl rings that greatly improve its potency. From the crystal structure, it can be seen that the lipophilic substituent (ethyl group) is positioned in the same hydrophobic sub-pocket as that of **7** and **8**, while the second *meta*-substituent (hydroxyl group) sits in a different sub-pocket in the core of the protein, similar to the position of the hydroxylphenyl group in monastrol and its analogues. In short, the crystal structures of Eg5-inhibitor complexes reveal important interactions between the ligands and protein, the preferential binding conformations of the ligands and the positions of substituents in the inhibitor-binding pocket.

The structure of Eg5-STLC revealed an intermediate state, which by comparison with the native and final inhibitor-bound structures, allows one to dissect the pathway of structural changes that occur upon inhibitor binding. Based on the crystal structures and in agreement with spectroscopic data[92], we propose that the binding of STLC to Eg5 causes drug-induced structural changes in 3 steps: first, loop L5 swings downwards to close the inhibitor-binding pocket, which then translates to an upward shift of the switch II cluster toward the N-terminal of helix α4, and finally the neck linker docks onto the motor domain. Therefore, the Eg5-STLC structure provides structural evidence for the molecular mechanism of inhibition of Eg5.

Finally, ITC experiment was carried out to obtain thermodynamic parameters of the binding event of STLC to Eg5. A 1:1 binding stoichiometry was determined, which concurs with the crystal structure of the Eg5-STLC complex. The dissociation constant is 0.096 μM, which is 50 times larger than that for Eg5-ispinesib. This alludes to the fact that the binding of ispinesib to Eg5 is tighter than that of Eg5-STLC. The enthalpy change is negative and favourable, while the entropy change is negative and unfavourable for the binding of STLC to Eg5. Taken together, the structural information and thermodynamic parameters obtained help us to gain a better understanding of the binding event of Eg5 and its inhibitor.

6.1.2 Mitotic kinesin Eg5 stalk$_{364-520}$ domain

Characterisation of the Eg5 stalk$_{364-520}$ domain by analytical ultracentrifugation (AUC) provides insights into the oligomerisation state of the protein. From the sedimentation velocity (SV) experiment, only one significant peak is observed; thus, indicating that Eg5 stalk$_{364-520}$ domain exists predominantly as one species at both low and high concentrations. This also suggests that there is no concentration-dependent oligomerisation effect. The true sedimentation coefficient at 20°C and in water, at zero concentration ($s^{\circ}_{20,w}$) of the Eg5 stalk$_{364-520}$ domain was calculated to be 1.76 S. This value is highly reliable as the fitting of a linear regression through the data produced a goodness of fit that is approximately 1.

From the sedimentation equilibrium (SE) experiment and the global fitting of the data to the species analysis model, the apparent weight averaged molecule weight ($M_{w,app}$) was found to be approximately 27 kDa. This is larger than the expected monomeric molecular weight of the protein, but less than the expected dimeric molecular weight. Hence, by exclusion of data with high r.m.s.d. values and subsequent global fitting, the $M_{w,app}$ of Eg5 stalk$_{364-520}$ domain was found to be approximately 37 kDa. This value is very close to the expected dimeric molecular mass of 36 kDa. In short, the SE experiment reveals that the Eg5 stalk$_{364-520}$ domain most likely exists as a single dimeric species at both low and high concentrations.

Next, a circular dichroism (CD) analysis was carried out for the Eg5 stalk$_{364-520}$ domain. The CD spectrum revealed a maximum at about 190 nm and a double minimum at 208 and 222 nm. In general, the shape of the CD spectrum is characteristic of α-helices. The $\Theta_{222}/\Theta_{208}$ ratio was calculated to be 0.95, which suggests that the Eg5 stalk$_{364-520}$ domain is neither fully coiled-coil nor entirely made up of non-coiled helices. The estimated percentage of helices is 52 %, while that of the turns and unordered regions is a total of 43 %. These results from the CD analysis suggest that the Eg5 stalk$_{364-520}$ domain may form an interrupted coiled-coil structure.

Lastly, small angle X-ray scattering (SAXS) experiment was carried out to determine the low resolution molecular envelope of the Eg5 stalk$_{364-520}$ domain. The scattering profiles of four samples of protein with different concentrations (ranging from 1 to 20 mg/ml) are similar; thus agreeing with the AUC data that there is no concentration-dependent oligomerisation behaviour. The reproducible shape of the scattering curve hints at a rod-shaped molecule. The mean maximum dimension (D_{max}) is 19.3 nm, while the mean radius of gyration (R_g) and extrapolated intensity at zero scattering angle for the Eg5 stalk$_{364-520}$ domain, obtained from the pair-distance distribution function plot, are 5.5 nm and 44.4 respectively.

Ab initio modelling of the molecular envelope of Eg5 stalk$_{364-520}$ domain from the scattering profiles reveal a reproducible rod-like molecular envelope that is approximately 165 Å long and 18 Å wide. The molecular envelope appears to contain kinks along its length, which could indicate an interrupted coiled-coil structure, as supported by the CD results. In short, the AUC, CD and SAXS results suggest that the Eg5 stalk$_{364-520}$ domain facilitates dimerisation of the protein by forming an elongated coiled-coil structure that may be interrupted by kinks along its length.

6.1.3 Autoinhibition mechanism of kinesin-1

The structure of the kinesin-1 motor domain dimer was solved to provide additional structural information for the modelling of kinesin-1 motility. Unfortunately, the docking of the kinesin-1 dimer structure onto microtubules was unsuccessful, revealing clashes between helix α2 of the unattached motor domain and α-tubulin. This is probably because both motor domains of the dimer structure are in the ADP-bound state. Nevertheless, the crystal structure reveals an alternate global conformation of the dimer, which provides a new conformation for modelling the mechanism of motility. The dimer structure also serves as a comparison for the structure of the kinesin-1 motor domain dimer-tail complex that was solved.

Differences between the free dimer structure and the dimer-tail complex provide insights into the autoinhibition mechanism of kinesin-1. In the absence of the tail domain, the motor domain dimer is likely to have considerable freedom of movement. However, when the monomeric tail domain binds to the dimeric motor domain, the latter becomes highly restricted due to cross-linking at two positions: coiled-coil and tail interface. As a result, major relative movements, such as the undocking of the neck linker, may be prevented. Results from our collaborator have shown that by engineering a covalent cross-link in the dimer at the tail interface, tail-mediated autoinhibition of kinesin-1 can be mimicked.

This covalent mimic was then shown to release ADP very slowly in the presence and absence of microtubules, as compared to the wild-type dimer. The release of ADP has been hypothesised and shown to be linked to undocking of the neck linker. Hence, based on the structural information and biochemical data, we propose a double lockdown autoinhibition mechanism, whereby cross-linking at both the coiled-coil and tail interface prevents the movement of the motor domains that is needed to undock the neck linker and release ADP. This opens up the possibility that other kinesins may be regulated by a common autoinhibitory mechanism.

Finally, the crystal structure of the dimer-tail complex reveals several important residues in the motor-tail interface that may be responsible for the binding of the tail to the motor domains. Alanine-scan peptide array confirms that Lys944 and Arg947 of the tail domain are crucial residues that would abolish motor-tail interaction when mutated. In addition, microtubule-stimulated single turnover assays carried out by our collaborator showed that Asp185 and His136 of the motor domain are important residues involved in the binding of the tail. In short, the crystal structures and biochemical data provide us with a better understanding of the mechanism of autoinhibition of kinesin-1.

6.2 Future directions

6.2.1 Continued development of mitotic kinesin Eg5 inhibitors

Based on the SAR studies and the crystal structures of Eg5-inhibitor complexes, we propose several steps for the future development of Eg5 inhibitors. As we have shown that some inhibitors have preferential binding conformations, we suggest separating the racemic mixtures of potential compounds into their enantiomers to identify the more active biological agent. For *S*-trityl-L-cysteine (STLC) analogues, the addition of a small lipophilic substituent on the *meta*- or *para*- positions of the phenyl ring has been shown to greatly improve potency. Substitution of the sulphur in STLC with a carbon atom did not decrease the potency of the small molecule. Hence, it might be a good idea to adopt the carbon scaffold in future development, as it is more stable and less likely to be hydrolysed or oxidized in the human gut.

To develop STLC analogues that are weak substrates or less susceptible to the P-glycoprotein (Pgp) efflux pump, the carboxylic acid group should be removed from the amine tail. However, the resultant flexibility of the small molecule and the loss of several hydrogen bonds may result in a decrease in potency. In addition, an analogue of compound **7** lacking the carboxylic acid group revealed hERG liability, high microsomal clearance in mice, low bioavailability, and is a moderate substrate for several cytochrome P450 isoforms, as compared to **7** which has the carboxylic acid group (unpublished data). These liabilities would have to be overcome by a different subgroup or more substituents on the phenyl rings to increase stability and potency. Next, by comparing the crystal structures of Eg5 in complex with monastrol, monastrol analogues and compound **9**, we realised that the common 3-hydroxyphenyl group forms important hydrogen bond interactions with the residues in the pocket. Hence, it may be useful to keep this subgroup while modifying the rest of the small molecule.

Taking into account all the observations from the various crystal structures and the SAR studies, we now have a basis for structure-guided optimisation that will hopefully lead to compounds with improved potency. Eg5 inhibitors that prove to be highly potent should then be tested in cell-based assays for their

susceptibility to the Pgp efflux pump. Cox *et al*. consider compounds with multidrug resistance (MDR) ratios of less than 10 as having the potential to overcome MDR[193,194]. Subsequently, absorption, distribution, metabolism and excretion (ADME) profiling and *in vivo* xenograft studies should be conducted on inhibitors that are weak substrates of Pgp, in order to shortlist potential candidates with optimal drug-like properties for clinical trials.

6.2.2 Characterisation of mitotic kinesin Eg5 stalk domain

Characterisation of the Eg5 stalk domain will aid us in understanding its purported functions: formation of a tetramer and coordination of Eg5 motility. However, attempts to express the full length Eg5 stalk domain in the bacterial *Escherichia coli* system have not been successful; therefore, little is known about the structure or biophysical properties of the stalk domain. In order to investigate the role of the stalk domain in the normal functioning of Eg5, we need to first express and purify the protein. To this end, using a different expression system, such as the yeast *Pichia pastoris* system, may result in higher protein expression and yield. In addition, *P. pastoris* is capable of producing certain post-translational modifications, such as glycosylation, which could allow proper folding of the protein.

Once the protein has been expressed and purified to a high yield and purity, crystallisation trials can be carried out. With a high resolution crystal structure of the Eg5 stalk domain, the structural characteristics of the molecule will become apparent and we will be able to confirm if it is a full or interrupted coiled-coil domain. Based on the structure, we can then try to understand how the stalk domain facilitates the formation of a bipolar tetrameric kinesin and coordinates the 'hand-over-hand' motility of Eg5. AUC experiment can also be used to determine whether there is a concentration-dependent oligomerisation behaviour. Nonetheless, if crystallisation is unsuccessful, CD and SAXS could be used to determine the secondary structure elements and the shape of the molecular envelope respectively.

6.2.3 Autoinihibition mechanism of kinesins

The proposed double lockdown mechanism of kinesin-1 autoinhibition opens up possibilities that other kinesins may be regulated by a common mechanism. Although the autoinhibition mechanism has been best studied in kinesin-1, other members, such as the kinesin-2, kinesin-3 and kinesin-7 families, are also regulated by autoinhibition when they are not performing their functions. Similar to kinesin-1, these kinesin members adopt a folded conformation when inactive[195-198]. Hence, it is possible that the folded conformation allows the tail to interact with the motor domains in the same way as the double lockdown mechanism does in kinesin-1. Future work should therefore be focused on dissecting the autoinhibition mechanism of these kinesins and identifying the region of the tail domain that is involved in the regulation of the molecular motor.

Based on the crystal structure of the kinesin-1 motor-tail complex, only one tail is shown to bind to the dimeric motor domains to prevent them from undergoing relative movements to undock the neck linker and release ADP. However, the function and position of the other tail domain of the kinesin dimer remain unclear. We speculate that the second tail domain could interact with microtubules and immobilise the kinesin on the track, while waiting for cargo to arrive. Alternatively, it could interact with kinesin-associated proteins, which could further regulate cargo-binding and transport abilities of kinesin[28]. Further experiments would have to be conducted to confirm or disprove these hypotheses.

The dimer-tail structure, the peptide array and the biochemical data have revealed several residues that are implicated in the autoinhibition of kinesin-1. When these residues are mutated, binding of the tail to the motor domains is abolished and autoinhibition is relieved. In a recent paper by Moua *et al.*, randomly generated lethal mutations in the *Drosophila melanogaster* kinesin heavy chain led to the identification of two mutations in the IAK region of the tail domain that may be crucial for development, namely P945S and S948F[199]. However, the results of the study showed that these mutants do not relieve autoinhibition but inhibit kinesin-1 functions instead. As these mutations are

different from those identified in our studies, we propose revisiting the experiments using mutants of residues identified in our studies to gain insight into the true functions of the tail-mediated autoinhibition mechanism *in vivo*.

Kinesin-1 has been linked to several diseases in humans, such as Alzheimer's disease, neurofibromatosis (cancer of nerve tissues) and vaccinia and herpes viral infections[119-122]. It has been found to bind to amyloid precursor protein, form a complex with neurofibromatosis tumour suppressors and transport the vaccinia and herpes viruses. With insight into how kinesin-1 is autoinhibited, we open new avenues for understanding how kinesin-1 may play a role in the above diseases and for the possible development of therapeutics. In short, the basic knowledge of the autoinhibition mechanism of kinesin-1 may lead to and be translated into clinically-relevant findings for the treatment of diseases.

Bibliography

1. Vale, R.D., Reese, T.S. & Sheetz, M.P. Identification of a novel force-generating protein, kinesin, involved in microtubule-based motility. *Cell* **42**, 39-50 (1985).
2. Brady, S.T. A novel brain ATPase with properties expected for the fast axonal transport motor. *Nature* **317**, 73-5 (1985).
3. Vale, R.D., Schnapp, B.J., Reese, T.S. & Sheetz, M.P. Organelle, bead, and microtubule translocations promoted by soluble factors from the squid giant axon. *Cell* **40**, 559-69 (1985).
4. Allen, R.D. et al. Gliding movement of and bidirectional transport along single native microtubules from squid axoplasm: evidence for an active role of microtubules in cytoplasmic transport. *J Cell Biol* **100**, 1736-52 (1985).
5. Yang, J.T., Laymon, R.A. & Goldstein, L.S. A three-domain structure of kinesin heavy chain revealed by DNA sequence and microtubule binding analyses. *Cell* **56**, 879-89 (1989).
6. Kim, A.J. & Endow, S.A. A kinesin family tree. *J Cell Sci* **113 Pt 21**, 3681-2 (2000).
7. Lawrence, C.J. et al. A standardized kinesin nomenclature. *J Cell Biol* **167**, 19-22 (2004).
8. Woehlke, G. & Schliwa, M. Walking on two heads: the many talents of kinesin. *Nat Rev Mol Cell Biol* **1**, 50-8 (2000).
9. Dagenbach, E.M. & Endow, S.A. A new kinesin tree. *J Cell Sci* **117**, 3-7 (2004).
10. Hunter, A.W. et al. The kinesin-related protein MCAK is a microtubule depolymerase that forms an ATP-hydrolyzing complex at microtubule ends. *Mol Cell* **11**, 445-57 (2003).
11. Alonso, M.C., van Damme, J., Vandekerckhove, J. & Cross, R.A. Proteolytic mapping of kinesin/ncd-microtubule interface: nucleotide-dependent conformational changes in the loops L8 and L12. *EMBO J* **17**, 945-51 (1998).
12. Woehlke, G. et al. Microtubule interaction site of the kinesin motor. *Cell* **90**, 207-16 (1997).

13. Hirose, K., Lowe, J., Alonso, M., Cross, R.A. & Amos, L.A. Congruent docking of dimeric kinesin and ncd into three-dimensional electron cryomicroscopy maps of microtubule-motor ADP complexes. *Mol Biol Cell* **10**, 2063-74 (1999).
14. Kikkawa, M., Okada, Y. & Hirokawa, N. 15 A resolution model of the monomeric kinesin motor, KIF1A. *Cell* **100**, 241-52 (2000).
15. Bourne, H.R., Sanders, D.A. & McCormick, F. The GTPase superfamily: conserved structure and molecular mechanism. *Nature* **349**, 117-27 (1991).
16. Sablin, E.P., Kull, F.J., Cooke, R., Vale, R.D. & Fletterick, R.J. Crystal structure of the motor domain of the kinesin-related motor ncd. *Nature* **380**, 555-9 (1996).
17. Kull, F.J., Sablin, E.P., Lau, R., Fletterick, R.J. & Vale, R.D. Crystal structure of the kinesin motor domain reveals a structural similarity to myosin. *Nature* **380**, 550-5 (1996).
18. Rice, S. et al. A structural change in the kinesin motor protein that drives motility. *Nature* **402**, 778-84 (1999).
19. Sindelar, C.V. et al. Two conformations in the human kinesin power stroke defined by X-ray crystallography and EPR spectroscopy. *Nat Struct Biol* **9**, 844-8 (2002).
20. Tao, L. et al. A homotetrameric kinesin-5, KLP61F, bundles microtubules and antagonizes Ncd in motility assays. *Curr Biol* **16**, 2293-302 (2006).
21. Cole, D.G. et al. Novel heterotrimeric kinesin-related protein purified from sea urchin eggs. *Nature* **366**, 268-70 (1993).
22. Lupas, A., Van Dyke, M. & Stock, J. Predicting coiled coils from protein sequences. *Science* **252**, 1162-4 (1991).
23. Stock, M.F. et al. Formation of the compact confomer of kinesin requires a COOH-terminal heavy chain domain and inhibits microtubule-stimulated ATPase activity. *J Biol Chem* **274**, 14617-23 (1999).
24. Hackney, D.D. & Stock, M.F. Kinesin's IAK tail domain inhibits initial microtubule-stimulated ADP release. *Nat Cell Biol* **2**, 257-60 (2000).
25. Karabay, A. & Walker, R.A. Identification of microtubule binding sites in the Ncd tail domain. *Biochemistry* **38**, 1838-49 (1999).
26. Wendt, T. et al. A structural analysis of the interaction between ncd tail and tubulin protofilaments. *J Mol Biol* **333**, 541-52 (2003).

27. Braun, M., Drummond, D.R., Cross, R.A. & McAinsh, A.D. The kinesin-14 Klp2 organizes microtubules into parallel bundles by an ATP-dependent sorting mechanism. *Nat Cell Biol* **11**, 724-30 (2009).
28. Gindhart, J.G. et al. The kinesin-associated protein UNC-76 is required for axonal transport in the Drosophila nervous system. *Mol Biol Cell* **14**, 3356-65 (2003).
29. Howard, J., Hudspeth, A.J. & Vale, R.D. Movement of microtubules by single kinesin molecules. *Nature* **342**, 154-8 (1989).
30. Block, S.M., Goldstein, L.S. & Schnapp, B.J. Bead movement by single kinesin molecules studied with optical tweezers. *Nature* **348**, 348-52 (1990).
31. Hackney, D.D. Highly processive microtubule-stimulated ATP hydrolysis by dimeric kinesin head domains. *Nature* **377**, 448-50 (1995).
32. Svoboda, K., Schmidt, C.F., Schnapp, B.J. & Block, S.M. Direct observation of kinesin stepping by optical trapping interferometry. *Nature* **365**, 721-7 (1993).
33. Lockhart, A., Crevel, I.M. & Cross, R.A. Kinesin and ncd bind through a single head to microtubules and compete for a shared MT binding site. *J Mol Biol* **249**, 763-71 (1995).
34. Schnitzer, M.J. & Block, S.M. Kinesin hydrolyses one ATP per 8-nm step. *Nature* **388**, 386-90 (1997).
35. Svoboda, K. & Block, S.M. Force and velocity measured for single kinesin molecules. *Cell* **77**, 773-84 (1994).
36. Howard, J. *Mechanics of motor proteins and the cytoskeleton.*, (Sinauer Associates, Inc., Sunderland, MA, 2001).
37. Higuchi, H., Bronner, C.E., Park, H.W. & Endow, S.A. Rapid double 8-nm steps by a kinesin mutant. *EMBO J* **23**, 2993-9 (2004).
38. Kaseda, K., Higuchi, H. & Hirose, K. Alternate fast and slow stepping of a heterodimeric kinesin molecule. *Nat Cell Biol* **5**, 1079-82 (2003).
39. Yildiz, A., Tomishige, M., Vale, R.D. & Selvin, P.R. Kinesin walks hand-over-hand. *Science* **303**, 676-8 (2004).
40. Nonaka, S. et al. Randomization of left-right asymmetry due to loss of nodal cilia generating leftward flow of extraembryonic fluid in mice lacking KIF3B motor protein. *Cell* **95**, 829-37 (1998).

41. Wong, R.W., Setou, M., Teng, J., Takei, Y. & Hirokawa, N. Overexpression of motor protein KIF17 enhances spatial and working memory in transgenic mice. *Proc Natl Acad Sci U S A* **99**, 14500-5 (2002).
42. Teng, J. et al. The KIF3 motor transports N-cadherin and organizes the developing neuroepithelium. *Nat Cell Biol* **7**, 474-82 (2005).
43. Pilling, A.D., Horiuchi, D., Lively, C.M. & Saxton, W.M. Kinesin-1 and Dynein are the primary motors for fast transport of mitochondria in Drosophila motor axons. *Mol Biol Cell* **17**, 2057-68 (2006).
44. Kanai, Y., Dohmae, N. & Hirokawa, N. Kinesin transports RNA: isolation and characterization of an RNA-transporting granule. *Neuron* **43**, 513-25 (2004).
45. Hirokawa, N. Organelle transport along microtubules - the role of KIFs. *Trends Cell Biol* **6**, 135-41 (1996).
46. Ou, G., Blacque, O.E., Snow, J.J., Leroux, M.R. & Scholey, J.M. Functional coordination of intraflagellar transport motors. *Nature* **436**, 583-7 (2005).
47. Reid, E. et al. A kinesin heavy chain (KIF5A) mutation in hereditary spastic paraplegia (SPG10). *Am J Hum Genet* **71**, 1189-94 (2002).
48. Zhu, C. et al. Functional analysis of human microtubule-based motor proteins, the kinesins and dyneins, in mitosis/cytokinesis using RNA interference. *Mol Biol Cell* **16**, 3187-99 (2005).
49. Kapitein, L.C. et al. The bipolar mitotic kinesin Eg5 moves on both microtubules that it crosslinks. *Nature* **435**, 114-8 (2005).
50. Lombillo, V.A., Nislow, C., Yen, T.J., Gelfand, V.I. & McIntosh, J.R. Antibodies to the kinesin motor domain and CENP-E inhibit microtubule depolymerization-dependent motion of chromosomes in vitro. *J Cell Biol* **128**, 107-15 (1995).
51. Wordeman, L. & Mitchison, T.J. Identification and partial characterization of mitotic centromere-associated kinesin, a kinesin-related protein that associates with centromeres during mitosis. *J Cell Biol* **128**, 95-104 (1995).
52. Hirokawa, N., Noda, Y., Tanaka, Y. & Niwa, S. Kinesin superfamily motor proteins and intracellular transport. *Nat Rev Mol Cell Biol* **10**, 682-96 (2009).

53. Jackson, J.R., Patrick, D.R., Dar, M.M. & Huang, P.S. Targeted anti-mitotic therapies: can we improve on tubulin agents? *Nat Rev Cancer* **7**, 107-17 (2007).

54. Morris, N.R. Mitotic mutants of *Aspergillis nidulans*. *Genetics Research* **26**, 237-254 (1975).

55. Le Guellec, R., Paris, J., Couturier, A., Roghi, C. & Philippe, M. Cloning by differential screening of a Xenopus cDNA that encodes a kinesin-related protein. *Mol Cell Biol* **11**, 3395-8 (1991).

56. Blangy, A. et al. Phosphorylation by p34cdc2 regulates spindle association of human Eg5, a kinesin-related motor essential for bipolar spindle formation in vivo. *Cell* **83**, 1159-69 (1995).

57. Kashina, A.S. et al. A bipolar kinesin. *Nature* **379**, 270-2 (1996).

58. Turner, J. et al. Crystal structure of the mitotic spindle kinesin Eg5 reveals a novel conformation of the neck-linker. *J Biol Chem* **276**, 25496-502 (2001).

59. Parke, C.L., Wojcik, E.J., Kim, S. & Worthylake, D.K. ATP hydrolysis in Eg5 kinesin involves a catalytic two-water mechanism. *J Biol Chem* **285**, 5859-67 (2010).

60. Rosenfeld, S.S., Xing, J., Jefferson, G.M. & King, P.H. Docking and rolling, a model of how the mitotic motor Eg5 works. *J Biol Chem* **280**, 35684-95 (2005).

61. Zhao, Y.C., Kull, F.J. & Cochran, J.C. Modulation of the kinesin ATPase cycle by neck linker docking and microtubule binding. *J Biol Chem* **285**, 25213-20 (2010).

62. Larson, A.G., Naber, N., Cooke, R., Pate, E. & Rice, S.E. The conserved L5 loop establishes the pre-powerstroke conformation of the Kinesin-5 motor, eg5. *Biophys J* **98**, 2619-27 (2010).

63. Behnke-Parks, W.M. et al. Loop L5 acts as a conformational latch in the mitotic kinesin Eg5. *J Biol Chem* **286**, 5242-53 (2011).

64. Cochran, J.C. & Gilbert, S.P. ATPase mechanism of Eg5 in the absence of microtubules: insight into microtubule activation and allosteric inhibition by monastrol. *Biochemistry* **44**, 16633-48 (2005).

65. Blangy, A., Arnaud, L. & Nigg, E.A. Phosphorylation by p34cdc2 protein kinase regulates binding of the kinesin-related motor HsEg5 to the dynactin subunit p150. *J Biol Chem* **272**, 19418-24 (1997).

66. Weinger, J.S., Qiu, M., Yang, G. & Kapoor, T.M. A nonmotor microtubule binding site in kinesin-5 is required for filament crosslinking and sliding. *Curr Biol* **21**, 154-60 (2011).
67. Crevel, I.M., Lockhart, A. & Cross, R.A. Kinetic evidence for low chemical processivity in ncd and Eg5. *J Mol Biol* **273**, 160-70 (1997).
68. Stout, J.R., Rizk, R.S., Kline, S.L. & Walczak, C.E. Deciphering protein function during mitosis in PtK cells using RNAi. *BMC Cell Biol* **7**, 26 (2006).
69. Mountain, V. et al. The kinesin-related protein, HSET, opposes the activity of Eg5 and cross-links microtubules in the mammalian mitotic spindle. *J Cell Biol* **147**, 351-66 (1999).
70. Sharp, D.J. et al. Functional coordination of three mitotic motors in Drosophila embryos. *Mol Biol Cell* **11**, 241-53 (2000).
71. Tanenbaum, M.E. et al. Kif15 cooperates with eg5 to promote bipolar spindle assembly. *Curr Biol* **19**, 1703-11 (2009).
72. Ferhat, L. et al. Expression of the mitotic motor protein Eg5 in postmitotic neurons: implications for neuronal development. *J Neurosci* **18**, 7822-35 (1998).
73. Sarli, V. & Giannis, A. Targeting the kinesin spindle protein: basic principles and clinical implications. *Clin Cancer Res* **14**, 7583-7 (2008).
74. Bartoli, K.M., Jakovljevic, J., Woolford, J.L., Jr. & Saunders, W.S. Kinesin Molecular Motor Eg5 Functions during Polypeptide Synthesis. *Mol Biol Cell* (2011).
75. Wilson, L. & Jordan, M.A. New microtubule/tubulin-targeted anticancer drugs and novel chemotherapeutic strategies. *J Chemother* **16 Suppl 4**, 83-5 (2004).
76. Rowinsky, E.K., Chaudhry, V., Cornblath, D.R. & Donehower, R.C. Neurotoxicity of Taxol. *J Natl Cancer Inst Monogr*, 107-15 (1993).
77. Jordan, M.A. & Wilson, L. Microtubules as a target for anticancer drugs. *Nat Rev Cancer* **4**, 253-65 (2004).
78. Orr, G.A., Verdier-Pinard, P., McDaid, H. & Horwitz, S.B. Mechanisms of Taxol resistance related to microtubules. *Oncogene* **22**, 7280-95 (2003).
79. Kavallaris, M. Microtubules and resistance to tubulin-binding agents. *Nat Rev Cancer* **10**, 194-204 (2010).
80. Mayer, T.U. et al. Small molecule inhibitor of mitotic spindle bipolarity identified in a phenotype-based screen. *Science* **286**, 971-4 (1999).

81. DeBonis, S. et al. Interaction of the mitotic inhibitor monastrol with human kinesin Eg5. *Biochemistry* **42**, 338-49 (2003).
82. Gartner, M. et al. Development and biological evaluation of potent and specific inhibitors of mitotic Kinesin Eg5. *Chembiochem* **6**, 1173-7 (2005).
83. DeBonis, S. et al. In vitro screening for inhibitors of the human mitotic kinesin Eg5 with antimitotic and antitumor activities. *Mol Cancer Ther* **3**, 1079-90 (2004).
84. Skoufias, D.A. et al. S-trityl-L-cysteine is a reversible, tight binding inhibitor of the human kinesin Eg5 that specifically blocks mitotic progression. *J Biol Chem* **281**, 17559-69 (2006).
85. Kozielski, F. et al. Proteome analysis of apoptosis signaling by S-trityl-L-cysteine, a potent reversible inhibitor of human mitotic kinesin Eg5. *Proteomics* **8**, 289-300 (2008).
86. Leizerman, I., Avunie-Masala, R., Elkabets, M., Fich, A. & Gheber, L. Differential effects of monastrol in two human cell lines. *Cell Mol Life Sci* **61**, 2060-70 (2004).
87. Jiang, C. et al. Design, synthesis and evaluation of tetrahydroisoquinolines as new kinesin spindle protein inhibitors. *Chem Pharm Bull (Tokyo)* **57**, 567-71 (2009).
88. Kim, K.S. et al. Synthesis and SAR of pyrrolotriazine-4-one based Eg5 inhibitors. *Bioorg Med Chem Lett* **16**, 3937-42 (2006).
89. Sheth, P.R. et al. Novel benzimidazole inhibitors bind to a unique site in the kinesin spindle protein motor domain. *Biochemistry* **49**, 8350-8 (2010).
90. Brier, S., Lemaire, D., DeBonis, S., Forest, E. & Kozielski, F. Molecular dissection of the inhibitor binding pocket of mitotic kinesin Eg5 reveals mutants that confer resistance to antimitotic agents. *J Mol Biol* **360**, 360-76 (2006).
91. Yan, Y. et al. Inhibition of a mitotic motor protein: where, how, and conformational consequences. *J Mol Biol* **335**, 547-54 (2004).
92. Maliga, Z. et al. A pathway of structural changes produced by monastrol binding to Eg5. *J Biol Chem* **281**, 7977-82 (2006).
93. Carol, H. et al. Initial testing (stage 1) of the kinesin spindle protein inhibitor ispinesib by the pediatric preclinical testing program. *Pediatr Blood Cancer* **53**, 1255-63 (2009).

94. Matsuda, M., Yamamoto, T., Matsumura, A. & Kaneda, Y. Highly efficient eradication of intracranial glioblastoma using Eg5 siRNA combined with HVJ envelope. *Gene Ther* **16**, 1465-76 (2009).

95. Liu, M. et al. Validating the mitotic kinesin Eg5 as a therapeutic target in pancreatic cancer cells and tumor xenografts using a specific inhibitor. *Biochem Pharmacol* **76**, 169-78 (2008).

96. Wiltshire, C. et al. Docetaxel-resistant prostate cancer cells remain sensitive to S-trityl-L-cysteine-mediated Eg5 inhibition. *Mol Cancer Ther* **9**, 1730-9 (2010).

97. Marcus, A.I. et al. Mitotic kinesin inhibitors induce mitotic arrest and cell death in Taxol-resistant and -sensitive cancer cells. *J Biol Chem* **280**, 11569-77 (2005).

98. Liu, M. et al. Ectopic expression of the microtubule-dependent motor protein Eg5 promotes pancreatic tumourigenesis. *J Pathol* **221**, 221-8 (2010).

99. Carter, B.Z. et al. Regulation and targeting of Eg5, a mitotic motor protein in blast crisis CML: overcoming imatinib resistance. *Cell Cycle* **5**, 2223-9 (2006).

100. Castillo, A., Morse, H.C., 3rd, Godfrey, V.L., Naeem, R. & Justice, M.J. Overexpression of Eg5 causes genomic instability and tumor formation in mice. *Cancer Res* **67**, 10138-47 (2007).

101. Hanahan, D. & Weinberg, R.A. Hallmarks of cancer: the next generation. *Cell* **144**, 646-74 (2011).

102. Johnson, R.K., McCabe, F.L., Cauder, E., et al. SB-715992, a potent and selective inhibitor of KSP mitotic kinesin, demonstrates broad-spectrum activity in advanced murine tumors and human humor xenografts. *Proc Am Assoc Cancer Res* **43**, 269 (2002).

103. Chu, Q.S., Holen, K.D., Rowinsky, E.K., et al. Phase I trial of novel kinesin spindle protein (KSP) inhibitor SB-715992 IC Q 21 days. *Proc Am Soc Clin Oncol* **22**, A2078 (2004).

104. Heath, E.I., Alouisi, A., Eder, J.P., et al. A phase I dose escalation trial of ispinesib (SB-715992) administered days 1-3 of a 21-day cycle in patients with advanced solid tumors. . *Proc Am Soc Clin Oncol* **24**, A2026 (2006).

105. Burris, H.A., Lorusso, P., Jones, S., et al. Phase I trial of novel kinesin spindle protein (KSP) inhibitor SB-715992 IV days 1, 8, 15 q 28 days. *J Clin Oncol* **22**, 2004 (2004).

106. Miller, K., Ng, C., Ang, P., et al. . PTC phase II, open label study of SB-715992 (Ispinesib) in subjects with advanced or metastatic breast cancer. *Breast Cancer Res Treat* **94 (suppl 1)**, abstract 1089 (2004).

107. Hirokawa, N. et al. Submolecular domains of bovine brain kinesin identified by electron microscopy and monoclonal antibody decoration. *Cell* **56**, 867-78 (1989).

108. Henningsen, U. & Schliwa, M. Reversal in the direction of movement of a molecular motor. *Nature* **389**, 93-6 (1997).

109. Case, R.B., Pierce, D.W., Hom-Booher, N., Hart, C.L. & Vale, R.D. The directional preference of kinesin motors is specified by an element outside of the motor catalytic domain. *Cell* **90**, 959-66 (1997).

110. Endow, S.A. & Waligora, K.W. Determinants of kinesin motor polarity. *Science* **281**, 1200-2 (1998).

111. Hackney, D.D., Levitt, J.D. & Suhan, J. Kinesin undergoes a 9 S to 6 S conformational transition. *J Biol Chem* **267**, 8696-701 (1992).

112. Hirokawa, N. & Takemura, R. Molecular motors and mechanisms of directional transport in neurons. *Nat Rev Neurosci* **6**, 201-14 (2005).

113. Sack, S. et al. X-ray structure of motor and neck domains from rat brain kinesin. *Biochemistry* **36**, 16155-65 (1997).

114. Song, Y.H. et al. Structure of a fast kinesin: implications for ATPase mechanism and interactions with microtubules. *EMBO J* **20**, 6213-25 (2001).

115. Kozielski, F. et al. The crystal structure of dimeric kinesin and implications for microtubule-dependent motility. *Cell* **91**, 985-94 (1997).

116. Verhey, K.J. & Hammond, J.W. Traffic control: regulation of kinesin motors. *Nat Rev Mol Cell Biol* **10**, 765-77 (2009).

117. Saxton, W.M., Hicks, J., Goldstein, L.S. & Raff, E.C. Kinesin heavy chain is essential for viability and neuromuscular functions in Drosophila, but mutants show no defects in mitosis. *Cell* **64**, 1093-102 (1991).

118. Gho, M., McDonald, K., Ganetzky, B. & Saxton, W.M. Effects of kinesin mutations on neuronal functions. *Science* **258**, 313-6 (1992).

119. Kamal, A., Almenar-Queralt, A., LeBlanc, J.F., Roberts, E.A. & Goldstein, L.S. Kinesin-mediated axonal transport of a membrane compartment containing beta-secretase and presenilin-1 requires APP. *Nature* **414**, 643-8 (2001).

120. Hakimi, M.A., Speicher, D.W. & Shiekhattar, R. The motor protein kinesin-1 links neurofibromin and merlin in a common cellular pathway of neurofibromatosis. *J Biol Chem* **277**, 36909-12 (2002).

121. Rietdorf, J. et al. Kinesin-dependent movement on microtubules precedes actin-based motility of vaccinia virus. *Nat Cell Biol* **3**, 992-1000 (2001).

122. Diefenbach, R.J. et al. Herpes simplex virus tegument protein US11 interacts with conventional kinesin heavy chain. *J Virol* **76**, 3282-91 (2002).

123. Hua, W., Chung, J. & Gelles, J. Distinguishing inchworm and hand-over-hand processive kinesin movement by neck rotation measurements. *Science* **295**, 844-8 (2002).

124. Asbury, C.L., Fehr, A.N. & Block, S.M. Kinesin moves by an asymmetric hand-over-hand mechanism. *Science* **302**, 2130-4 (2003).

125. Arnal, I. & Wade, R.H. Nucleotide-dependent conformations of the kinesin dimer interacting with microtubules. *Structure* **6**, 33-8 (1998).

126. Hirose, K., Lockhart, A., Cross, R.A. & Amos, L.A. Three-dimensional cryoelectron microscopy of dimeric kinesin and ncd motor domains on microtubules. *Proc Natl Acad Sci U S A* **93**, 9539-44 (1996).

127. Hirose, K., Lowe, J., Alonso, M., Cross, R.A. & Amos, L.A. 3D electron microscopy of the interaction of kinesin with tubulin. *Cell Struct Funct* **24**, 277-84 (1999).

128. Hirose, K., Lockhart, A., Cross, R.A. & Amos, L.A. Nucleotide-dependent angular change in kinesin motor domain bound to tubulin. *Nature* **376**, 277-9 (1995).

129. Hoenger, A. et al. A new look at the microtubule binding patterns of dimeric kinesins. *J Mol Biol* **297**, 1087-103 (2000).

130. Yildiz, A. & Selvin, P.R. Kinesin: walking, crawling or sliding along? *Trends Cell Biol* **15**, 112-20 (2005).

131. Friedman, D.S. & Vale, R.D. Single-molecule analysis of kinesin motility reveals regulation by the cargo-binding tail domain. *Nat Cell Biol* **1**, 293-7 (1999).

132. Coy, D.L., Hancock, W.O., Wagenbach, M. & Howard, J. Kinesin's tail domain is an inhibitory regulator of the motor domain. *Nat Cell Biol* **1**, 288-92 (1999).
133. Hackney, D.D. & Stock, M.F. Kinesin tail domains and Mg2+ directly inhibit release of ADP from head domains in the absence of microtubules. *Biochemistry* **47**, 7770-8 (2008).
134. Seiler, S. et al. Cargo binding and regulatory sites in the tail of fungal conventional kinesin. *Nat Cell Biol* **2**, 333-8 (2000).
135. Wong, Y.L. & Rice, S.E. Kinesin's light chains inhibit the head- and microtubule-binding activity of its tail. *Proc Natl Acad Sci U S A* **107**, 11781-6 (2010).
136. Hackney, D.D., Baek, N. & Snyder, A.C. Half-site inhibition of dimeric kinesin head domains by monomeric tail domains. *Biochemistry* **48**, 3448-56 (2009).
137. Dietrich, K.A. et al. The kinesin-1 motor protein is regulated by a direct interaction of its head and tail. *Proc Natl Acad Sci U S A* **105**, 8938-43 (2008).
138. Garcia-Saez, I. et al. Structure of human Eg5 in complex with a new monastrol-based inhibitor bound in the R configuration. *J Biol Chem* **282**, 9740-7 (2007).
139. Otwinowski, Z. & Minor, W. [20] Processing of X-ray diffraction data collected in oscillation mode. in *Methods in Enzymology*, Vol. Volume 276 307 (Academic Press, 1997).
140. Powell, H.R. The Rossmann Fourier autoindexing algorithm in MOSFLM. *Acta Crystallogr D Biol Crystallogr* **55 (Pt 10)**, 1690-5 (1999).
141. Evans, P.R. Scaling and assessment of data quality. *Acta Cryst* **D62**, 72-82 (2005).
142. Collaborative Computational Project, N. The CCP4 Suite: Programs for Protein Crystallography. *Acta Cryst*, 760-763 (1994).
143. Padilla, J.E. & Yeates, T.O. A statistic for local intensity differences: robustness to anisotropy and pseudo-centering and utility for detecting twinning. *Acta Crystallogr D Biol Crystallogr* **59**, 1124-30 (2003).
144. Yeates, T.O. Detecting and overcoming crystal twinning. *Methods Enzymol* **276**, 344-58 (1997).

145. Vagin, A., Teplyakov, A. MOLREP: an automated program for molecular replacement. *J. Appl. Cryst.* **30**, 1022-1025 (1997).
146. Yan, Y. et al. Inhibition of a Mitotic Motor Protein: Where, How, and Conformational Consequences. *Journal of Molecular Biology* **335**, 547-554 (2004).
147. Murshudov, G.N., Vagin, A.A. & Dodson, E.J. Refinement of macromolecular structures by the maximum-likelihood method. *Acta Crystallogr D Biol Crystallogr* **53**, 240-55 (1997).
148. Emsley, P. & Cowtan, K. Coot: model-building tools for molecular graphics. *Acta Crystallogr D Biol Crystallogr* **60**, 2126-32 (2004).
149. Schuttelkopf, A.W. & van Aalten, D.M. PRODRG: a tool for high-throughput crystallography of protein-ligand complexes. *Acta Crystallogr D Biol Crystallogr* **60**, 1355-63 (2004).
150. Laskowski, R.A., MacArthur, M.W., Moss, D.S. & Thornton, J.M. PROCHECK: a program to check the stereochemical quality of protein structures. *J App Cryst* **283**, 283-291 (1993).
151. Schrodinger, LLC. The PyMOL Molecular Graphics System, Version 1.3r1. (2010).
152. Adams, P.D. et al. PHENIX: a comprehensive Python-based system for macromolecular structure solution. *Acta Crystallographica Section D-Biological Crystallography* **66**, 213-221 (2010).
153. Burmeister, W.P. Structural changes in a cryo-cooled protein crystal owing to radiation damage. *Acta Crystallogr D Biol Crystallogr* **56**, 328-41 (2000).
154. Leiros, H.K., McSweeney, S.M. & Smalas, A.O. Atomic resolution structures of trypsin provide insight into structural radiation damage. *Acta Crystallogr D Biol Crystallogr* **57**, 488-97 (2001).
155. McCoy, A.J. et al. Phaser crystallographic software. *J Appl Crystallogr* **40**, 658-674 (2007).
156. Kim, E.D. et al. Allosteric drug discrimination is coupled to mechanochemical changes in the kinesin-5 motor core. *J Biol Chem* **285**, 18650-61 (2010).
157. Chen, V.B. et al. MolProbity: all-atom structure validation for macromolecular crystallography. *Acta Crystallographica Section D-Biological Crystallography* **66**, 12-21 (2010).

158. Leue, T.M., Shah, B.D., Ridgeway, T.M., Pelletier, S.L. Computer-aided interpretation of analytical sedimentation data for proteins. in *Analytical ultracentrifugation in biochemistry and polymer science*. (Royal Society for Chemistry, Cambridge, UK, 1992).
159. Schuck, P. Size-distribution analysis of macromolecules by sedimentation velocity ultracentrifugation and lamm equation modeling. *Biophys J* **78**, 1606-19 (2000).
160. Vistica, J. et al. Sedimentation equilibrium analysis of protein interactions with global implicit mass conservation constraints and systematic noise decomposition. *Anal Biochem* **326**, 234-56 (2004).
161. Whitmore, L. & Wallace, B.A. DICHROWEB, an online server for protein secondary structure analyses from circular dichroism spectroscopic data. *Nucleic Acids Res* **32**, W668-73 (2004).
162. Provencher, S.W. & Glockner, J. Estimation of globular protein secondary structure from circular dichroism. *Biochemistry* **20**, 33-7 (1981).
163. Konarev, P.V., Volkov, V.V., Sokolova, A.V., Koch, M.H.J., Svergun, D.I. PRIMUS: a Windows PC-based system for small-angle scattering data analysis. . *J. Appl. Crystallogr.* **36**, 1277-1282 (2003).
164. Guinier, A., Fournet, G. *Small angle X-ray scattering*, (Wiley, New York, 1955).
165. Semenyuk, A.V., Svergun, D.I. GNOM -- a program package for small angle scattering data processing. *J. Appl. Cryst.* **24**, 537-540 (1991).
166. Svergun, D.I., Petoukhov, M.V. & Koch, M.H. Determination of domain structure of proteins from X-ray solution scattering. *Biophys J* **80**, 2946-53 (2001).
167. Volkov, V.V., Svergun, D.I. Uniqueness of ab initio shape determination in small-angle scattering. *J. Appl. Cryst.* **36**, 860-864 (2003).
168. Jiang, W., Stock, M.F., Li, X. & Hackney, D.D. Influence of the kinesin neck domain on dimerization and ATPase kinetics. *J Biol Chem* **272**, 7626-32 (1997).
169. Krissinel, E. & Henrick, K. Inference of macromolecular assemblies from crystalline state. *Journal of Molecular Biology* **372**, 774-797 (2007).
170. Muller, K., Faeh, C. & Diederich, F. Fluorine in pharmaceuticals: looking beyond intuition. *Science* **317**, 1881-6 (2007).

171. Chakrabarti, P. & Bhattacharyya, R. Geometry of nonbonded interactions involving planar groups in proteins. *Prog Biophys Mol Biol* **95**, 83-137 (2007).

172. Sheth, P.R. et al. Thermodynamics of nucleotide and inhibitor binding to wild-type and ispinesib-resistant forms of human kinesin spindle protein. *Biochemistry* **48**, 11045-55 (2009).

173. Kaan, H.Y. et al. Structural basis for inhibition of Eg5 by dihydropyrimidines: stereoselectivity of antimitotic inhibitors enastron, dimethylenastron and fluorastrol. *J Med Chem* **53**, 5676-83 (2010).

174. Prokopcova, H. et al. Structure-activity relationships and molecular docking of novel dihydropyrimidine-based mitotic Eg5 inhibitors. *ChemMedChem* **5**, 1760-9 (2010).

175. Kaan, H.Y. et al. Structure-activity relationship and multidrug resistance study of new S-trityl-L-cysteine derivatives as inhibitors of Eg5. *J Med Chem* **54**, 1576-86 (2011).

176. Boonyapiwat, B., Panaretou, B., Forbes, B., Mitchell, S.C. & Steventon, G.B. Human phenylalanine monooxygenase and thioether metabolism. *J Pharm Pharmacol* **61**, 63-7 (2009).

177. Kerns, E.H. & Di, L. *Drug-like properties: concepts, structure design and methods. From ADME to toxicity optimization*, (Elsevier, 2008).

178. Glatter, O., Kratky, O. *Small angle X-ray scattering*, (Academic Press, London, UK, 1982).

179. Zhou, N.E., Kay, C.M. & Hodges, R.S. The net energetic contribution of interhelical electrostatic attractions to coiled-coil stability. *Protein Eng* **7**, 1365-72 (1994).

180. Diefenbach, R.J., Mackay, J.P., Armati, P.J. & Cunningham, A.L. The C-terminal region of the stalk domain of ubiquitous human kinesin heavy chain contains the binding site for kinesin light chain. *Biochemistry* **37**, 16663-70 (1998).

181. Yousef, M.S., Kamikubo, H., Kataoka, M., Kato, R. & Wakatsuki, S. Miranda cargo-binding domain forms an elongated coiled-coil homodimer in solution: implications for asymmetric cell division in Drosophila. *Protein Sci* **17**, 908-17 (2008).

182. Bodey, A.J., Kikkawa, M. & Moores, C.A. 9-Angstrom structure of a microtubule-bound mitotic motor. *J Mol Biol* **388**, 218-24 (2009).

183. Kikkawa, M. & Hirokawa, N. High-resolution cryo-EM maps show the nucleotide binding pocket of KIF1A in open and closed conformations. *EMBO J* **25**, 4187-94 (2006).
184. Sindelar, C.V. & Downing, K.H. The beginning of kinesin's force-generating cycle visualized at 9-A resolution. *J Cell Biol* **177**, 377-85 (2007).
185. Hirokawa, N., Nitta, R. & Okada, Y. The mechanisms of kinesin motor motility: lessons from the monomeric motor KIF1A. *Nat Rev Mol Cell Biol* **10**, 877-84 (2009).
186. Hackney, D.D. Evidence for alternating head catalysis by kinesin during microtubule-stimulated ATP hydrolysis. *Proc Natl Acad Sci U S A* **91**, 6865-9 (1994).
187. Crevel, I.M., Lockhart, A. & Cross, R.A. Weak and strong states of kinesin and ncd. *J Mol Biol* **257**, 66-76 (1996).
188. Cheng, J.Q., Jiang, W. & Hackney, D.D. Interaction of mant-adenosine nucleotides and magnesium with kinesin. *Biochemistry* **37**, 5288-95 (1998).
189. Kull, F.J. & Endow, S.A. Kinesin: switch I & II and the motor mechanism. *J Cell Sci* **115**, 15-23 (2002).
190. Hwang, W., Lang, M.J. & Karplus, M. Force generation in kinesin hinges on cover-neck bundle formation. *Structure* **16**, 62-71 (2008).
191. Sindelar, C.V. & Downing, K.H. An atomic-level mechanism for activation of the kinesin molecular motors. *Proc Natl Acad Sci U S A* **107**, 4111-6 (2010).
192. Hahlen, K. et al. Feedback of the kinesin-1 neck-linker position on the catalytic site. *J Biol Chem* **281**, 18868-77 (2006).
193. Cox, C.D. et al. Kinesin spindle protein (KSP) inhibitors. Part V: discovery of 2-propylamino-2,4-diaryl-2,5-dihydropyrroles as potent, water-soluble KSP inhibitors, and modulation of their basicity by beta-fluorination to overcome cellular efflux by P-glycoprotein. *Bioorg Med Chem Lett* **17**, 2697-702 (2007).
194. Cox, C.D. et al. Kinesin spindle protein (KSP) inhibitors. 9. Discovery of (2S)-4-(2,5-difluorophenyl)-n-[(3R,4S)-3-fluoro-1-methylpiperidin-4-yl]-2-(hydroxymethyl)-N-methyl-2-phenyl-2,5-dihydro-1H-pyrrole-1-carboxamide (MK-0731) for the treatment of taxane-refractory cancer. *J Med Chem* **51**, 4239-52 (2008).

195. Espeut, J. et al. Phosphorylation relieves autoinhibition of the kinetochore motor Cenp-E. *Mol Cell* **29**, 637-43 (2008).

196. Hammond, J.W. et al. Mammalian Kinesin-3 motors are dimeric in vivo and move by processive motility upon release of autoinhibition. *PLoS Biol* **7**, e72 (2009).

197. Imanishi, M., Endres, N.F., Gennerich, A. & Vale, R.D. Autoinhibition regulates the motility of the C. elegans intraflagellar transport motor OSM-3. *J Cell Biol* **174**, 931-7 (2006).

198. Okada, Y., Yamazaki, H., Sekine-Aizawa, Y. & Hirokawa, N. The neuron-specific kinesin superfamily protein KIF1A is a unique monomeric motor for anterograde axonal transport of synaptic vesicle precursors. *Cell* **81**, 769-80 (1995).

199. Moua, P., Fullerton, D., Serbus, L.R., Warrior, R. & Saxton, W.M. Kinesin-1 tail autoregulation and microtubule-binding regions function in saltatory transport but not ooplasmic streaming. *Development* **138**, 1087-92 (2011).

Appendices

Appendix 1

Kaan, H.Y., Ulaganathan, V., Hackney, D.D. & Kozielski, F. An allosteric transition trapped in an intermediate state of a new kinesin-inhibitor complex. *Biochem J* **425**, 55-60 (2010).

Appendix 2

Kaan, H.Y., Ulaganathan, V., Rath, O., Prokopcová, H., Dallinger, D., Kappe, C.O. & Kozielski, F. Structural basis for inhibition of Eg5 by dihydropyrimidines: stereoselectivity of antimitotic inhibitors enastron, dimethylenastron and fluorastrol. *J Med Chem* **53**, 5676-83 (2010).

Appendix 3

Kaan, H.Y., Weiss, J., Menger, D., Ulaganathan, V., Tkocz, K., Laggner, C., Popowycz, F., Joseph, B. & Kozielski, F. 2010. Structure-activity relationship and multidrug resistance study of new *S*-trityl-L-cysteine derivatives as inhibitors of Eg5. *J Med Chem* **54**, 1576-86 (2011).

Appendix 5: List of co-author published paper and submitted manuscript.

Published co-author paper:

Prokopcová, H., Dallinger, D., Uray, G., Kaan, H.Y., Ulaganathan, V., Kozielski, F., Laggner, C. & Kappe, C.O. Structure-activity relationships and molecular docking of novel dihydropyrimidine-based mitotic Eg5 inhibitors. *ChemMedChem* **5**, 1760-9 (2010).

Submitted manuscript:

Wang, F., Good, J.A.D., Rath, O., Kaan, H.Y., Sutcliffe, O.B., Mackay. S.P., Kozielski, F. 2011. Triphenylbutanamines — kinesin spindle protein inhibitors with *in vivo* anti-tumour activity. *J Med Chem*. (Submitted)